Politecnico di Torino

FACOLTÀ DI INGEGNERIA
Corso di Laurea Magistrale in Ingegneria Meccanica

Tesi di laurea magistrale

Development of a Health-and-Usage-Monitoring-System for Ball Screws in Electro-Mechanical Actuators

Candidato:
Lorenzo Trecroci
Matricola 238871

Relatore:
Prof. Massimo Sorli

Correlatori:
Prof. Giovanni Jacazio
Prof. Frank Thielecke

Anno Accademico 2017-2018

"Non si puó mai attraversare l'oceano
se non si ha il coraggio di perdere di vista la riva"
[*Cristoforo Colombo*]

Abstract

The More Electric Aircraft is one of the main drivers in current aircraft systems' research and development. Indeed, higher electrification of aircrafts can reduce complexity as well as the weight of power supply systems. In this respect, one of the principal aims of More Electric Aircraft (MEA) is to replace the hydraulic supply with electric technologies in the primary flight control surfaces.

In order to do that, it is possible to employ an Electro-Mechanical Actuator (EMA) which mainly consists of a Brushless DC motor, a reducer and a ball screw. However, although this replacing seems feasible in theory, there are several issues that have to be overcome. One of these is represented by the wear mechanisms that affect the ball screw due to disadvantageous motion profiles of primary flight controls. In the light of this assessment, the principal goal of this thesis is the development of a suitable Health-and-Usage-Monitoring-System for ball screws embedded in EMAs.

In attempt to do that, firstly an extensive literature research was carried out, in order to understand the state-of-the-art of primary and secondary flight controls, ball screw's structure, wear mechanisms as well as principal HUMS's concepts.

After that, a high fidelity ball screw model was developed in Matlab/Simulink environement, in order to simulate the degradation in ball screws. In this respect several simulations was carried out to highlight the model's behavior when subjected to different parameters such as external force, preload and degradation effects.

In the last part of the thesis a second model capable to simulate the EMA's nominal condition was derived from the high fidelity model. By comparing the parameters of the monitoring model with the high fidelity model, a health assessment of the actuator can be carried out. In particular, in this thesis two methodologies are proposed: one uses the frequency spectrum of the motor current and another utilizes the variations of several indexes capable to detect the deviations of e.g. motor current and nut position due to wear mechanisms. Finally, by using the motor current index, a methodology to identify the actuator's Remaining Useful Life (RUL) is proposed .

On the basis of the obtained results, it is possible to conclude that the proposed methodologies should be capable to detect degradation in ball screws. Indeed, the deviations caused by degradations are high enough to detect decreasing in EMA's performances. For this reason, the results obtained in this thesis represent promising concepts for further analyses and experimental validation.

Contents

List of Figures

List of Tables

Introduction

The Electro-Mechanical Actuators (EMA) are embedded in several fields of engineering such as robotic or aircraft. In particular, in the last years the studies concernig EMAs are increased in order to obtain the concept of More Electric Aircraft (MEA). This last is one of the most stimulating challanges in aircraft fields because the use of electric technologies instead of hydraulic ones can lead to several advantages as reduced weight and less complexity. However, the EMAs are struggled to be employed in primary flight controls due to degradation and wear mechanisms that affect the mechanical components. In order to overcome these issues, the newest researches are trying to identify a suitable Health and Usage Monitoring System in order to predict faults in EMAs. One of the possible methodologies by which faults in EMAs can be envisaged consists in developing a detailed numerical model by which the behavior of the actuator can be simulated.
In particular, the principal goal of this thesis is to develop a HUMS for ball screws embedded in EMA for primary flight controls by following the afore mentioned model-approach. This work tries to identify new methodologies by which a health assessment of the EMA and prediction of its Remaining Useful Life (RUL) can be carried out.
This thesis is divided in three macro sections. The first part carries out an extensive literature research in order to have an overview of the ball screw's issues, expecially correlated to wear mechanisms and degradation. After that, a high fidelity EMA's model is developed in order to simulate degradation effects. In particular, this thesis focuses on the development of a detailed ball screw model based on previous works [1, 2]. Finally, in the last part of the work two methodologies based on the frequency analysis and definition of condition indexes are explained.
The thesis is composed by six chapters: the first one provides an overview of the EMA's problems correlated with wear mechanisms and degradation that lead to decreased performances. The second chapter explains the ball screw's structure as well as the refence systems utilized in the ball screw model. In the last part of this chapter a case study is reported in order to understand how the wear mechanisms affect the ball screw's parameters. The third chapter explains the characteristics of wear mechanisms in detail. In particular, these lasts are not embedded in the ball screw model because the analysis was carried out in a parametric way. However, the studies conducted in this chapter can

represent a basis for further analyses. The fourth chapter treats the principal HUMS's concepts, with a focus on its structure and principal methodologies commonly used nowadays. The fifth chapter treats in detail the developed model with the utilized equations and hypotheses whereas the last chapter explains the HUMS' proposed methodologies to detect degradation in ball screws.
Thanks to this work it was possible to identify useful methodologies by which a health assessment and prediction of EMA's RUL can be obtained. In particular, the deviations observed from the nominal conditions are enough high to carry out a HUMS in ball screws. The results of this work will be explained in detail in the finals conclusions of this thesis.

Chapter 1

EMA for More Electric Aircraft

In this first chapter the most important perspectives about More Electric Aircraft are explained. The first section deals with the so-called primary and secondary flight control surfaces, in order to understand the main users that need of energy. The second section shows an overview of the hydraulic supplies and compares them with the electrical technologies. After that, the third section explains the concept of the More Electric Aircraft (MEA), in order to understand the principal advantages of electric supplies rather than hydraulic technologies. To obtain electric supply in aircraft systems, it is possible to follow three difeerent concepts: the Electro-Hydrostatic Actuator (EHA), the Integrated Actuation Package (IAP) and the Electro-Mechanical Actuator (EMA). Among the afore mentioned solutions, the EMA likely represents the most promising concept in terms of saving costs and weight of the aircraft [2]. In the light of this assessment, the fourth section talks about the EMA's principal components: Brushless DC Motor, gear box and ball screw. However, the electromechanical actuator is struggled to be employed in the primary flight control applications due to the mechanical jamming susceptibility caused by wear mechanisms. Furthermore, the degradation also affects strongly the performances of EMA's components by leading to lower accuracy and reliability.
For these reasons, nowadays the idea is to include prognostic and diagnostic systems that can predict faults and failures in EMA, by maintaining its standard mechanical structure. This thesis analyzes the development of a HUMS for a ball screw. In order to do that, in the second chapter the ball screw's structure will be explained, so as to identify the parameters that can be useful to forecast possible failures in ball screw.

1.1 Flight Controls in commercial aircrafts

The commercial aircrafts are composed by several surfaces by which is possible to achieve the aircraft's rotation along its three axes or an increasing of its performances.

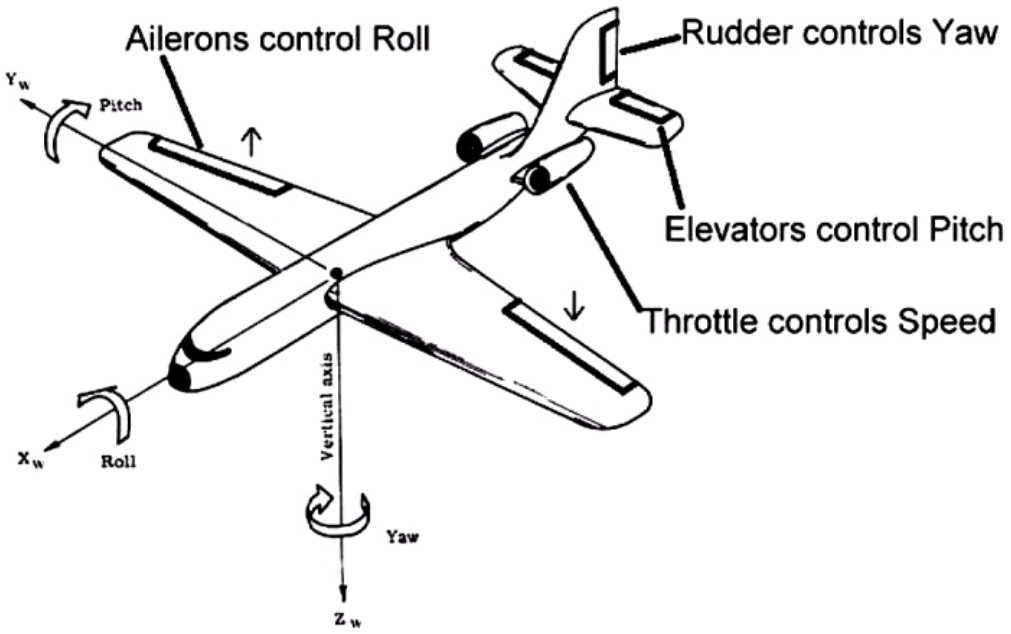

Figure 1.1: Aircraft axes [2]

The Figure 1.1 depicts the afore mentioned aircraft's axes. In particular, it is possible to observe three axes: the longitudinal (roll), lateral (pitch) and vertical axis (yaw). In order to obtain the rotation along these axes, in the aircrafts the so-called primary flight controls are embedded. These last consist in ailerons, elevators and rudder, which control the aircraft's rotation along the roll, pitch and yaw axes respectively.
However, as depicted in Figure 1.2, there are other surfaces employed in the aircrafts. For instance, it is possible to observe in the figure the flaps, slats and spoilers. These last are the so-called secondary flight controls. In particular, their aim is to increase as much as possible the performances of the aircraft by optimizing the aerodynamics on the basis of the flight conditions [2].
For instace, the flaps increase as much as possible the lift during the take-off. It is known that the lift raises according to the incidence angle until a critical value. After that, the lift decreases highly due to the boundary limits effects. These types of surfaces manage to delay this effect in order to improve the aircraft's performances [2].
The slats are placed in the opposite part of the wing. They modify the wing profile, by creating an orifice that energize the boundary layer. In this way, the slats manage to reduce the stall speed [2].
The spoilers reduce the lift as well as causing an increasing of the hydrodynamic resis-

tance. They allow to unload the wings, by increasing the adherence between the ground and tires. They are also used in-flight for helping the ailerons. Usually, near the flaps the airbrakers are employed (they are not shown in Figure 1.2). Their principal goal is similar to the spoilers, because they cause a speed reduction by increasing the hydrodynamic resistance. In particular, this consequence can be useful during the cruise or landing phase [2].

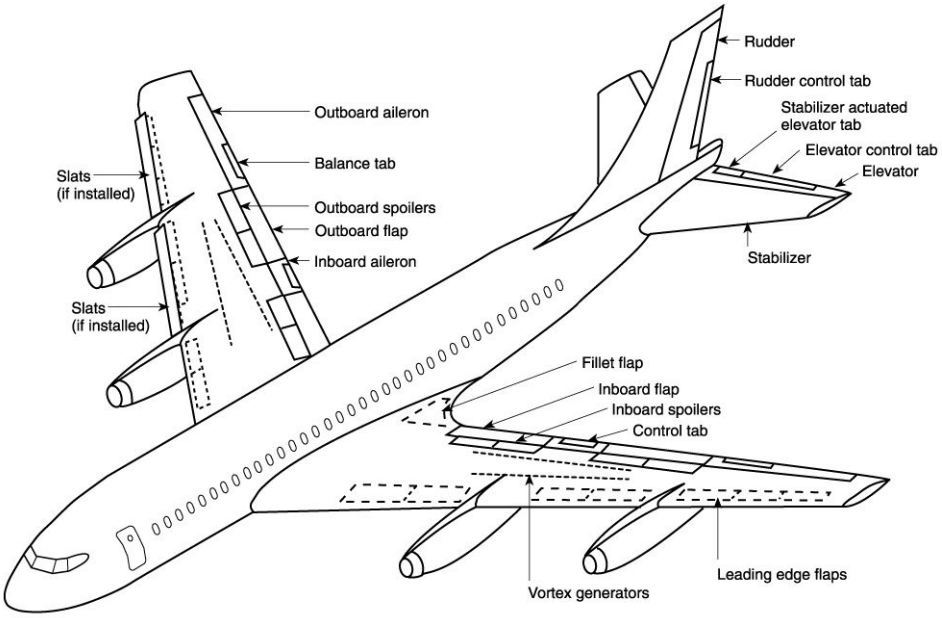

Figure 1.2: Primary and secondary flight controls [3]

In order to obtain the motion of these surfaces, it is necessary to employ flight control systems by which the surfaces' orientation can be controlled. Depending on the applications, the flight control systems can be obtained with different techniques. For instance, they can be realized with mechanical connections such as cables and shafts. Obviously, these solutions are feasible only in the small aircrafts, where the strenght requested to move the surfaces is not too high.

For this reason, in the large aircrafts hydraulic or electric supplies are employed to increase the amplitude's command before it reaches the surfaces. A consequence of the hydraulic or electric energy in flight controls is the possibility of usying active control for the reduction of load flights, the self-driving as well as improvement of aircraft reliability [2]. Nowadays, the most commonly used are the hydraulic supplies, thanks to their reliability and high power density at equipment level. For this reason, in the next section the hydraulic systems are analyzed.

1.2 State-Of-The-Art

As before mentioned, nowadays the primary flight control surfaces are mostly supplied by hydraulic technologies. These lasts consist on a hydraulic valve that commands a cylinder-piston system, as depicted in the Figure 1.3.

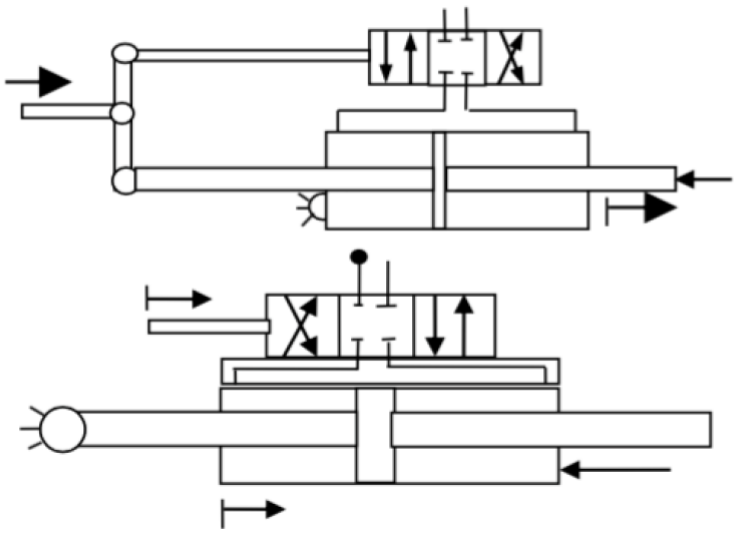

Figure 1.3: Hydraulic actuator with a parallel and series command [2]

The command received from the crew causes a displacement of the spool. Therefore, the valve changes the differential pressures in the cylinder chambers: in this way it is possible to move the piston and then the surface. This type of actuation system is the most used thanks to its high power-weight density. However, the weight of the overall hydraulic power systems is not low due to the pressure fluid network and pumps.
The hydraulic power systems are embedded in aircrafts since over 50 years. Previously, these last were utilized only in the so-called secondary flight control. Successively, their use has increased in many closed-loop functions as primary flight control and landing gear steering. The principal reasons of this conceptual change are different [4]:

- With the developing of aircraft technologies the human strength is no longer sufficient to satisfy the power requests of users. This aspect promotes the development of hydraulic power systems thanks to their high power density at equipment level
- In order to reduce the pilot's intellectual and physical burden and improve the aircraft's performances

For the afore-mentioned reasons, the hydraulic power systems are employed for supplying the primary and secondary flight control surfaces. However, despite of the HPS's advantages, nowadays the drawbacks of hydraulic supplies are less and less accepted [4]. In fact,

in the course of the years the constraints that the aircrafts have to respect are becoming increasingly difficult to respect for hydraulic technologies. Indeed, the pollutants fluids embedded in these systems are ever less accepted due to restrictive environmental laws. Moreover, other types of issues are making this technology obsolete for primary flight controls [4]:

- The power distribution of pressurized fluids represents a constraint difficult to overcome in the large aircraft where the pumps can be placed so far from the actuators (until $50\,m$)
- The hydraulics networks have small potential reconfigurations
- The power regulation and control are realized by throttling valves. For this reason, when the aircraft does not operate under nominal conditions, its efficiency decreases

In order to partially overcome the principal drawbacks of hydraulic power systems, it is possible to adopt several solutions. For instance, by placing the hydraulic power as close as possible to the actuation need or utilizing displacement control of the power instead of valve throttling as well as replacing the standard valves with Direct Drive Valves (DDVs) [4].
However, these solutions can overcome the hydraulic power systems' drawbacks only partially. For this reason, the present trend is to replace in the primary and secondary flight control applications the hydraulic power systems with other types of technologies, as explained in the following section.

1.3 More Electric Aircraft (MEA)

In attempt to overcome the hydraulic system's drawbacks, the idea is to eliminate in the before mentioned applications the hydraulic supplies with electrical ones. In this respect, the principal goal of More Electric Aircraft (MEA) is to replace the hydraulic supply with electric components. The MEA represents in the coming years one of the most stimulating challenges in aircraft field. Thanks to the introduction of electrical parts, a reduction of costs (mostly due to the increased price of fuel), environmental impact (by reducing the pollutant fluids), control complexity and saving of aircraft weight, in addition to eliminating leakages can be obtained. Moreover, electrical systems have high gains in safety, reconfiguration and maintenance, as well as permitting an easier maintainability of mechanical parts. The candidate concepts to reach a MEA are principally three [5]:

- Electro-Mechanical Actuator (EMA), which allows to obtain a rotary motion through a gear box or a linear motion thanks to a gear box and ball screw

- Electro Hydrostatic Actuator (EHA), where a fixed displacement pump is driven by a variable speed motor

- Integrated Actuator Package (IAP), where a variable displacement pump is driven by a fixed speed motor, as depicted in Figure 1.4. This solution was abandoned due to the low efficiency, hydraulic stiffness and heat issues

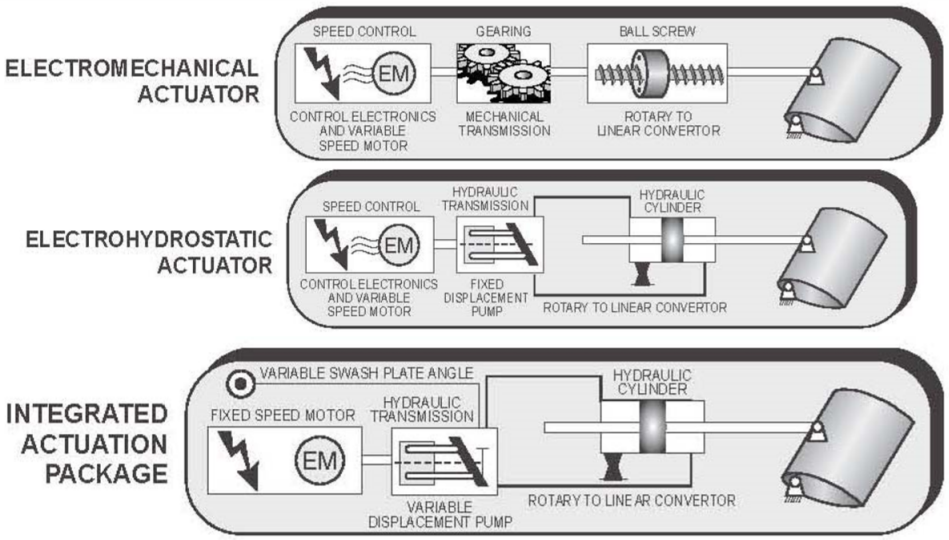

Figure 1.4: The different actuation system architecture [5]

The electro-hydrostatic actuator makes the control actions by using an electrical drive instead of a hydraulic one. Moreover, the EHA manages to provide an electric supply with proven availability, because hydraulic components are immune to jamming problems. On the contrary, the EMAs permit to obtain more benefits in terms of saving weight and costs but they struggle to be applied in primary flight control due to jamming problems caused by wear mechanisms. The mechanical jamming can be avoided by embedding an anti-jamming system in the EMA; for instance, the CESA developed a "jam-tolerant" EMA system [6]. However, the wear mechanisms cause also reduction in performances and actuator's accuracy. For this reason, it is important to analyze the principal components affected by these mechanisms in order to show the most suitable solutions in development nowadays.

1.4 Electromechanical actuator

The electromechanical actuator represents one of the most promising concepts in order to benefit from several advantages as fuel and weight saving as well as reducing costs and complexity. In fact, this solution removes totally the hydraulic components to the

advantage of electrical technologies. The electromechanical actuator is composed by three components: Brushless DC motor (BLDC), gear box and screw-nut coupling. The BLDC transfers the electrical power to rotary mechanical motion. The gear box (or reducer) is placed between the motor and screw-nut and provides a defined transmission ratio whereas the screw-nut actuator transforms the rotatory motion of the motor in a linear motion of the nut.

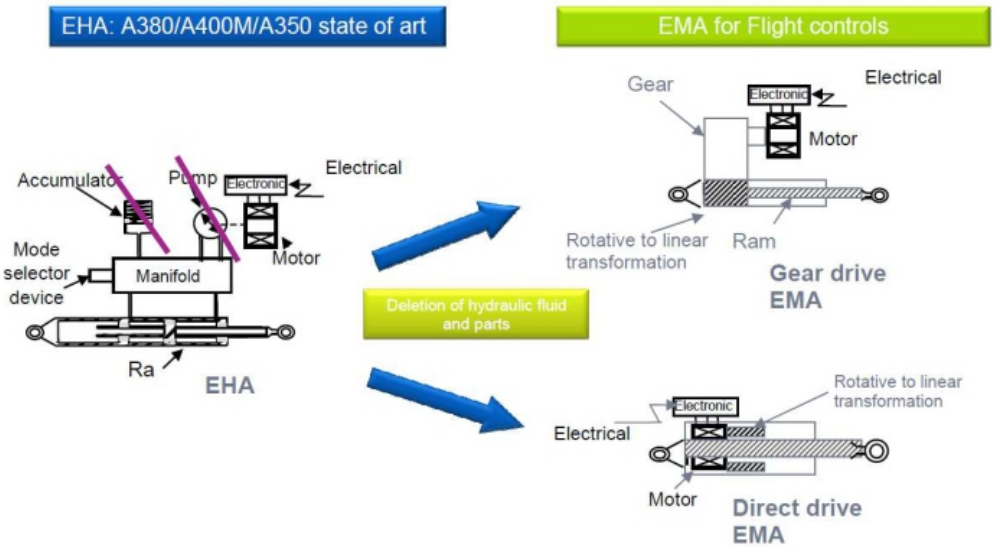

Figure 1.5: Future perspectives of flight controls [7]

As mentioned in the previous paragraph, nowadays the EHAs are in competition with EMAs due to their jamming problems and degradation effects. These last are likely the worst issue because they lead to decreased accuracy and performances. Other issues are represented by the thermal behavior, the duration of some critical mechanical parts as well as the power electronics optimization [6]. However, in few applications some EMA's components have been employed. For instance, they have been implemented in the secondary flight control such as spoilers of the Boeing 787 [7]. Furthermore, the EMAs have been employed on the management of the landing gear swerve during ground phases as well as closure or opening landing gear compartment [2]. However, the trend nowadays is to identify a feasible way to move from the EHA to EMA also in the primary flight controls, as depicted in Figure 1.5.

As afore mentioned, the degradation effects have to be monitored in order to avoid mechanical jamming as well as replacing EMA's components before their performances and accuracy are unacceptable. In the light of this evaluation, a strategy based on failure anticipation represents the most promising concept to solve this issue. In order to do

that, it is possible to embed a Health and Usage Monitoring System (HUMS) by which predicting the Remaining Useful Life (RUL) of the actuator and forecasting the development of degradation effects. Obviously, one of the EMA's components affected by wear mechanisms is the ball screw. For this reason, in the next chapter the ball screw's structure is analyzed, in order to give a technical overview and principal consequences that the wear mechanisms cause in this type of actuator.

Chapter 2

Ball Screw

In this chapter the principal characteristics of ball screw are explained. In the first section the ball screw structure, features and principal advantages of this type of mechanical system are analyzed. The second section shows the reference systems utilized for the ball screw's kinematical analysis. The latters allow to comprehend the equation reported in the fifth chapter in the developed model. Finally, the last section deals with a case study of a preloaded ball screw affected by wear mechanisms, in order to understand how these last affect the ball screw's performances.

2.1 Ball Screw structure

The ball screws are transmission systems which transform the rotary motion of the screw shaft into a linear motion of the nut or vice versa. There are four principal parts of the ball screw:

- The screw, which has an accurate profile of the surface, with several threads and a specific lead
- The nut, that has a linear motion and a threaded interne surface
- Between the screw and the nut there are several balls that allow to obtain high accuracy and efficiency
- To reduce the dimension of the whole system, the balls have to be recirculated. Then, the ball screws include a recirculation path which can be internal or external, in order to permit the continuous flux of the spheres

As the Figure 2.1(a) and 2.1(b) show , this mechanical system can be compared to ball bearing with the difference that the balls have both a linear motion (along the screw axial direction) and a rotary motion. Therefore, the core of the ball screw's kinematic is

represented by the balls, which have a linear, rotational and slip velocity. For this reason, the kinematical analysis of the ball screw is very difficult, because the whole system is closed in its internal part.

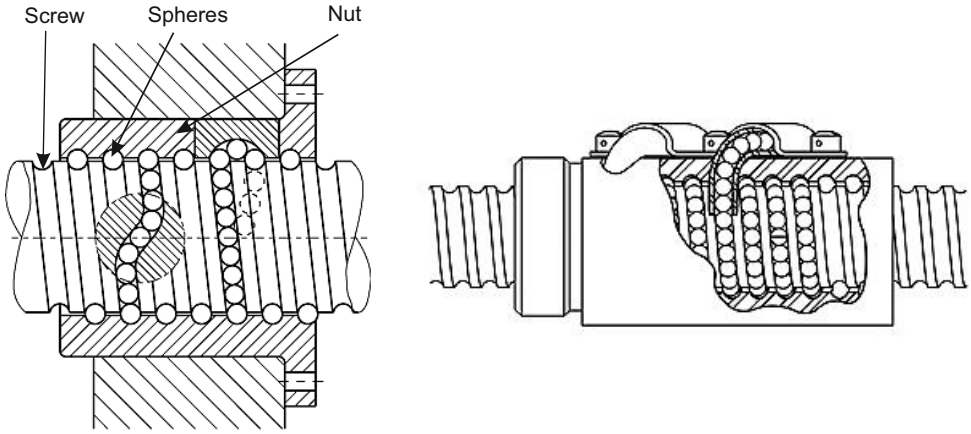

(a) (b)

Figure 2.1: Ball screw with internal (a) and external (b) recirculation of balls [2]

The principal reason why the ball screws are more used than the sliding screws is that the latters have less efficiency than the first one. As a proof of this consideration, the efficiency trend of both ball and sliding screw are depicted in the Figure 2.2(a) and 2.2(b). The Figure 2.2(a) shows the direct efficiency of ball screw which is higher than sliding screw due to the balls, by which the sliding friction is replaced by rolling one. Furthermore, the Figure 2.2(b) depicts the reverse efficiency, which is usually lower than the direct one. Therefore, thanks to the spheres embedded in the system, the ball screws manage to have several advantages [2]:

- Better positioning accuracy
- Higher efficiency
- Lower wear of mechanical parts
- Higher speeds
- Lower driving power requested
- Lower backslash
- The noises are lower than the traditional sliding screw

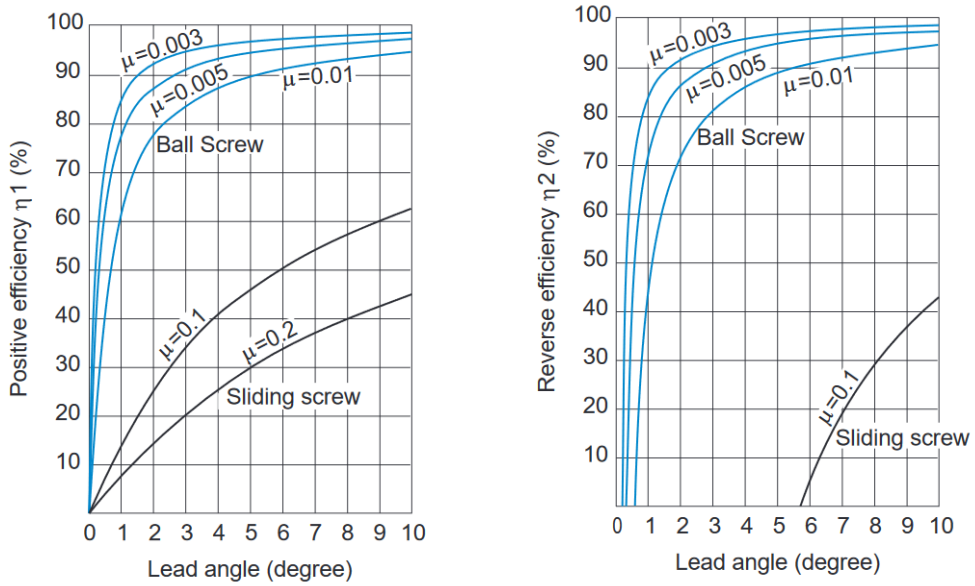

(a) (b)

Figure 2.2: Ball and lead screw efficiency [8]

To evaluate the ball screw's life, the catalogues report two different coefficients. The first one is the static load C_{a0} whereas the second one is dynamic load C_a that the ball screw can sustain. The static load is used to dimension the ball screw for either low speed of the shaft or intermittent motion and it depends on the maximum deformation of the balls (it is the maximum axial load that generates a static deformation equal to 1/10000 of the balls' radius: it represents the highest deformation after which the ball screw's efficiency is affected [2]). On the contrary, the dynamic load is used for high rotational speeds to evaluate ball screw's remaining useful life; in fact, C_a is the axial load (which has to be constant and perfectly centered) that permits to reach or overcome 10^6 cycles with a 90% of reliability [2].

The peak load is also an important parameter, which depends on the distance between the screw supports, the ball screw diameter and the way that it is constrained. In fact, the instability phenomena due to compression loads have to be avoided because they could lead to lower accuracy and seizing of the contact surfaces. Moreover, in the catalogues the maximum rotational speed is also reported. This last is defined as the highest velocity after which instability phenomena would be generated, by creating an irregular motion and bending loads [2].

There are several ball screw types because the nut's and screw's profiles can be different. Indeed, as the Figures 2.3(a) and 2.3(b) depict, the profiles can be semicircular and gothic. The first one is easier to manufacture but the last one is the most used because it decreases the contact pressures by optimizing the axial load's lift.

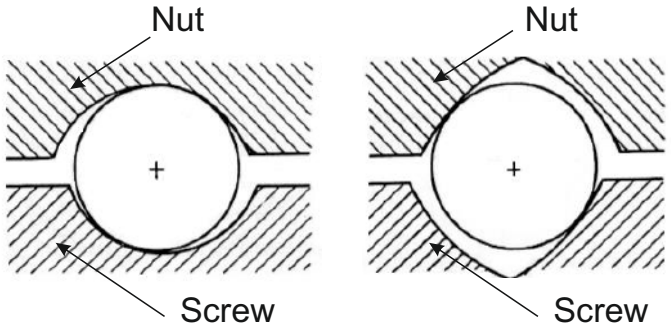

(a) (b)

Figure 2.3: Semicircular (a) and gothic (b) profile [2]

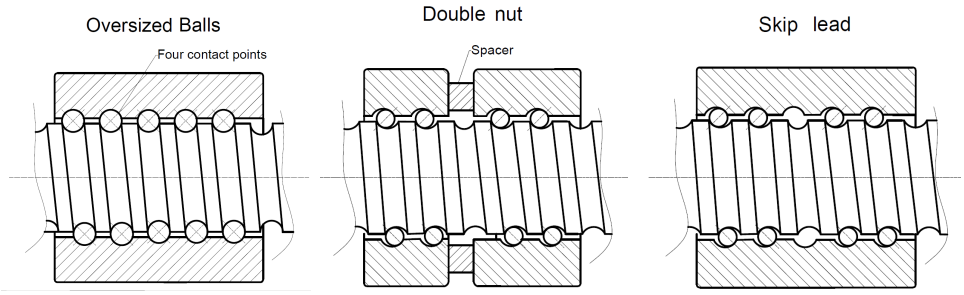

(a) (b) (c)

Figure 2.4: Different mothods to apply a preload in a ball screw

The preload is also a fundamental parameter, because it reduces the axial play as well as decreasing the axial deformations due to the external load. However, an excessive preload leads to higher friction and therefore lower efficiency; for this reason, the preload value should be calculated accurately. As the Figures 2.4(a), 2.4(b) and 2.4(c) depict, the ways to obtain a preload in ball screw are different:

- By using oversized balls, in order to have four contact points instead of only two. This solution leads to increased differential slipping and a spin motion of the spheres along the four axes passing through the contact points. This generates faster wears and heat generation due to the higher friction forces. This phenomenon leads to higher motor torque to balance the increased friction loads

- By using a double nut with a thickness between the two nuts. This method does not generate differential slipping, by avoiding too high wear effects and heat generation

- By manufacturing a pitch offset. This constructive solution does not have to adopt when the external load is high, because the pressures in the contact points can lead to failures due to fatigue

However, to reduce the wear and heat generations, the ball screws contain lubricants such as oil and greases, which have to be chosen based on the operating conditions. Moreover, to avoid the sliding friction due to the contact between the spheres, cages should be adopted; these last allow also to have a lubricant film between the spheres, by obtaining an additional friction reduction.

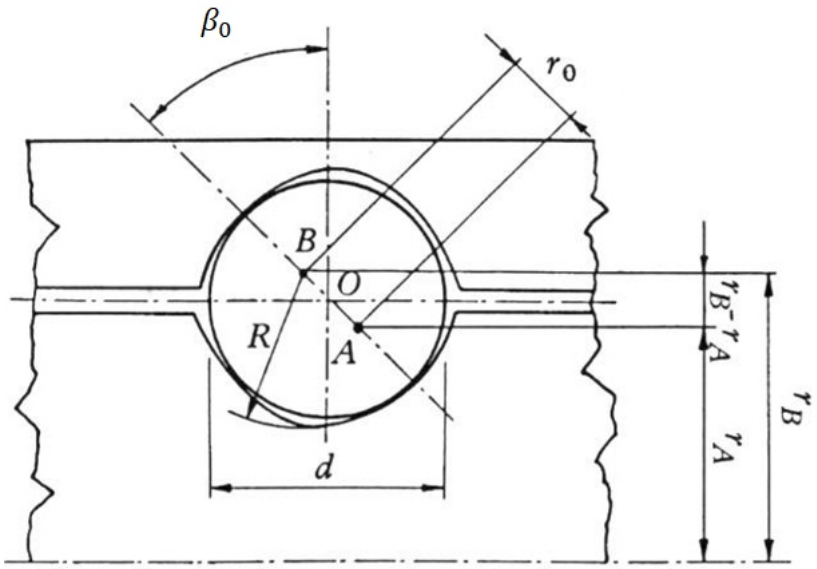

Figure 2.5: Contact angle evaluation [2]

An important ball screw value is the contact angle, which is defined as the angle formed between the pressure line (which passes through one of the two contact points and the ball's center) and the radius plane (passing through the screw axis). Obviously, the contact angles vary if an external load or a preload are applied to the ball screw. The nominal contact angle can be evaluated on the basis of the ball screw's geometry as represented in Figure 2.5 [2]. By identifying as A and B the curvature centers of both profiles, the nominal contact angle is defined as the angle when no external load is applied to the ball screw:

$$\cos(\beta_0) = \frac{r_B - r_A}{r_0} \tag{2.1}$$

$$r_0 = 2 \cdot R - d \tag{2.2}$$

Where R is the curvature radius of the screw's or nut's profiles and d is the ball radius. However, if an external load is applied, the contact angles vary as depicted in the Figure 2.6. Indeed, the external load leads to a deformation called δ that causes a variation of the contact angle β. As the Figure 2.6 depicts, there is a correlation between the deformation

due to the external load and the distance between C_1 and A ($\overline{C_1A}$):

$$\overline{C_1A} = \overline{C_1B} \cdot \tan(\beta) = \delta + r_0 \cdot \sin(\beta_0) \tag{2.3}$$

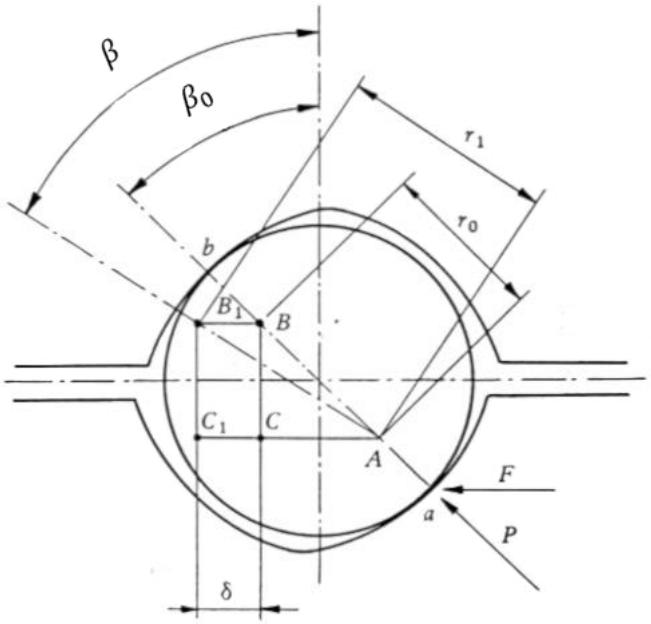

Figure 2.6: Contact angle when an external load is applied on the ball screw [2]

In order to obtain a correlation between the nominal and the current contact angle, it is necessary to approximate the distance between C_1 and B_1 equal to $\overline{CB} = r_0 \cdot \cos(\beta_0)$. Thanks to this hypothesis, the correlation between the two contact points is computed as reported in equation 2.4.

$$\tan(\beta) = \tan(\beta_0) + \frac{\delta}{r_0 \cdot \cos(\beta_0)} \tag{2.4}$$

In many applications the contact angle is equal to 45° and varies due to the external load of $5° - 8°$. However, due to wear mechanisms, the ball screw's geometry can vary, leading to a variation of the contact angles. On the basis of this analysis [2], in the Simulink model it is possible to neglect the variations of contact angle, which is considered equal to 45°.

Once evaluated the contact angle both in nominal and work conditions, the both the direct and reverse ball screw's efficiency can be evaluated as reported in equations 2.5 and 2.6.

$$\eta_d = \frac{\tan(\alpha)}{\tan(\alpha + \phi)} \tag{2.5}$$

$$\eta_r = \frac{\tan(\alpha - \phi)}{\tan(\alpha)} \tag{2.6}$$

Where ϕ is the friction angle. This last can be evaluated as:

$$\tan(\phi) = \frac{f_G}{r_b \cdot \sin(\alpha)} \tag{2.7}$$

Where f_G is the friction coefficient, r_b represents the ball radius whereas α is the helix angle. Obviously, the equations 2.5 and 2.6 approximate the ball screw behavior with the classic screw-nut coupling. However, these formulas are valid only if the preload force is null. If it is necessary to evaluate the ball screw's efficiency by taking into account the rolling and sliding friction (this last is due to slipping phenomena), it is possible to evaluate the ball screw's efficiency according to [9]. In this study a numerical method on the basis of [10] is proposed, in order to evaluate accurately the ball screw efficiency. In particular, the following expressions of direct and reverse efficiency were obtained:

$$\eta_d = \frac{\sin\beta - f \cdot [\cos\gamma_A \cdot \cos\beta + \sin\gamma_A \cdot \tan\alpha'] - \tan\rho \cdot \tan\alpha'}{\tan\alpha' \cdot \left\{\sin\beta + f\left[\cos\gamma_B \cdot \cos\beta - \frac{\sin\gamma_B}{\tan\alpha'}\right]\right\} + \tan\rho} \cdot \tan\alpha' \tag{2.8}$$

$$\eta_r = \frac{\tan\alpha' \cdot \left\{\sin\beta - f \cdot \left[cos\gamma_B \cdot \cos\beta - \frac{sin\gamma_B}{\tan\alpha'}\right]\right\} - \tan\rho}{\left\{\sin\beta + f \cdot [\cos\gamma_A \cdot \cos\beta + \sin\gamma_A \cdot \tan\alpha'] - \tan\rho \cdot \tan\alpha'\right\} \cdot \tan\alpha'} \tag{2.9}$$

Where f is the sliding friction coefficient due to slipping phenomena, γ_i is the sliding friction angle, ρ is the rolling friction angle. This last can be obtained on the basis of rolling friction coefficient f_v:

$$\tan(\rho) = f_v \tag{2.10}$$

Finally, the $\tan\alpha'$ is defined as:

$$\tan\alpha' = \frac{p}{2\pi \cdot (r_m - r_b \cdot \cos\beta)} \tag{2.11}$$

Where r_m is the screw shaft radius and p is the screw pitch. The Figure 2.7 represents the trend of the direct efficiency by varying the nominal helix angle and supposing a contact angle of 45°, a slipping angle $\gamma_A = -\gamma_B = 5°$, a sliding friction coefficient $f = 0.1$, a ball radius $r_b = 3.175\,mm$, a screw radius of $r_m = 8\,mm$ and a rolling friction coefficient of $f_v = 0.005$. As it is shown in the Figure 2.7, by utilizing the equation 2.8 the efficiency trend is similar to the theoretical trend reported in equation 2.5.
It is possible to observe that in the figure the symplified real efficiency trend by neglecting the effect of the contact angle in the $\tan\alpha'$ is also reported. In this condition it is possible to conclude that:

$$\tan\alpha' = \frac{p}{2\pi \cdot r_M} = \tan\alpha \tag{2.12}$$

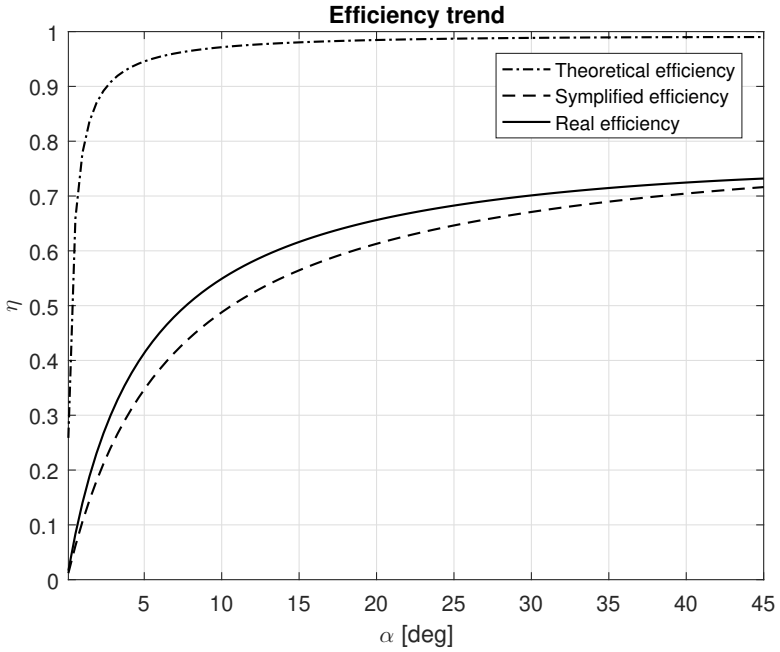

Figure 2.7: Ball screw's efficiency

However, due to slipping phenomena the real efficiecy is lower than the theoretical efficiency. Furthermore, even if the afore mentioned equations allow to evaluate in the best way the ball screw efficiency, it is necessary to specify that the slipping angle as well as the contact angle of the ball screw are not known in the pratical analyses. For this reason, the equations 2.5 and 2.6 are the most common used nowadays for a preliminary evaluation of the ball screw efficiency.

2.2 Ball screw's reference systems

As before mentioned, the ball screw is a complex system because it is closed in its internal part. In order to develop a detailed ball screw model, it is necessary to study the ball screw's kinematics on the basis of the previous studies [9].
In this section the reference systems utilized in the literature to analyze the ball screw's kinematics will be explained. In particular, usually four reference systems are introduced in the analysis, as depicted in Figure 2.8:

- $Ox'y'z'$ is the fixed reference system where the z' axis coincides with the screw shaft longitudinal axis

- $Oxyz$ is the rotary reference system whose motion coincides with the angular velocity of the screw shaft and with z axis aligned with the screw axis

- $O'tnb$ is the mobile reference system whose motion coincides with the balls motion. The origin of this reference system is the ball center (it is known as Frenet-Serret reference system)

In order to evaluate the actuator position, three coordinates will be utilized:

- The Ω angle, which represents the rotation of $Oxyz$ reference system with respect to $Ox'y'z'$
- The θ angle which is defined as the angle formed between the projection of the n-axis on the $x'y'$ plane and the x' direction
- The helix angle α

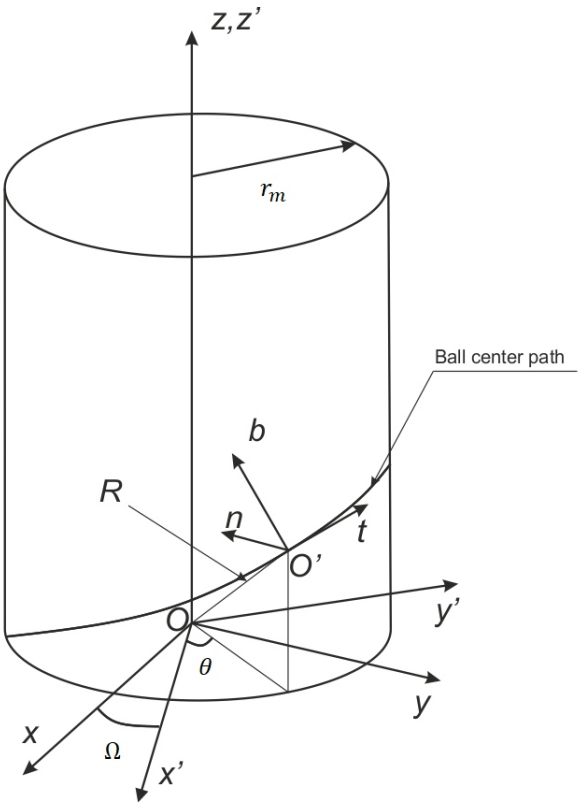

Figure 2.8: Reference Systems in ball screw

In order to understand the equations reported in the ball screw model, it is important to express a vector in one of these reference systems once known the coordinates in another one.
To move from the $Oxyz$ to $Ox'y'z'$ it may be possible to utilize the following matrix:

$$\begin{Bmatrix} \hat{x}' \\ \hat{y}' \\ \hat{z}' \end{Bmatrix} = \begin{bmatrix} \cos(\Omega) & -\sin(\Omega) & 0 \\ \sin(\Omega) & \cos(\Omega) & 0 \\ 0 & 0 & 1 \end{bmatrix} \begin{Bmatrix} \hat{x} \\ \hat{y} \\ \hat{z} \end{Bmatrix} = \mathbf{T_1} \begin{Bmatrix} \hat{x} \\ \hat{y} \\ \hat{z} \end{Bmatrix} \tag{2.13}$$

Therefore, to express the position of the ball center in the fixed reference system with respect to the mobile one, it may be possible to utilize the following expression:

$$\mathbf{R} = \begin{Bmatrix} r_m \cdot \cos(\theta) \\ r_m \cdot \sin(\theta) \\ r_m \cdot \theta \cdot \tan(\alpha) \end{Bmatrix} \tag{2.14}$$

Where r_m is the screw radius. The transformation matrix that allows to correlate $Oxyz$ and the Frenet-Serret reference system is expressed as $\mathbf{T_2}$:

$$\begin{Bmatrix} \hat{x} \\ \hat{y} \\ \hat{z} \end{Bmatrix} = \begin{bmatrix} -\cos(\alpha)\sin(\theta) & -\cos(\theta) & \sin(\alpha)\sin(\theta) \\ \cos(\alpha)\cos(\theta) & -\sin(\theta) & -\sin(\alpha)\cos(\theta) \\ \sin(\alpha) & 0 & \cos(\alpha) \end{bmatrix} \begin{Bmatrix} \hat{t} \\ \hat{n} \\ \hat{b} \end{Bmatrix} = \mathbf{T_2} \begin{Bmatrix} \hat{t} \\ \hat{n} \\ \hat{b} \end{Bmatrix} \tag{2.15}$$

Moreover, in order to study the contact, it is necessary to introduce another reference system centered in the contact point as depicted in Figure 2.9. As can be observed, there are two contact points, called A and B.

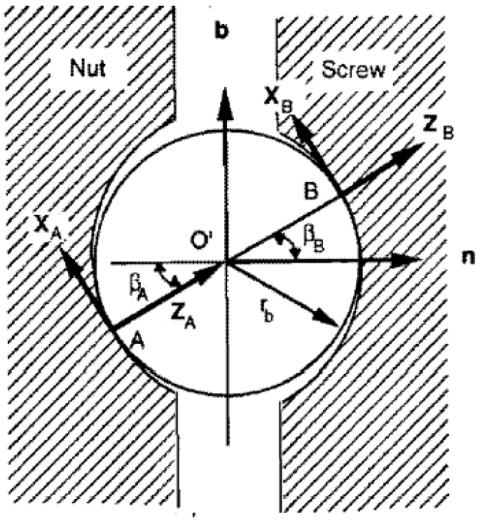

Figure 2.9: Reference Systems in the contact points [9]

These last represent the contact points between the ball and nut and ball and screw respectively. It has be noted that the z_i axis passes through the line joining the contact point and the ball center whereas the x_i and y_i axes form the plane tangent to the contact point. Thanks to the transformation matrix $\mathbf{T_{3i}}$, it is possible to pass from $O'tnb$ to the afore mentioned reference system and vice versa:

$$\begin{Bmatrix} \hat{x}_i \\ \hat{y}_i \\ \hat{z}_i \end{Bmatrix} = \begin{bmatrix} 0 & -sin(\beta_i) & \cos(\beta_i) \\ 1 & 0 & 0 \\ 0 & \cos(\beta_i) & sin(\beta_i) \end{bmatrix} \begin{Bmatrix} \hat{t} \\ \hat{n} \\ \hat{b} \end{Bmatrix} = \mathbf{T_{3i}} \begin{Bmatrix} \hat{t} \\ \hat{n} \\ \hat{b} \end{Bmatrix} \tag{2.16}$$

As afore explained, these equations will be useful in the ball screw model. Indeed, in order to evaluate the driving force starting from the driving torque provided by the motor, the before mentioned matrixes will utilize to pass from a reference system to another one. Once these reference systems were analyzed, it is necessary to understand how wear mechanisms affect the ball screw's parameters. Therefore, in the next section a wear analysis of ball screw is reported, in order to understand how the wear mechanisms can be simulated in the Simulink environment.

2.3 Wear analysis of ball screw - a case study

Thanks to the studies conducted by Wei et al. [11] a theoretical analysis of the ball screw's kinematics can be carried out. As afore-mentioned, by providing an offset pitch it is possible to obtain a preload in a ball screw with a single nut. The offset value changes with the applied axial load, which is symmetric respect to screw axis for hypothesis; for this reason, all the balls sustain the same load conditions and therefore the kinematical analysis can be performed for one pairs of balls [11]. In the light of this assessment, the kinematical analysis can be conducted by observing the Figure 2.10, where it is possible to observe the contact behavior of a ball screw when an axial load lower than preload is applied.

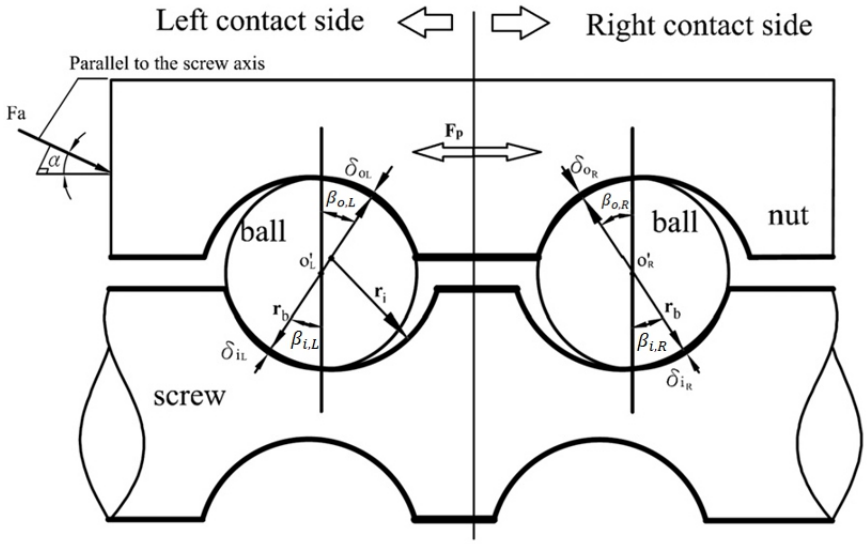

Figure 2.10: Contact behavior when the axial load is lower than preload [12]

As it may be possible to observe in the figure, when an axial load is applied, an elastic deformation δ_i at the left end of the nut is formed, creating an elliptical contact area according to Hertz contacts theory. The angle formed between the n-axis of the ball and the line joining the center of the elliptical area and ball center is the contact angle β_i. If no axial load is applied, the contact angle of the nut β_o is equal to the contact angle of

the screw β_i; on the contrary, if an axial load is applied to the ball screw, the two contact angles are different and for this reason it is necessary to underline with the subscript "L" and "R" the elastic deformations of the left and right track, respectively. Obviously, due to the applied preload in the ball screw, the right track ball will incline in the leftwards direction by an angle β_o and the left track ball in the rightward direction by the same angle [11].

After applying an axial load less than the preload, the contact angles between both ball-screw and ball-nut in the left track ($\beta_{i,L}$ and $\beta_{o,L}$, respectively) will reduce because the contact center will move towards the n-axis, whereas the contact angles in the right track ($\beta_{o,R}$ and $\beta_{i,R}$) will increase, because the contact center will move far away to the n-axis [11]. This situation is depicted in Figure 2.10.

When the axial load approaches the preload, the contact angles in the left track become 0° and therefore the elastic deformations (δ_{iL} and δ_{oL}) disappear. Finally, if the axial load becomes higher than the preload, the deformations in the left track move to the right side of the n-axis. So, this theoretical analysis of a preloaded ball screw indicates that a solution of several parameters does not exist when the axial load approaches the preload, due to the abrupt change of the angle β_{oL} [11].

To have a complete evaluation of the wear mechanism in the ball screw, an accurate analysis of the surface's roughness should be carried out. Generally, it is well known that the ball is harder and smoother than the raceway, therefore the total roughness of the ball-raceway system can be calculated as a composite roughness. The Figure 2.11 shows the raceway roughness, which is usually fabricated by grinding process. Moreover, the roughness normally is not constant along the different directions.

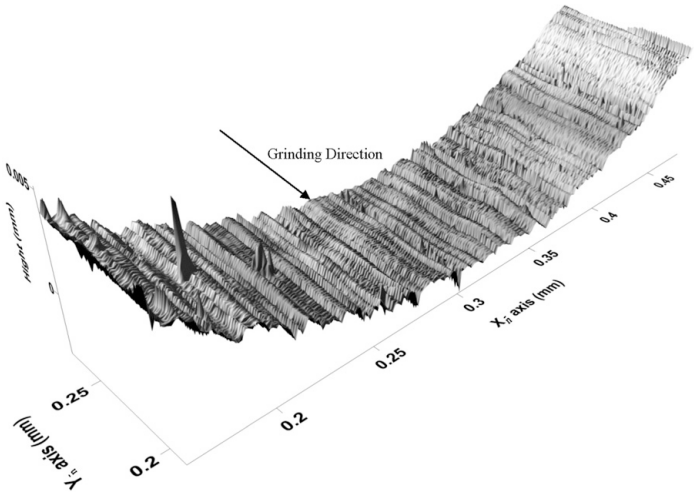

Figure 2.11: Representation of raceway roughness [12]

As the Figure 2.11 depicts, the raceway shows several imperfections that can cause wear mechanisms and degradation. In order to compute the degradation effects during the time, thanks to the reference study [12], the wear rate of each contact surface can be computed as:

$$\delta_{Wt} = E_c \cdot \dot{N} \cdot \Delta H \tag{2.17}$$

Where E_c is the effective contact ratio, $\dot{N}$ is the wear frequency whereas ΔH is the depth of an asperity. The first one depends on the ratio between the plastic and normal contact area:

$$E_c = \left(\frac{A_p}{A_n}\right)^{\frac{1}{2}} \tag{2.18}$$

Moreover, $\dot{N}$ depends on the relative speeds between the contact surfaces whereas ΔH can be computed on the basis of the geometry of the contact zone. In this thesis only the results of the experiments carried out in the cited article will be analyzed. For a deeper analysis, it is suggested to refer to [12].

2.3.1 Wear analysis

By referring to equation 2.17, to study the trend of wear rate it is necessary to evaluate three parameters:

- The effective contact ratio E_c
- The wear frequency $\dot{N}$
- The depth of an asperity ΔH

First of all the contact ratio is analyzed, which depends on the effective contact area formed between the two surfaces. In the Figure 2.12 the normal force and contact area are plotted with respect to the axial load for two rotational speeds ($31.4\,rad/s$ and $314.2\,rad/s$) in the left and right vertical axes respectively. It may be possible to observe that in the right contact side the dimensionless force is higher than the left track and it increases slowly. Moreover, the force decreases in the left side with high slope. Indeed, according to the kinematical analysis of a preloaded ball screw [11], the contact area in the right track increases with the raising of the axial load and the opposite phenomenon occurs in the left track. For this reason, both the dimensionless force and normal contact area have the same trend. Moreover, the ball-nut contact area is greater than the ball-screw. This trend is caused by the geometry of the contact surfaces, which are both concave between the nut and the ball and concave and convex in the contact between the ball and the screw [12]. This geometry's differences allow to understand why the normal contact area of the ball-nut is always higher than the ball-screw. Therefore, the Figure

2.12 permits to predict that the wear rate in the ball-screw contact should be higher than the ball-nut contact, because higher normal contact area leads to a lower wear rate. Naturally, this hypothesis is valid if the relative speeds in the two contact areas are equal. Indeed, it is known that the wear frequency $\dot{N}$ depends on the relative speeds in the contact area.

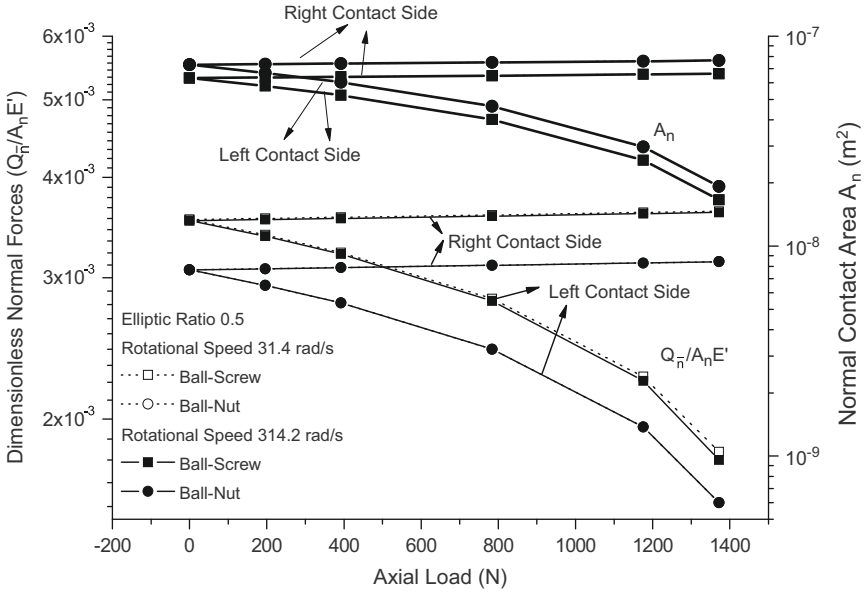

Figure 2.12: Dimensioneless Normal force and Normal contact area with respect to the axial load [12]

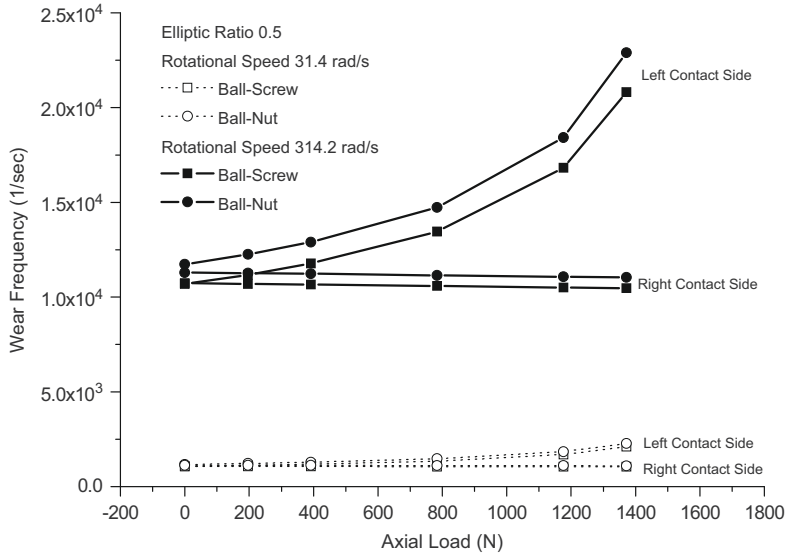

Figure 2.13: Wear frequency with respect to the axial load [12]

Obviously, for similar relative speeds the wear frequency is higher if the contact areas are lower. Since the relative speeds are similar in both contact sides then the wear frequency in the left contact side is higher than the right contact side, as it is possible to observe

in Figure 2.13 [12]. In fact, the contact areas are lower in the left contact side rather than the right contact side. Moreover, it may be possible to observe that this variable is higher in ball-nut than ball-screw, because the relative speed in the ball-nut contact is slightly higher than ball-screw contact. As can be found by observing Figure 2.13, the differences of the wear frequency between the left and right contact side become higher when the rotational speed increases. In fact, by increasing the velocity, a growth of the relative speeds occur and therefore the differences between the wear frequency of the two contacts side are more marked.

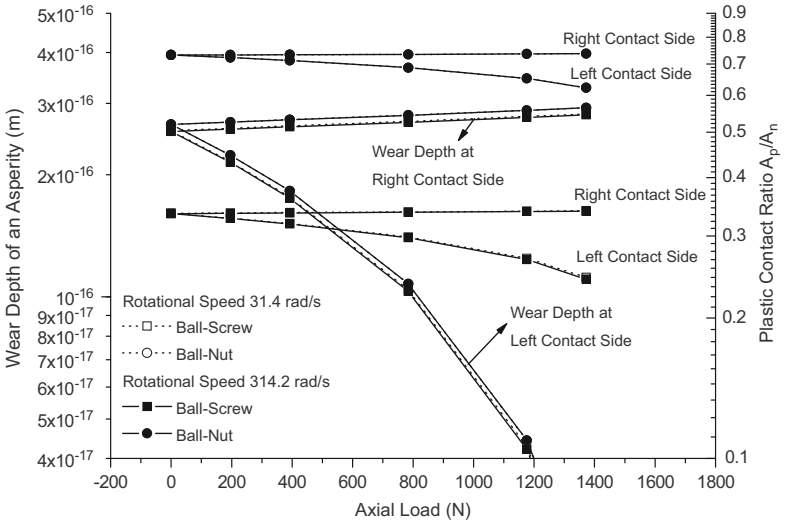

Figure 2.14: Wear depth of an asperity and plastic contact ratio trend [12]

Finally, in order to evaluate the wear rate, the wear depth of an asperity is analyzed. By comparing the trend of Figure 2.14 with the Figure 2.12, it is possible to conclude that the dimensioneless force is the major factor that affects the wear depth of an asperity [12]. Moreover, the plastic contact ratio in the ball-nut contact is always higher than the ball-screw contact, because the nut's roughness is higher than the screw in this case study. Therefore, the Figure 2.14 allows to understand the trend of the wear depth of an asperity on the left side and effective contact ratio E_c, according to equation 2.18.

As before mentioned , the wear rate depends on the contact ratio E_c, the wear frequency $\dot{N}$ and the depth of an asperity ΔH. Therefore, both E_c and ΔH are affected by the dimensionless contact force, whereas the wear frequency is major affected by the relative speeds and contact areas. The Figure 2.15 shows that the wear rate in the ball-nut contact is always higher than the ball-screw due to the larger value of ΔH and $\dot{N}$ [12]. Moreover, when the axial load raises, the contact force in the left side decreases such as the contact area. Hence, both E_c and ΔH decrease, but the wear frequency raises because a smaller contact area generates increased wear frequency. For this reason, the wear rate increases slightly with the raising of the axial load in the left contact side. Equally, in the right

contact side the plastic contact ratio and ΔH increase with raising the axial load, whereas the wear frequency slightly reduced. Then, also the wear rate in the right side increases when the axial load becomes higher.

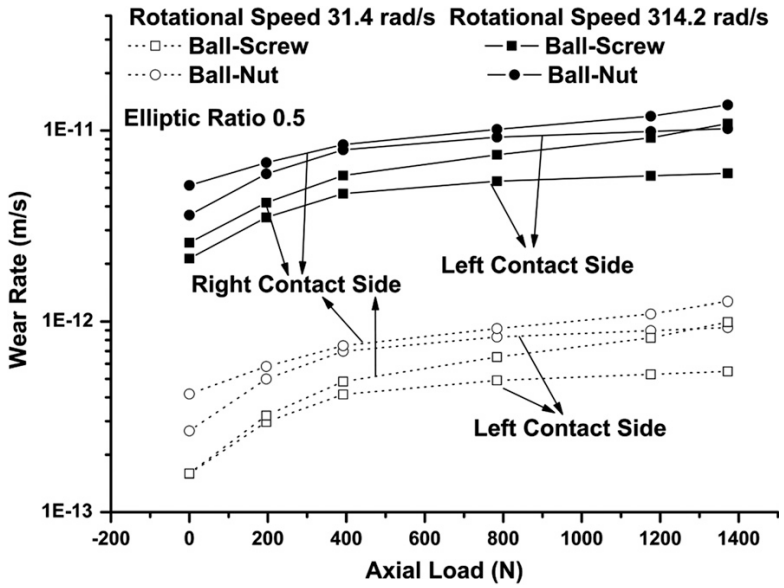

Figure 2.15: Wear rate trend [12]

Finally, by starting to the wear rate, it may be possible to calculate the wear depth formed into the ball during the acceleration-deceleration times as well as the preload variation. In particular, the wear depth can be evaluated as the product between the acceleration time and the wear rate previously computed. Furthermore, the preload loss can be computed as [12]:

$$\Delta P = K_{nut} \cdot \left(\bar{\delta_\lambda} - \delta_\lambda\right) \tag{2.19}$$

Where $\bar{\delta_\lambda}$ is the axial deformation considering the wear effects whereas δ_λ is the axial deformation only due to the axial load.

It may possible to observe in Figure 2.16 that for low stroke numbers the axial wear increases quickly, subsequently the trend becomes smoother; this behavior is known as running-in process. Moreover, when the speed increases the wear rate becomes higher such as the acceleration time, therefore the axial wear depth is greater. The preload decreases quickly for higher rotational speeds due to the higher acceleration time requested to reach the steady speed. To maintain a good accuracy of the ball screw it is necessary that the preload is at least the 10% of its initial value. Therefore, the ball screw's life has to be evaluated according to its working rotational speed.

In conclusion, this analysis allows to understand that the wear is not equal for all balls, because it changes depending on the considered side. For this reason, in order to obtain

an accurate evaluation of wear mechanisms, the microcontact zones for each ball should be analyzed. However, in this thesis a macroscopic point of view is proposed. In this respect, it is supposed to simulate the ball screw degradation by increasing the friction forces and the backlash.

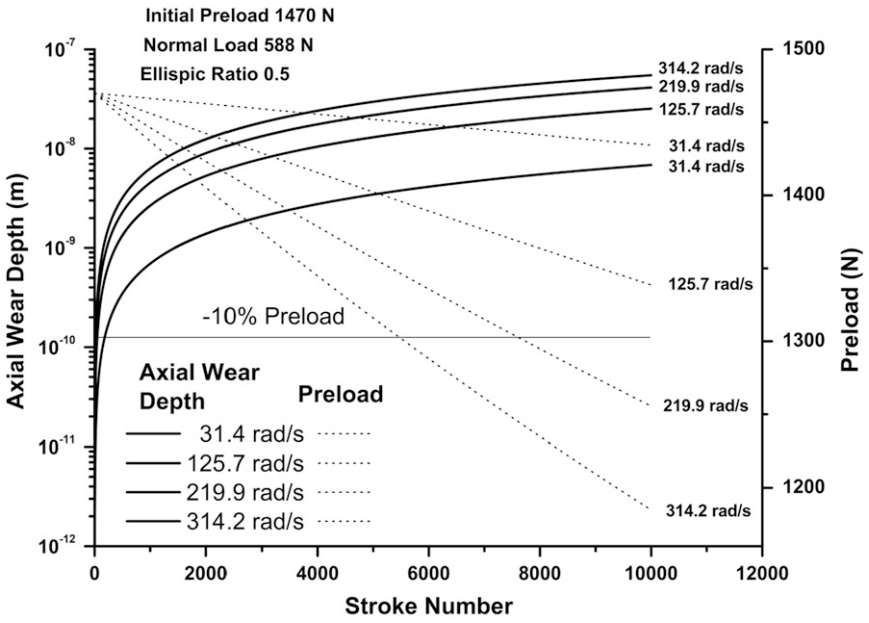

Figure 2.16: Axial wear depth and preload with respect to the stroke number [12]

Obviously, this last appears when the preload becomes null. According to [12], it is possible to hypothesize a linear decreasing of the preload force during the simulation time. In the next chapter the wear mechanisms that can affect the mechanical components will be deeper analyzed. Indeed, in this analysis the effects of wear mechanisms were considered but nothing has been said about root causes that lead to degradation effects.

Chapter 3

Wear Mechanisms

In this chapter the most known wear mechanisms will be explained, in order to understand the principal consequences that they lead to mechanical components. The first section provides an overview of the principal wear mechanisms. Successively, in the next sections the principal phenomena that affect mechanical components are treated. In particular, on the basis of [13], in this chapter the adhesive, abrasive, fatigue, oxidation, tribochemical and fretting wear will be explained, because they represent the most commonly degradation mechanisms that affect the mechanical parts.

3.1 Introduction

The wear mechanisms are defined as "*the phenomenon of progressive damage resulting in a loss of material*" [13]. It is very important to have a deep knowledge of wear mechanisms because they produce loss of material, by causing the mechanical components' failure. For the last consequence, it is quite understandable that the wear mechanisms are correlated with the maintenance's and technical diagnostic's field.
Therefore, it is important to monitor the degradation progress in order to reduce the maintenance costs, by improving the life of components. Furthermore, during the propagation of degradation mechanisms, the performances decrease because usually the wear is accompanied by an increasing of the friction force.
For the afore-mentioned reasons, the wear mechanisms have been studied in the course of the years, through the developing of models by which predicting the wear's behavior. However, these phenomena are very complex because the wear rate depends on numerous variables as environmental effects, type of wear mechanism, properties of the surfaces in contact, etc. Moreover, many mechanisms occur at the same time, hence it is necessary to take into account also this aspect [13]. The wear is usually classified on the basis of the wear rate.

In this respect, it is possible to distinguish two types of wear mechanisms:

- The most "dangerous" as adhesive and abrasion wear. Indeed, these last cause high wear rate and catastrophic failures. For these reasons, they should be avoided when they occur

- Mechanisms that occur with low wear rate as cavitation, corrosion, erosion or fretting. Although the wear rate is usually low, these types of degradations can represent the most important phenomenon that affects the part's life. For instance, the cavitation is the most important mechanism in turbines whereas bearing and seats suffer from fretting

Furthermore, the wear can be classified on the basis of the relative motion of contacting surfaces. Indeed, it is known that the most common motions are the rolling and sliding. However, the fretting and drilling can have several consequences too, by leading to performances deterioration. Furthermore, depending on the relative motion, the wear rates can be different. In fact, the degradation is caused by the relative speeds of the two bodies in the contact surfaces. For the same angular speed, it is quite understandable that the linear speeds will be different if the bodies' curvatures are not equal. Since the geometries of the contacting components are not the same in most cases, then slipping occurs in the contact surfaces. This phenomenon allows to understand that the micro-sliding represents the most important mechanism in tribological parts [13].
In the light of these issues, it may be possible to reduce wear effects by introducing lubricants between the contact bodies. However, the lubricant changes the contact behavior because several aspects that are disadvantageous in dry contact become positive. Furthermore, the particles and oxides that are usually adsorbed by the contacting materials can act as lubricant in several applications. For this reason, the dry contact hypothesis is not a reasonable assumption in most of cases [13].
As before mentioned, it is quite understandable that to improve the performances of mechanical components and reduce the degradation effects, the most common wear mechanisms have to be analyzed. In fact, depending on the analyzed case, it may be possible to identify a most suitable solution by which degradation effects can be minimized. Obviously, since many mechanisms act at the same time, then the phenomenon is more complex than the following analyses, but these studies can represent the basis of further considerations. In particular, this chapter analyzes the most common wear mechanisms as adhesive, abrasive, fatigue, oxidation and tribochemical and the fretting wear according to [13].

3.2 Adhesive wear

The adhesive wear is one of the most common and severe wear mechanisms in mechanical components. The adhesive wear is caused by the micro-junctions that occur in contact surfaces. In fact, the friction generates heat that causes welding between the asperities and, therefore, adhesions. These junctions are caused by covalent, ionic, hydrogen and Van Der Waals bonds. If the force of these bonds is as high to overcome the internal resistance of the material, a part of the weaker body detaches and it is held by the other surface. Due to this material film, several holes in the weaker surface and irregularities in the other body can be observed in the micro-contact zone. Obviously, after the material detachment, the contact is less smooth and in the next contacts the impacts will be more severe by promoting the growth of new debris [13].

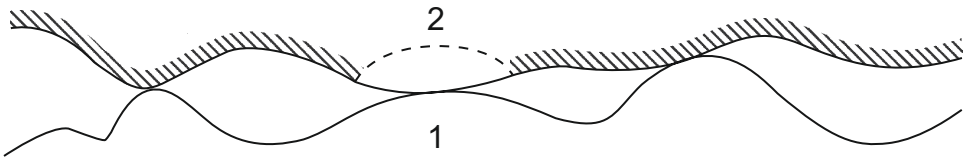

Figure 3.1: Adhesive wear mechanism [13]

As shown in Figure 3.1, a small fragment of the weaker body (which is represented in the shadow zone) detaches from the body 2 and attaches to the body 1. In order to compare the behavior of materials, Lancaster proposes a coefficient that represents the specific wear rate [13]:

$$k = \frac{V}{W} \tag{3.1}$$

Where V is the sliding distance whereas W is the normal load. The higher this index the more the adhesive wear affects the behavior of the analyzed material.

The adhesive wear is the most severe phenomenon in materials that have similar solubility and chemical affinity. Moreover, the toughness of the material strongly affects the wear rate during time. In fact, it was found that materials with low toughness tend to form bigger plastic deformation areas. Therefore, the areas of material where detachments may occur are larger.

Due to the before mentioned reasons, the ways to reduce the adhesive wear are quite understandable. In fact, by using materials with low chemical affinity or with high toughness it makes possible to reduce the adhesive wear in the contact surfaces, by improving the life of the mechanical parts.

3.3 Abrasive wear

The abrasive wear is a complex phenomenon that affects several coupling systems. Indeed, the abrasive wear itself is not a single process but it depends on many physical processes and variables (as dynamics of contacts and mechanical properties).
The most common abrasive wear occurs when a particle slides over two surfaces, by causing plastic deformation or materials detachments in the weaker surface. These particles may be inclusions, come from external environment or they can be the product of interaction between two surfaces. The particles can form or not debris; the first case is known as cutting mode whereas the second one is referred as plowing. This last causes plastic deformations in the weaker surfaces by leading to irregularities and grooves. The grooves may host external debris, by promoting the abrasive wear when new sliding contacts will occur. These mechanisms are common in high toughness materials such as steels and many metals.

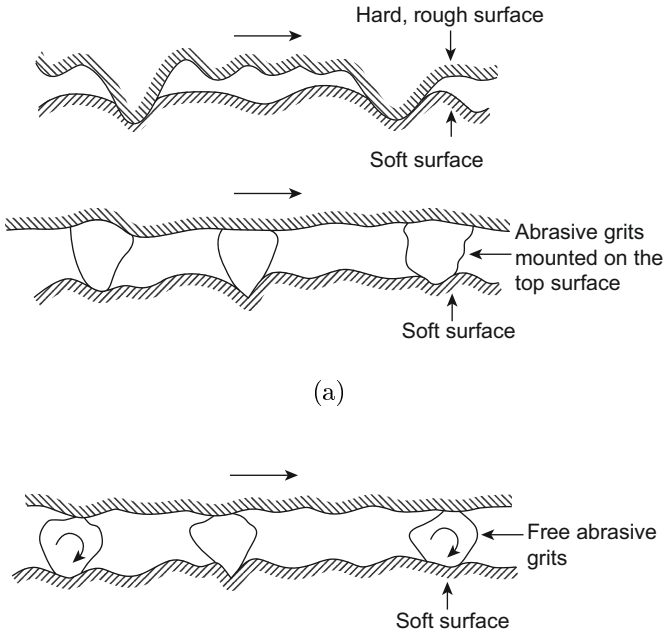

Figure 3.2: Abrasive wear mechanism [13]

Usually, the abrasive wear is divided in two and three-body wear. The first one occurs when debris are placed between the two contact surfaces, by leading to wear in the weaker material. However, it is possible that the debris form an interface between the contact bodies, by creating a third body and damaging either or both surfaces. This last case is known as three-body wear. Usually the three-body is less dangerous than the two-body wear because the debris surface tends to form the contact in the easiest possible

way, according to the minimum energy principle [13]. In the Figures 3.2(a) and 3.2(b) the two-body and three-body wear mechanisms are depicted, respectively. The two-body mechanism occurs in many mechanical processes as grinding, cutting and machining. On the contrary, the three-body abrasive wear occurs especially in polishing and abrasive-free lapping [13].

In order to reduce the abrasive wear, it may be possible to decrease the toughness dissimilarities in the contacting surfaces, because it is necessary that a body is stronger than other to have abrasion. At the same time, if the toughness difference is very high, the weaker material is subjected by plastic deformations, by avoiding abrasion wear mechanism but not eliminating irregularities in the softer surfaces.

3.4 Fatigue wear

As it is known, the fatigue is a break mechanism that affects all mechanical components. Generally, the fatigue wear can be divided in low cycle fatigue and high cycle fatigue. The first one consists in high stresses which are repeated for low cycles whereas in the high cycle fatigue there are small stresses for elevated number of cycles. Usually, the fatigue wear starts to crack formations that lead to wear mechanisms of the material with a consequent losing in performance.

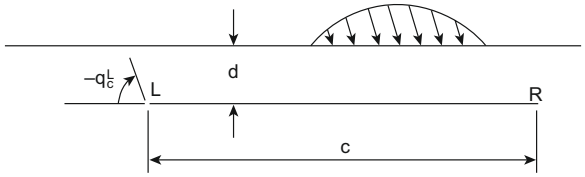

(a)

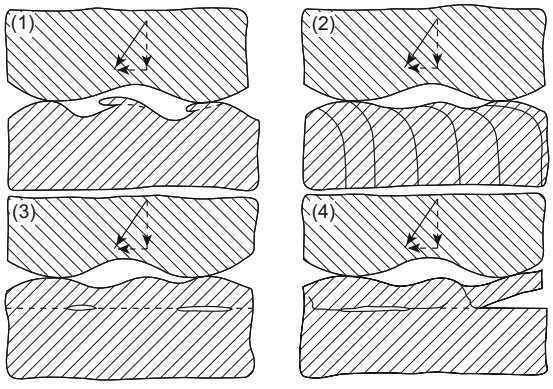

(b)

Figure 3.3: Subsurface zone (a) and delamination wear mechanism (b) [13]

An accepted theory that allows to explain the fatigue wear mechanism was developed by

Suh [13]: the so-called delamination theory of wear. According to this last, the fatigue wear starts because of repeated shear stresses that grow in the subsurface, where the loads are higher. Therefore, there are many stress cycles that lead to the development of plastic deformations along the parallel direction of the surface. When the crack reaches a critical size, there is a material separation shaped like a sheet, that slide under the two surfaces leading to stress accumulations in the back part of the contact. Then, the delamination leads to the development of pits on the two contact surfaces (indeed, this process is known as pitting in ball bearings and gears).
As it is possible to observe, in the Figure 3.3(a) the subsurface zone is represented whereas the Figure 3.3(b) depicts the delamination wear mechanism. Indeed, it may be possible to observe that the stresses create a small crack (that can be observed in the third picture of Figure 3.3(b)) that propagates in parallel to the surface direction.
This process only occurs when the stresses are slow and repeated for many cycles. Indeed, if the stresses are high, the principal wear processes are the adhesive and abrasive mechanisms. This consideration can be explained as follow: when there is a removed part of material due to wear mechanism, the high stresses tend to change the location by avoiding the grow of the cracks. For this reason, the fatigue wear does not affect the nonlubricated sliding contacts as well as contacts with high stresses. On the contrary, this wear mechanism is most common in rolling and lubricated contacts, where the local contact forces are quite low [13].

3.5 Oxidation and Tribochemical wear

The tribochemical wear is caused by the reaction products formed locally between the contact surfaces. It is necessary to understand that between two contact surfaces many chemical reactions can lead to tribochemistry. In the Figure 3.4 the tribochemical wear process can be observed; this last causes the formation of wear debris due to the reactions between meting materials [13].
Obviously, these reactions can appear only under specific load, environmental and temperature conditions. However, it is known that the tribochemical process is not ever associated to an undesired phenomenon. Indeed, many lubricants are composed by additives; the reactions of these last are based on right on tribochemistry. The mixed lubrications regime depends on the tribochemical reactions that can occur only under specific environmental and load conditions. Therefore, the optimal material choice is a compromise between the material characteristics, chemistry and operating conditions. Furthermore, if a deep study of material features is not conducted, a bad behavior of the contact surfaces it is expected [13]. Therefore, it is quite easy to understand that a proper choise of the material constitutes an essential step to obtain a careful design.

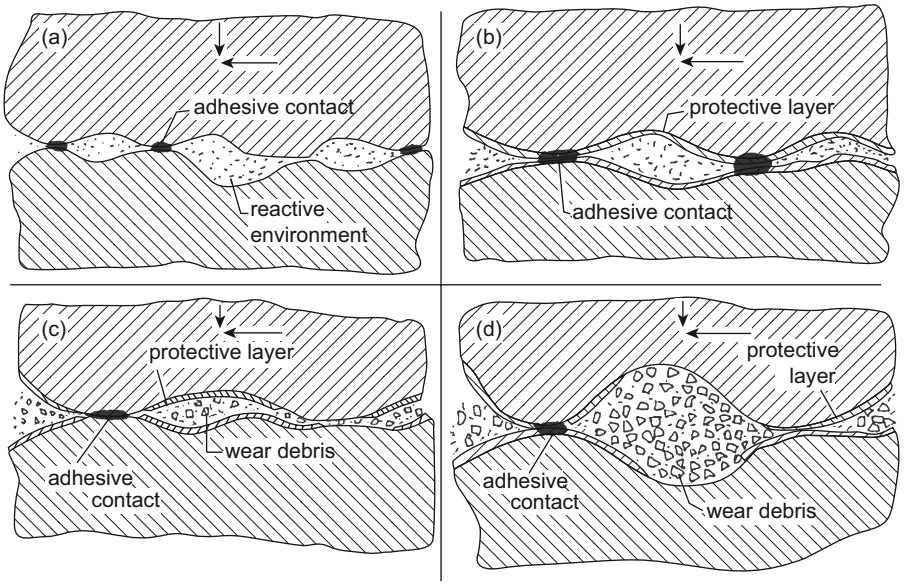

Figure 3.4: Tribochemical wear process [13]

For the afore-mentioned reasons, the tribochemical wear principally depends on the velocity with which the surface layers form and the material strength properties as ductility, strength, hardness, etc. Furthermore, this wear process is strongly affected by the properties and structure of the oxides. Indeed, the Fe_3O_4 leads to a lower wear rate than Fe_2O_3 [13]. Therefore, in order to avoid the tribochemical wear process, it is necessary to choose accurately the material according to the working environment.

3.6 Fretting wear

The fretting wear is one of the most complex wear mechanisms. In particular, the fretting mechanism is defined as "*any situation in which the contacts between materials are subjected to a low amplitude oscillatory motion that is lower than a few hundred* μm" [13]. Due to the low relative motion, the debris remain included between the two contact surfaces by causing degradation effects.

The fretting mechanisms can lead to three different damages' modes. The first one is caused by the chemical reactions between the material and environment, that lead to corroded debris. The second one happens when low stresses of many cycles cause fretting conditions in few micrometers of amplitude. Finally, if the amplitudes are very high, the slip is the most important phenomenon of the contact: this mechanism is the third fretting damage's mode. The fretting wear mechanisms is known in several fields of mechanical and material engineering. Indeed, the faults in helicopters, turbine disks or supporting joints in trains are caused by wear fretting mechanism. In the light of this assessment, it is very important to study deeper than other mechanism the fretting wear.

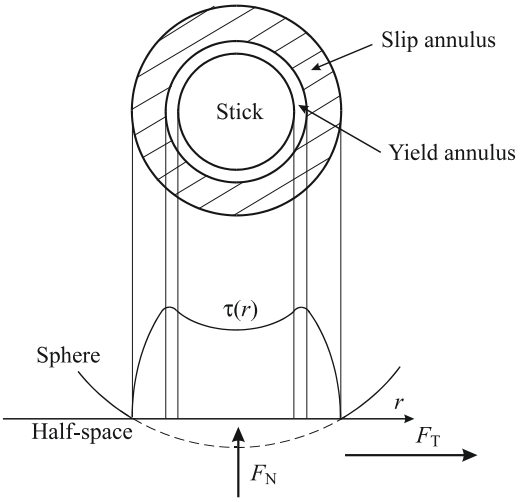

Figure 3.5: Shear stress trend according to the elasto-plastic theory [13]

In order to study the fretting wear, it is necessary to analyze the contact zone between the two sliding surfaces. In particular, as depicted in Figure 3.5, it may be possible to identify three contact zones [13]:

- The inner zone that is characterized by elastic deformations and where no slipping phenomena occur
- An anulus zone where plastic deformations occur but the asperities do not experience fractures
- An outer zone where the asperities are subjected by fractures: in this zone slipping between contact surfaces occurs

Therefore, it is not difficult to understand that the contact behavior can change on the basis of the largeness of each zone. Indeed, it may be possible to distinguish different regimes [13]:

- Stick regime. In this case the largeness of the stick zone is predominant. This type of regime can be observed when the displacement amplitudes are very low. In this type of contact the deformations are elastic: therefore, there are not cracks and damages in the asperities and the dissipated energy is null in one cycle, as depicted in Figure 3.6 (a). For this reason, this wear mechanism is called low-damage fretting
- Partial slip regime. When the oscillations increase, a plastic zone appears in the contact between two surfaces. In this case the $\delta - F_T$ curve (where F_T represents the applied tangential force) has a restricted hysteresis cycle, as depicted in Figure

3.6 (b). This regime is characterized by low oxidation effects; however, the cracks grow with high acceleration, by resulting in reduction of the material's fatigue life

- Gross slip regime. This phenomenon occurs when the displacements reach a critical value. Indeed, when the condition $F_N = \mu \cdot F_N$ is verified, there is an abrupt change in the friction coefficient value. Indeed, it passes from the static friction coefficient to the dynamic friction coefficient. In this case the largeness of the $\delta - F_T$ curve is very high. This fretting wear regime is the most dangerous because it leads to high wear rate which is associated with oxidations mechanisms that make more dangerous the phenomenon. However, the fatigue wear does not occur because the cracks growth is avoided due to the wear mechanism itself that removes the contact fatigue crakcs

- Reciprocating wear regime. This regime occurs when the displacement amplitude becomes so high that the wear rate and mechanisms are equal to the reciprocating wear

- Partial slip regime. This last occurs when both gross and partial slip regimes can be observed. For this reason, the material micrography shows typical cracks of both fatigue and fretting wear. This particular regime is characterized by an elliptical shape of the hysteresis trend and the alternation between gross and partial slip regimes

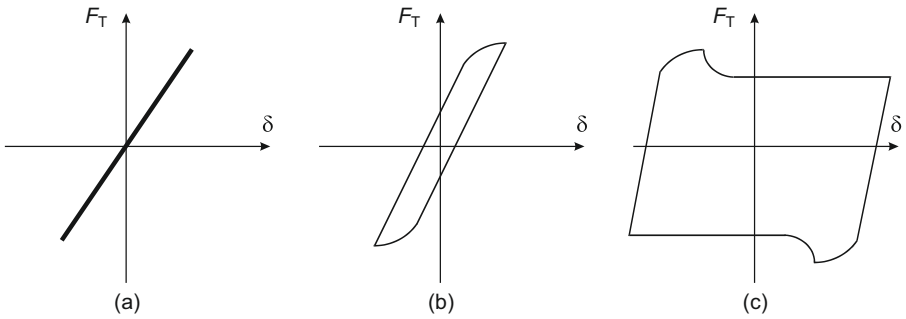

Figure 3.6: $\delta - F_T$ curve in the three analyzed cases [13]

For evaluating the transition from the stick regime to the partial slip regime it is possible to observe the hysteresis curve. Indeed, if the dissipated energy is null, the regime is stick. The first displacement in which the energy is not null represents the critical value where the transition between stick and partial slip regime occurs. However, the transition from the partial to the gross slip regime is more difficult to recognize. For instance, it is possible to observe the magnitude of the friction force: the point where this value

reaches a maximum over that an abrupt decreasing can be observed (due to the transition from static to dynamic friction) represents the δ_{cr} where the transition occurs. In [13] an energetic method to identify the transition from partial to gross slip regime is also proposed. In the light of this analysis it is possible to conclude that the fretting wear can be dangerous for mechanical parts and despite of the afore mentioned mechanisms, it is difficult to mitigate since occurring whenever two surfaces have relative motion.

Therefore, this analysis allows to understand the principal consequences of the most common wear mechanisms. In particular, the abrasive and adhesive wear represent the most common cause of faults and failure in mechanical components, because they are characterized by high wear rate. However, the fatigue wear as well as the fretting wear can lead to catastrophic disasters too. Generally, it is possible to conclude that wear mechanisms lead to material removal; for this reason, they cause axial plays, high frictions and decreased performances. Furthermore, the trend of wear mechanisms is not linear during time, because the formation of debris promotes higher wear rate. Therefore, on the basis of this study, it is supposed to simulate the wear mechanisms by increasing the friction and backlash with an exponential trend. Indeed, in the developed model in this thesis the wear mechanisms are considered under a macroscopic point of view, by taking into account only their effects and neglecting their root causes. However, this chapter can represent the basis for further analyses and possible developments of the explained model.

Once wear mechanisms and degradations were explained in detail, in the following chapter the framework and principal concepts of Health and Usage Monitoring Systems are explained. Indeed, it is now important to understand how the development of these mechanisms can be detected before they can lead to mechanical jamming or unacceptable performances of the actuator.

Chapter 4

Health and Usage Monitoring Systems

In this chapter the principal characteristics of Health and Usage Monitoring Systems are analyzed. The first section explains the principal HUMS concepts as well as the advantages that HUMS's architecture can bring to aircrafts. After that, the HUMS framework is analyzed, in order to understand which are the principal components that allow to monitor the flight parameters stored by the sensors such as position, current, angular velocity, etc. Subsequently, the third section treats the principal HUMS methods, with an emphasis on the most commonly used nowadays. Finally, the last section deals with the most commonly used sensors by which it is possible to predict faults as well as the remaining useful life of mechanical components.

4.1 HUMS Concepts

The principal HUMS goals are the increasing of the availability and readiness of the aircraft, enhancing safety and reducing operating costs. As mentioned in the first chapter, the electromechanical actuators are struggled to be employed in primary flight control applications due to the mechanical jamming and degradation of performances caused by wear mechanisms and thermal behavior issues [6]. In order to overcome these problems, nowadays the trend is to employ a Health and Usage Monitoring System in EMAs, by which faults as well as the Remaining Useful Life (RUL) of the actuator can be predicted. Indeed, thanks to a HUMS, the EMA can benefit from several advantages as [6]:

- The maintenance works can be more efficient because the faults prediction allow to schedule possible faults
- Possible problems can be avoided without removal of equipment, thanks to a proper use of the system
- Reduction of downtimes because many inspection intervals can be eliminated

- The prediction of possible faults avoids other following damages that can be caused by the first fault
- Decreasing of direct and indirect costs as well as increasing of the remaining useful life of mechanical components through a proper use of them

It is important to observe that the complexity of the system depends on the number of data that HUMS collects and the number of parameters which HUMS monitors. In fact, there are simple ones, which measure only few parameters and whose weight is about $1\,kg$ and others monitor systems which can record 130 parameters with a greater weight [14]. Indeed, the HUMS can store several parameters as acceleration, aircraft position, flying hours, temperature and pressure parameters, etc. Obviously, the HUMS monitors several parameters which should be chosen according to the fault types. Furthermore, these last should be sensitive enough and they have to be steady during the flight [15]. Then, thanks to flight parameters, it is possible to obtain different condition indexes by which the aircraft health assessment can be carried out. However, in order to have an overview of the health state of the aircraft, all condition parameters have to be studied together. As before mentioned, the most important HUMS goals are the identification and isolation of the occurred faults, for instance by using models by which possible aircraft faults/failures can be predicted. In fact, HUMS concept includes two modules [6]:

- Health Monitoring
- Usage (Prognostic)

The first one allows to comprehend the component's diagnosis and isolation of faults. On the contrary, the Usage part has to predict the component's RUL on the basis of several methodologies. A more detailed description of these two concepts is reported in the following subsections.

4.1.1 Health Monitoring

The health monitoring consists of diagnosis and isolation of faults. Indeed plays, degradation can be useful information to detect possible issues in the EMA. The health monitoring represents a useful way to identify possible faults before they could happen [16]. In order to do that, different sensors are employed, some of which are already mounted in the aircraft's framework whereas others have to be insert appositely. In general, the health monitoring improves the actuator maintainability and it allows to monitor the EMA during its life cycle. Therefore, the health monitoring should anticipate EMA jamming failure, locate and identify failures in order to have a deeper knownledge of the issues that can affect mechanical system.

In order to identify the most severe faults that can occur in EMA, it is possible to utilize the Failure Mode and Critical Effect Analysis (FMECA). Thanks to this methodology, it is possible to prioritize the most severe faults, for instance by allocating a coefficient from 1 (worst case) to 4 (best case) at each faults characteristic, as reported in the Figure 4.1 [17]. In particular, in the figure the frequency (F), severity (S), testability(T), and replaceability of each fault (R) are analyzed.

COMPONENT	MAIN FAILURE MODES	SCORE				
		F	S	T	R	TOT
EPU	Power MOSFET thermal failure	3	2	4	1	10
Electric motor	Turn-to-turn short	1	2	4	1	8
	Turn-to-phase short	2	2	4	1	9
	Turn-to-ground short	2	2	4	1	9
Bearings	Scoring	3	1	3	1	8
	Indentation	4	1	3	1	9
	Wear	4	4	3	1	12
	Pitting	4	4	3	1	12
	Electric erosion	3	2	3	1	9
	Tracks crack	3	1	3	1	8
Gears	Crack	3	1	3	1	8
	Wear	4	4	4	1	13
	Pitting	2	3	3	1	9
Power screw	Scoring	2	1	3	1	7
	Wear	3	4	4	1	12
	Return channel deformation	4	1	3	1	9
	Indentation	3	1	3	1	8

Figure 4.1: FMECA analysis for a EMA [17]

As it is possible to observe in the Figure 4.1, several types of failures modes can affect the EMA. In particular, in the figure the faults of EPU (Electronic Processor Unit), BLDC motor, bearings, gear box and power screw are reported. In particular, the motor failures mode show high frequency but usually they cause only degradation in performance but no EMA loss. On the contrary, the mechanical failures lead to the loss of the whole EMA [17]. By focusing in this work of thesis, the failures of power screw are underlined in the figure. As it is possible to observe, the power screw scoring is the failure mode that shows the lowest score as possible. Furthermore, the wear shows a high total score but the replaceability is the lowest value. Indeed, wear mechanisms has a low frequency because the degradation develops continually during the time. However, when they occur it is necessary to replace the power screw because the actuator's performances become unacceptable.

4.1.2 Usage (Prognostics)

There are several differences between the diagnostic and prognostic algorithms. As explained before, the principal aim of the diagnostics is to identify the root causes of a problem, situation or failure when it has just happened. On the contrary, the prognostic goal is to predict the future on the basis of several rational studies [18]. In the course of the years many studies are conducted to minimize the downtimes due to wear and degradation effects in mechanical components. The Figure 4.2 represents the principal differences between diagnostic (Health Management) and prognostics (Usage).

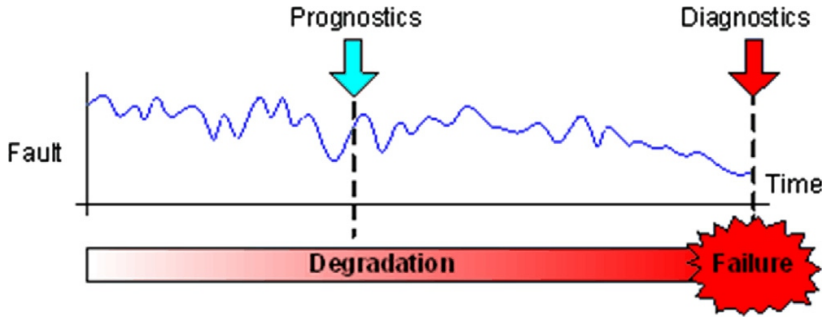

Figure 4.2: Differences between prognostics and diagnostics [18]

The prognostic operates during the degradation mechanisms and it allows to forecast the Remaining Useful Life (RUL) of the monitored parts. As it can be observed, the diagnostic arrow is represented in the final part of the degradation mechanism, when the failure has just occurred. In fact, the diagnostic aim is to identify the principal cause of the failure. For this reason, the time does not have a crucial role because the emphasis being placed on determining the main parameters that lead to the failure [18]. Since the prognostic is based on the prediction of possible faults before they can occur, then the time has a crucial role in this discipline.
The prognosis is used to predict possible failures by using of patterns that can simulate the behavior of EMA. In order to do that, many data are necessary to develop the model continuously; however, the motor data and the features of other components are usually not completed and bench not available. Therefore, firstly a preliminary model should be made and it can be developed gradually utilizing the forgiven data. By obtaining the final model it will be possible to fix the actuator behavior by means of simulation techniques as well as increasing the EMA efficiency by developing prediction and monitoring algorithms [6].

4.2 HUMS Design

As explained before, the HUMS has to detect possible faults as well as predicting the RUL of the analyzed aircraft component. For this reason, the HUMS's design has to be developed in order to satisfy these requests. Fundamentally, the HUMS's framework consists in an airborne and a ground system. The airborne system is composed by a sensing module and a data acquistion module by which the parameters can be stored. For instance, the Figure 4.3 depicts a HUMS structure mounted on a ultra-light aircraft based on FBG (Fiber Bragg Grating) sensors for storing the applied loads on aircraft's components.

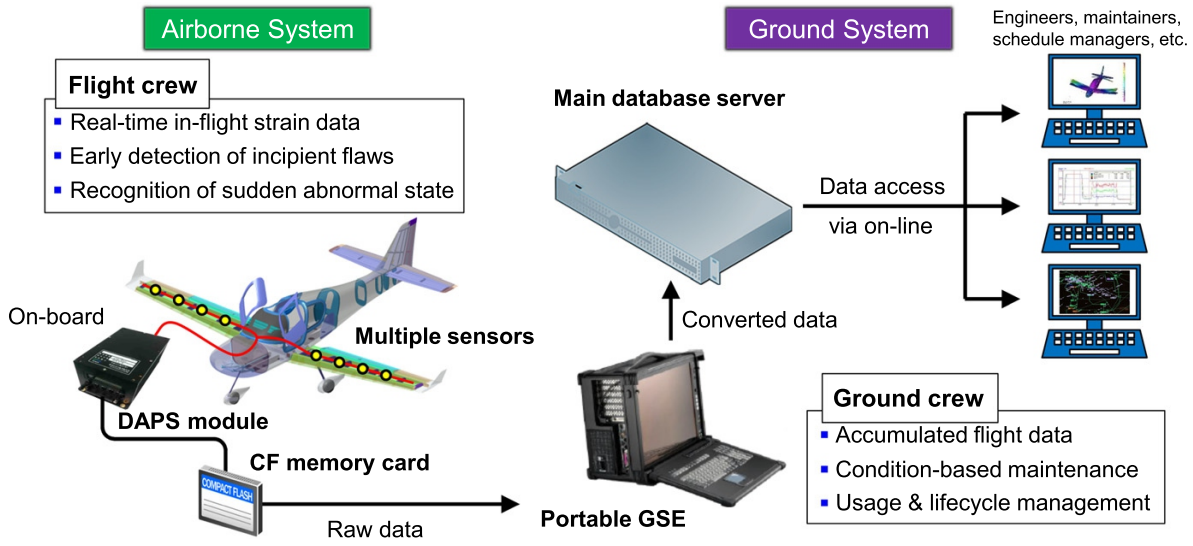

Figure 4.3: HUMS structure for a ultra-light aircraft [19]

As the Figure 4.3 shows, the data stored from the sensors are forwarded to the DAPS module (the acquisition module in this case). The acquired parameters (wavelengths from FBG as well as altitude, roll, pitch and yaw angles) are stored in a memory card. After the landing, these data are analyzed by a portable ground support equipment, in order to understand if the stored parameters can be useful under a diagnostic and prognostic point of view. If this requirement is satisfied, the data are uploaded to the main server of the ground system, where they can be utilized for post-processing analyses [19]. Even if this example reports a HUMS for a ultra-light aircraft, the HUMS structure is similar also for the large commercial aircrafts.
Moving from the HUMS design, it is necessary now to explain which are the HUMS's methods by which an EMA's health assessment and prediction of its RUL can be carried out. These last will be explained in the following section.

4.3 Health Monitoring Methods

In the simplest way, a health monitoring method compares the sensors output with a fixed threshold over that a fault can occur. However, the most sophisticated monitoring methods allow to monitor the aircraft trends of performance, the differences from the healthy operating ranges, in order to predict failures to schedule in the best way the maintenance operations [20].

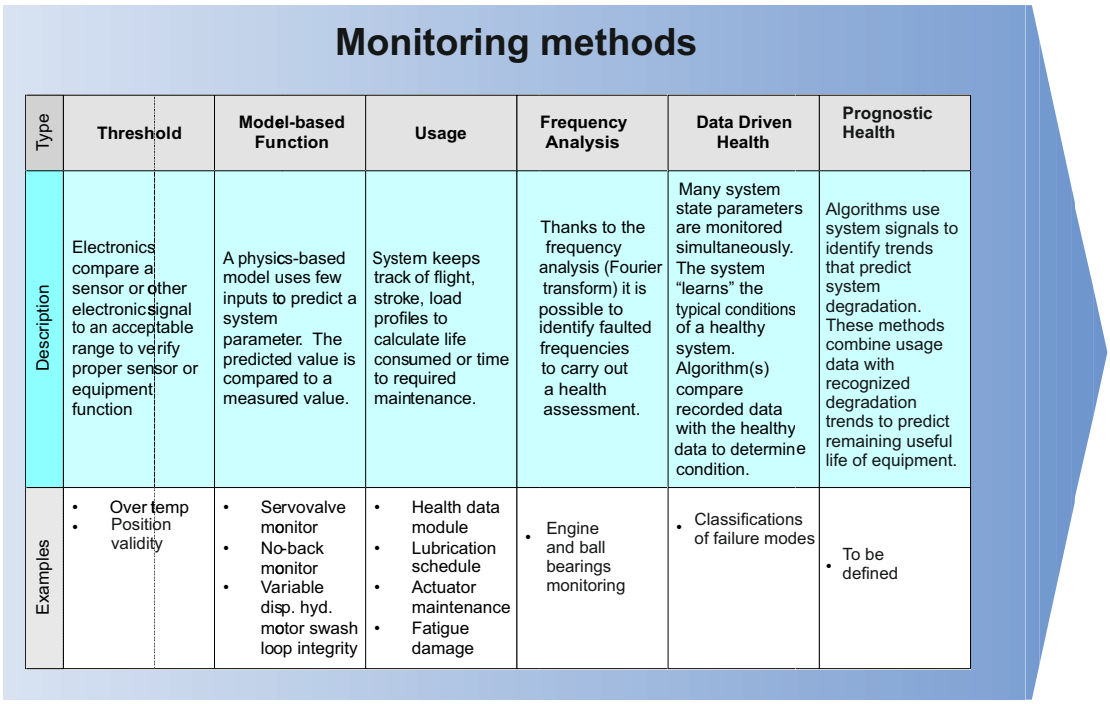

Figure 4.4: Overview of the principal Health Monitoring Methods [20]

The Figure 4.4 shows the principal monitoring system, starting from the threshold type and finishing to the newest monitoring systems, such as the Prognostic and Health Management (PHM). As it will be explained below, each methods has several characteristics that can make the analyzed methodology most suitable for specific applications. For instance, the model-based function is very useful when it is necessary to monitor a servovalve. On the contrary, the frequency analysis is commonly used for the bearing and engine monitoring. The following subsections treat the reported monitoring systems with except to the Usage monitoring. Indeed, this last has already treated in the previous sections.

4.3.1 Threshold Monitoring

The threshold method is the most common monitoring system in the flight control today. In fact, it works by comparing the value of an available signal to a known threshold value over that a fault can occur. The principal advantages of this monitoring method are the robustness and reliability. However, the signal noise due to environment effects or to external vibrations can create some issues. Therefore, to obtain a robust method, a careful design of the monitoring system has to be carried out.

4.3.2 Model-Based Monitoring

When the threshold method is insufficient, a model-based monitor system can be involved in the aircraft. For instance, the servo-valve monitor represented in Figure 4.5 can be made by a model-based system, in order to check the entire actuator control forward path from the SET to the feedback spool position. As it is possible to observe in the Figure 4.5, the servovalve model recieves in input the command of the position loop (CMD), the feedback and the external force. On the basis of these signals, the model computes the predicted spool position by which the monitoring can be carried out. Indeed, this last is compared to the current spool position recorded by a LVDT, which has to be demodulated by using a difference demodulator and a second order low-pass filter that cut-off the highest frequecies (this operation allows to reduce the noises too). The comparison between the current and predicted position can be useful to carry out a health assessment of the servo-valve [20]. So, when a persistent deviation is detected, a fault in the system can be envisaged.

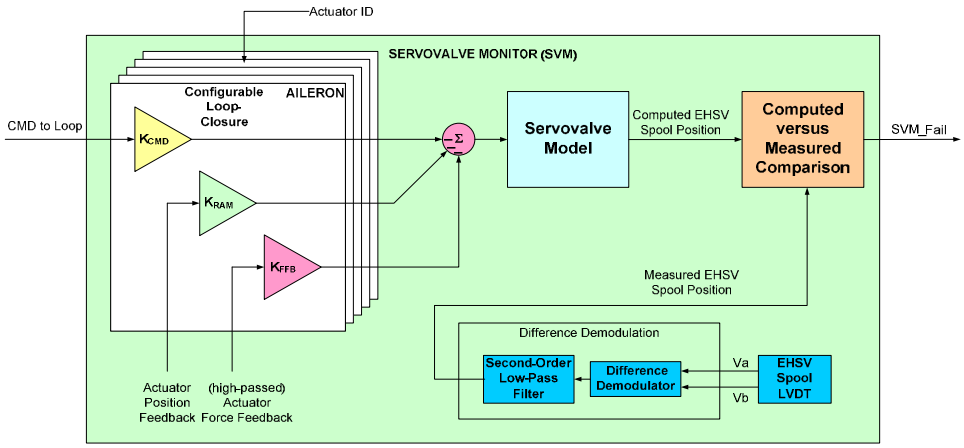

Figure 4.5: Example of model-based monitoring for a servovalve [20]

4.3.3 Frequency Analysis

It is known that when a fault occurs in mechanical components as ball bearings and gear boxes, a vibration analysis using the Fourier transform can be utilized to prevent these failures. About that, in the last years several experiments are conducted in order to use vibration signals as a failure diagnosis system. In [21] a new study to identify possible failures in ball screws by assuming these last as rolling bearings and using the Harris and McCool findings is proposed. Thanks to these studies, it is possible to calculate the so-called defected frequencies that are the Ball Pass Frequency of Shaft (BPFS), Ball Pass Frequency of Nut (BPFN) and Ball Spin Frequency (BSF), reported in equations 4.1, 4.2 and 4.3 [21].

$$BPFS = \frac{1}{120} \cdot z \cdot n \cdot \left(1 + \frac{D_W}{d_m} \cdot \cos\beta\right) \tag{4.1}$$

$$BPFN = \frac{1}{120} \cdot z \cdot n \cdot \left(1 - \frac{D_W}{d_m} \cdot \cos\beta\right) \tag{4.2}$$

$$BSF = \frac{1}{120} \cdot n \cdot \frac{d_m}{D_W} \cdot \left(1 + \frac{D_W}{d_m} \cdot \cos\beta\right) \cdot \left(1 - \frac{D_W}{d_m} \cdot \cos\beta\right) \tag{4.3}$$

Where n is the angular shaft speed, d_m is the ball pitch diameter, D_W is the balls diameter and β is the contact angle.

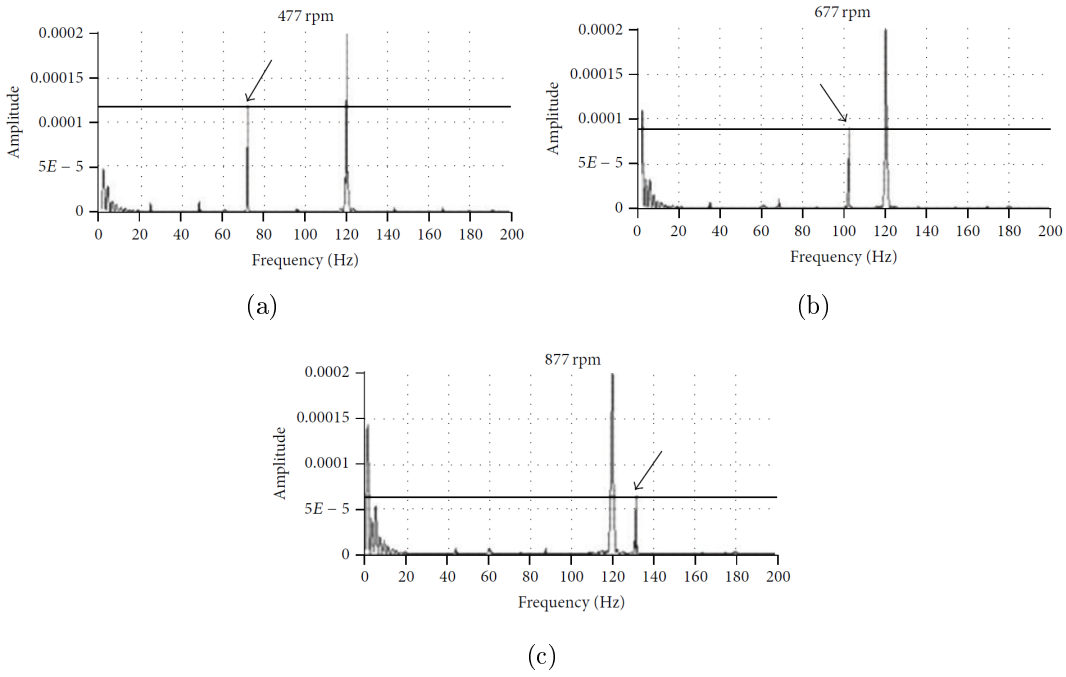

Figure 4.6: Frequency spectrum of faulted ball screw for three angular speeds: 477rpm (a), 677 rpm (b) and 877 rpm (c) [21]

In order to understand how the frequencies can be useful to detect faults in ball screws,

it is possible to observe Figures 4.6(a), 4.6(b) and 4.6(c) that show the vibration signals frequency spectrum of a faulted ball screw for 477 rpm, 677 rpm and 877 rpm respectively. By observing the equation 4.1, it is quite understandable that the faulted frequency varies according to the angular velocity of the screw shaft. Indeed, the defected frequency changes and it becomes higher with the increasing of the angular speed.

All these results are obtained in the steady-state of ball screw, because a frequency analysis does not permit the studying of transient; thus, a discrete Wavelet signal decomposition is necessary if a deeper analysis has to be carried out [21]. In fact, to study EMA real flight conditions with variable solicitations, a time-frequency analysis allows to identify shocks and vibrations that could happen during the flight. It is known as a transient signal has a large frequency content and for this reason it is necessary to describe the signal in the time domain, so that it will be possible to represent the obtained results clearly.

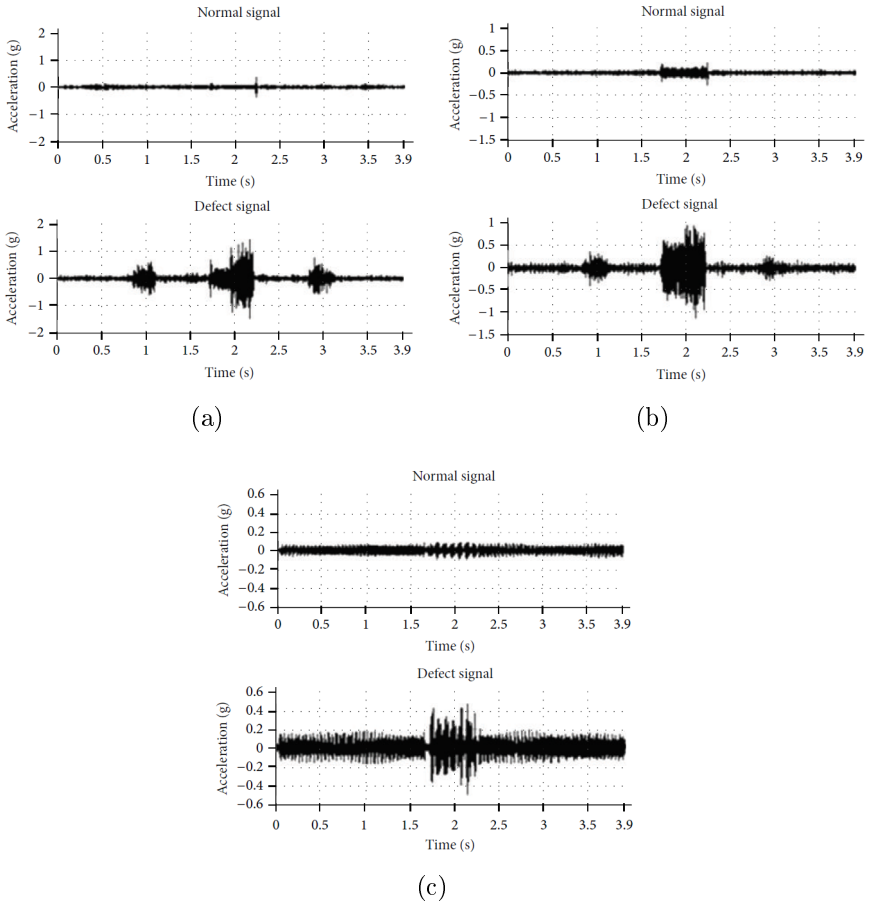

Figure 4.7: Time-frequency analysis for three frequencies intervals: 768Hz-1536Hz (a), 384Hz-768Hz (b) and 48Hz-96Hz (c) [21]

In the light of this assessment, the time-frequency analysis is depicted in Figures 4.7(a), 4.7(b) and 4.7(c) for three frequencies intervals. In this case, the nut makes a linear motion from 0 mm to 267 mm and vice versa with a linear velocity of 133 mm/s and an

angular velocity of the motor of $399\,rpm$. By observing the Figures 4.7(a) and 4.7(b), it is possible to understand that the shaft fault is placed in the center of the screw, because the nut passes through the defected points at $1\,s$ and $3\,s$. Moreover, the Figure 4.7(c) represents the low frequency band, in which is evident the defected signal that persists during the entire time interval (the ball pass frequency spin is around $58.7\,Hz$ when the motor rotates with $399\,rpm$). Therefore, a deep study of vibration permits both to identify possible faults in ball screw and comprehend where they could be placed. However, the vibrations amplitudes depend on the operating condition (as the shaft speed) and the noise can disturb the measuring. For these reasons, a vibration analysis is a robust monitoring method which can be applied in aircraft systems only upon specific environmental conditions.

Despite of these issues, this thesis will analyze the motor current frequency spectrum of a health and faulted ball screw by varying the backlash and friction forces, in order to highlight how the Fourier analysis can be utilized to detect degradation effects.

4.3.4 Data Driven Monitor

The EMA data-driven monitor predicts possible faults in the electromechanical actuators by using collected data from several tests. Indeed, many tests should be performed in order to obtain many data derived from both health and faulted actuators. Moreover, it is necessary that the data are characterized with a high confidence.

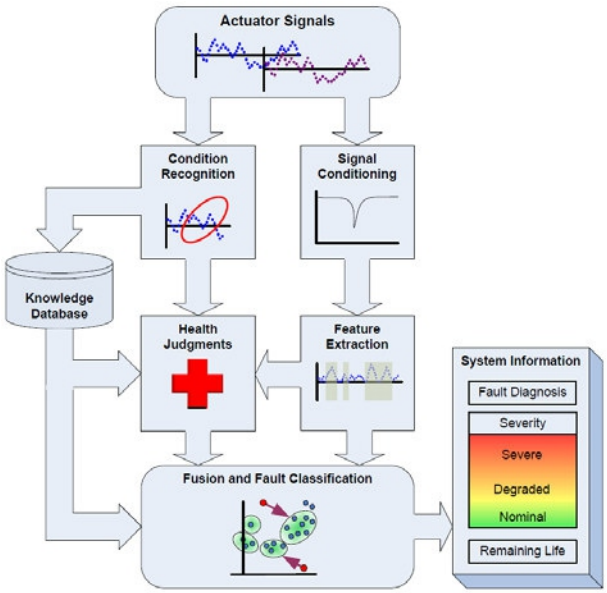

Figure 4.8: Block diagram of an EMA Data-Driven monitor [20]

Therefore, by using the recordered data, an actuator health assessment can be carried out,

simply by comparing the extracted features with the normal feature set: if the deviation between these two quantities is high, the actuator is in the final part of its life. As it is possible to observe in the Figure 4.8, after a conditioning of the actuator signals, a feature extraction of the conditioned signal leads to an actuator health evaluation, taking into account both the knowledge database and the condition recognition of the actuator. Finally, to predict the EMA remaining useful life, it is important to achieve a fusion and fault classification of the available data.

4.3.5 Prognostic and Health Management (PHM)

The Prognostic and Health Management is a monitoring system which predicts the Remaining Useful Life of the actuator. This monitoring method is very powerful but its maturity is not high: for this reason it is in development nowadays. The PHM's structure is based on the well known prognostic algorithms that has been developed in the course of years.

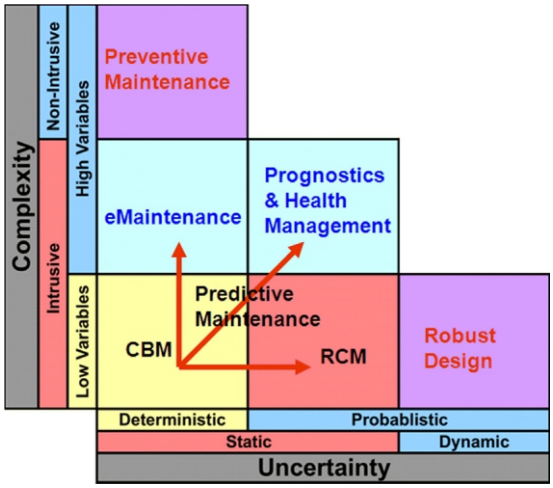

Figure 4.9: Features of the principal prognostics alghoritms [18]

The Figure 4.9 depicts the principal prognostics methods, such as the Condition Based Mantainance (CBM), the eMantainance, etc. The CBM can be utilized only in deterministic and static conditions, where the variables can be useful to extract many features. Indeed, this method is based on the data acquisition and processing from which useful information can be extracted and maintenance decision can be adopted [18].
However, if the system is not deterministic, the data are not simple to obtain because they can vary depending on the performed test. In this case, the most suitable prognostic method is the RCM (Reliability Centered Maintenance), which utilizes several tools such as FMECA to identify the most likely faults, by forecasting the system's remaining life. The RCM is different to the CBM because it is based on the capability of the system

to guarantee a specific reliability in a certain amount of time; therefore, the analysis is probabilistic in this case. However, the RCM method can lead to several issues if the system's complexity is too high. Indeed, in dynamic systems where the behavior varies during time, this method can lead to wrong results because many parameters should be monitored simultaneously. In the light of this assessments, several monitoring algorithms have been developed for high system's complexity [18].
If the system is characterized by low dimensions of many data (as position, velocity, vibrations, etc.), an eMantainence method can be adopted. In this method internet and other communication techniques are used as means to improve the system's performance by annul the downtimes due to maintenance operations. Furthermore, by associating the maintenance works and the process, the eMaintenance permits to reach the optimal solution between production's requests and systems' health [18].
If the system's complexity is very high, the addition of external technologies and sensors can critically affect the precision and performances of the system. In these cases, the Preventive Maintenance represents the most suitable prognostic method. This technique is based on the experience and Mean Time Between Failure (MTBF) by which the maintenance works can be scheduled. However, the Preventive Maintenance is suitable only for static systems, because it is based on the principle that the principal machine's parameters are deterministic and constant [18].
In this perspective, the PHM method is settled in the middle part of the Figure 4.9. The Prognostic and Health Management allows to predict failures before they happen, by making a prevision of the actuator's RUL as well as reducing the downtimes. Thanks to the afore-mentioned features, the PHM represents nowadays one of the most promising prognostics methods. Currently, the PHM can be categorized in three methodologies: model-based, data-driven and hybrid approach [18].
The model based-approach uses a physics-based model of the actuation system to calculate its response. Firstly, it is necessary to modify the principal parameters of the mathematical model to obtain a simulated behavior of the EMA similar to the nominal conditions. After that, there are two types of model which can be adopted. The first one is a static model, which can predict the components' degradation by evaluating the deviations between the current parameters' values of the EMA and the constant healthy results of the model. This approach permits to obtain a monitoring of the overall servosystem but does not allow to isolate and track among competing failures modes. For this reason, a dynamic model is usually preferred. In the dynamic approach, the model parameters are updated continually in order to minimize the deviations between the current behavior of the EMA and its model. This recalibration is realized by identifying different model parameters which will be updated frequently [22].
For instance, the Figure 4.10 illustrates the key concepts about the identification of system

parameters by using a dynamic approach. In particular, it may be possible to observe that the real system output is the sum between the nominal output, fault effects and possible variations.

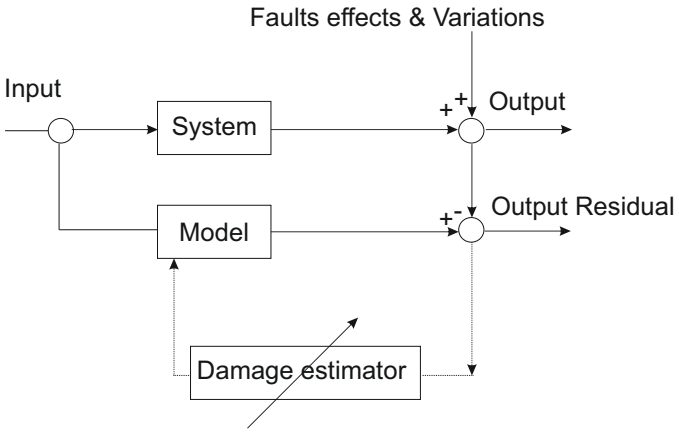

Figure 4.10: Model - Based approach [22]

To identify the fault effects (and therefore identifying the fault) of the EMA, a mathematical optimization can be used. Therefore, this method is based on a minimization algorithm in order to obtain the minimum residual between the predicted and actual response. The equation that explains this algorithm is following reported [22]:

$$E(\bar{a}) = y_i - f(x_i, \bar{a}) \tag{4.4}$$

This iterative equation can lead to the faults' identification but it is necessary to take into account which type of minimization method will be used. For instance, it is possible to use the steepest-decent techniques as well as global search methods such as genetic algorithms or simulated annealing [22].
Once a fault is detected, prognostics are implemented to understand the critical components' RUL. In order to do that, the evolutionary approach is commonly used. This last is based on the measuring of the rate change of the component current state to identify the fault condition by using a N-dimensional parameters space [22].
When a single fault is analyzed, a two-dimensional representation can be utilized, as depicted in Figure 4.11. Here, it is possible to observe that degradation causes a shift of the model's parameters. For this reason, when the time increases, the regions parameters tend to move towards different zones. However, if some faulted regions are known thanks to several tests, it is possible to identify the health EMA's state as well as its future life. In order to do that it is necessary to compute useful indexes by which the diagnostic and prognostic monitoring can be carried out. In particular, by identifying a general parameter β affected by degradation, it is possible to carry out a health assessment of the

actuator by choosing two different strategies [22]:

1. The cumulative index CI, which is defined as:

$$CI_{0,t} = -\frac{\beta_t - \beta_0}{\beta_0} = -\frac{\Delta\beta_{0,t}}{\beta_0} \tag{4.5}$$

   As the equation 4.5 shows, this index represents the non-dimensional variation between the initial state 0 and the final state t

2. The local index EI, defined as:

$$EI_{i,i+1} = -\frac{\beta_{i+1} - \beta_i}{\beta_i} = -\frac{\Delta\beta_{i,i+1}}{\beta_i} \tag{4.6}$$

   Rather than the cumulative index, the local index is defined as the variation of the parameter β between the i and $i+1$ time instants.

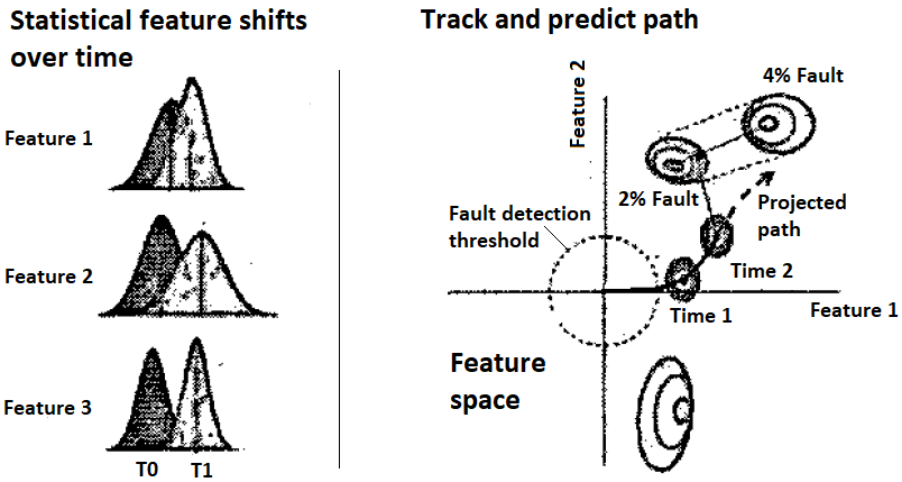

Figure 4.11: Evolutionary approach's scheme [22]

Therefore, these two indexes are used to evaluate the distance between the current condition and the known fault condition; the fault region's condition that have the shortest distance with the current condition represents the most likely fault region to define the current health of the EMA. Furthermore, by using the projected path it is possible to forecast the future health of the EMA.

On the basis of the projected path for each fault, a N-dimensional representation can be obtained. For instance, the Figure 4.12 depicts competitive failures progression using a N-dimensional plot where multiple faults can be observed. In particular, in the figure the RUL obtained by statistical projections is represented. As it is possible to observe, the

failure mode $FM4$ is the most dangerous in the present time, but the failure mode which likely inflicts the EMA's loss is the $FM1$. This example shows the PHM's advantages, because it avoids a wrong evaluation of the RUL basing only on the evaluation of the $FM4$. A correct Prognostic and Health Management allows to focus the monitoring among both failure mode 1 and 4, by reducing the downtime and increasing the aircraft availability. In particular, in the developed model the useful indexes by which a health assessment of the actuator can be carried out are based on the position and the motor current. Indeed, according to [22], in this thesis these indexes will be utilized to highlight the decreased performances of the actuator, in order to identify degradation effects as well as predicting its RUL.

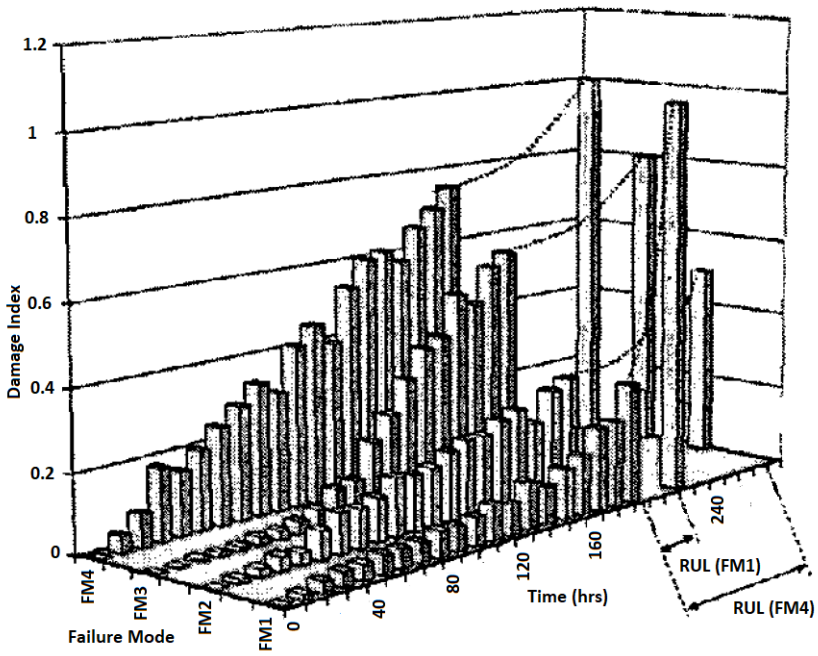

Figure 4.12: Representation of most severity failures in EMA [22]

As before mentioned, if an actuator's detailed model is not available, the data-driven approach (or statistical learning) can be adopted instead of model-based approach. The data-driven prognostic uses available data to give an actuator's health assessment as well as predicting its remaining life. Indeed, the data allow to trend a trajectory that represents how the fault will develop in the course of the time.
Finally, the hybrid approach fuses the advantages of the two mentioned methods to provide more reliable results.

4.4 HUMS sensors to be employed in EMA

On the basis of the reported articles, it is quite clear that a HUMS embedded on a EMA requires several sensors. In particular, the sensors embedded has to facilitate the EMA's health assessment but it is important to use the lowest number of sensors as possible in order to not affect the EMA's reliability. In the light of what it was explained before, usually six types of sensors should be mounted on the EMA [6]:

- Double load sensors based on Wheatstone bridges of strain gauges to measure the actuator load
- Motor current sensor per each phase (higher current is necessary to have the same external force)
- Double temperature sensors to identify possible overheating which could lead to an efficiency decreasing
- Triaxle accelerometers to evaluate the eigenfrequency of the motor and vibrations
- Motor rotational position which permits to calculate the shaft speed (for example using a resolver)
- Actuator linear sensor (the most used is the LVDT)

It is obviously necessary that the implemented sensors cannot affect the EMAs safety as well as leading to an excessive increasing of its costs and complexity. However, the EMAs already include several sensors as encoder and LVDT for recording the angular velocity and linear displacement. The linear sensors do two principal purposes: on one hand they measure the actuator linear position and on the other hand they commutate the motor windings both in case of Brushless DC motor or switched reluctance motor.
Although the sensors' choice seems not difficult in theory, it represents many challenges that it is necessary overcoming. In fact, the choice of sensor's type is critical because it could change the HUMS's performances. Therefore, a good knowledge about the structural system design has to be carried out, in order to obtain the highest efficiency as possible. Moreover, the sensors should be placed as close as possible to the component to reduce the noise and the disturbances in the recorded data [23]. However, in a lot of cases it is not possible to place the sensor near the component. Moreover, for detecting the vibrational features in order to make a vibration monitoring, sensors with high band width and sensitivity are required (a rolling bearing's wear monitoring may require a sampling rate over than $20\,kHz$ [23]).
As the next chapter will explain, the developed Simulink model contains some of the afore mentioned sensors. In particular, it is supposed to have a LVDT, encoder and current

sensor in order to provide the respectives feedbacks to each loop. Furthermore, in order to have a realistic representation of the EMA's behavior, the white noise of the sensors is simulated in the model. Therefore, once the ball screw's structure, wear mechanisms and HUMS concepts were treated, it is now possible to comprehend the model's equations reported in the next chapter.

Chapter 5

Matlab/Simulink Model

In this chapter the EMA model developed in Matlab/Simulink environment will be explained. In particular, the first section provides an overview of the whole electromechanical actuator's model. Successively, the controller design, the stability and performances of each loop will be treated. After that, the other sections explain the subsystems contained in the model: the PWM and inverter, electric motor, reducer and ball screw. Finally, in the last part of this chapter the model behavior will be analyzed, in order to understand how the different parameters can affect the servosystem's response.

5.1 Overview

In the following sections a complete overview of the EMA model is analyzed. In particular, the principal subsystems contained in the model are the Controller, PWM and Inverter, BLDC Motor, Reducer and Ball Screw. As it is possible to observe in Figure 5.1, the EMA model is composed by the afore-mentioned subsystems. In particular, it is possible to observe that the controller recieves in input the SET and feedback position, angular velocity of the motor shaft and current expressed in Volt (due to the sensors that record the sensitive parameter as a voltage). Therefore, the controller subsystem compares the SET position, velocity and current with the respective feedbacks provided by the sensors. Moreover, the model can also simulate the sensors noise with three blocks that are avaiable in Matlab/Simulink environment. The output of the controller is the SET voltage that is sent to the PWM and Inverter subsystem. This last contains the PWM modulation of the SET voltage as well as the inverter. The output of this subsystem is the supply voltage of the BLDC motor, which is a function modulated in amplitude. This last represents the input of the BLDC motor subsystem as well as the angular velocity of the motor shaft, which is the disturbance of the current loop. The outputs of this subsystem are the feedback current (V) and the filtered torque (Nm). The fist one closes the current loop

whereas the second one is forwarded to the reducer model, which performs an increase of the output torque as well as a decrease of the output angular velocity. As depicted in the figure, this subsystem recieves in input the angular velocity of the screw shaft and torque of the motor. The outputs of the reducer model are the torque applied to the screw shaft and the angular velocity of the motor shaft; this last is forwarded to the motor subsystem. The reducer torque as well as the external force are sent to the ball screw subsystem. The outputs of this last are the nut position and the angular velocity of the screw shaft. Obviously, the nut position closes the position loop whereas the angular velocity closes the speed loop. Finally, it is possible to observe that the feedback position and angular velocity are received by the transducers blocks, which are simulated as a second order transfer function.

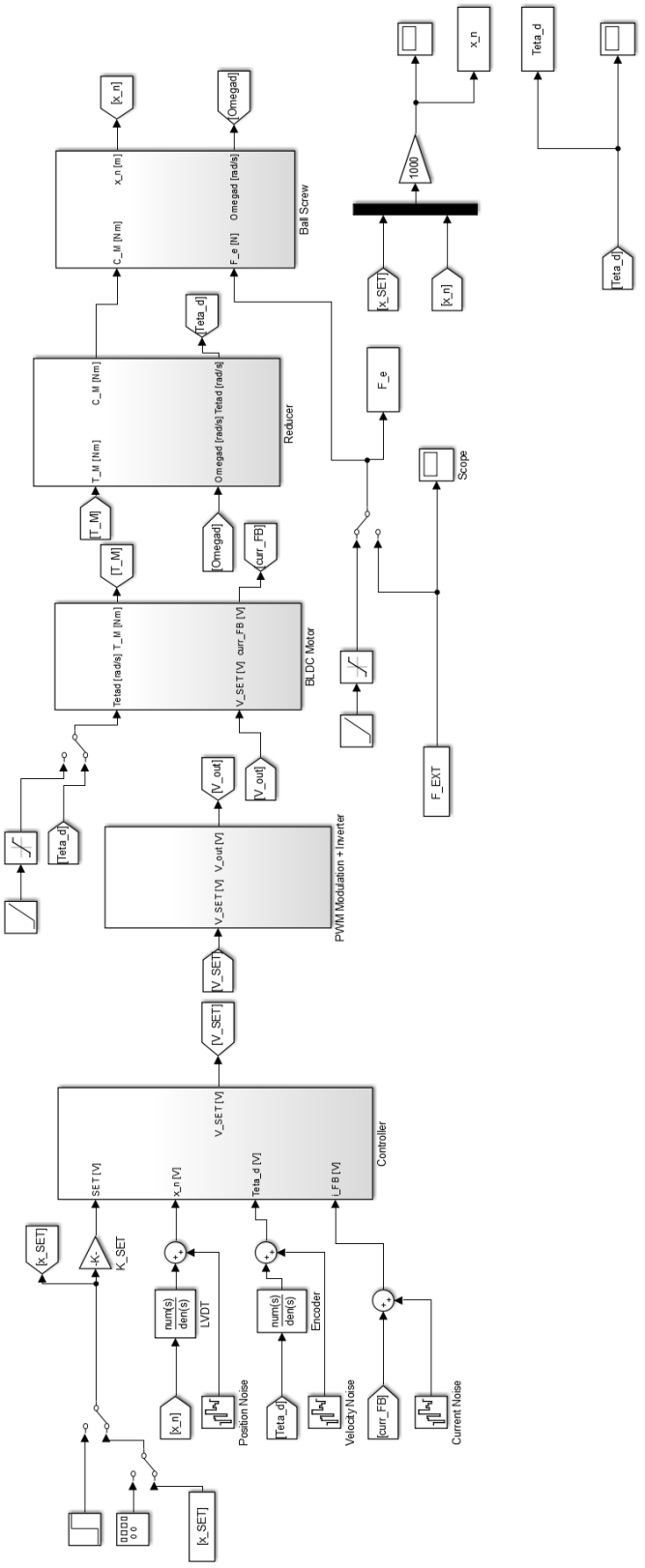

Figure 5.1: EMA Matlab/Simulink Model

5.2 Controller

The controller subsystem contains three controllers which allow to have a feedback of the current, angular velocity of the motor shaft and nut position. In the Figure 5.2 the controller's structure is depicted.

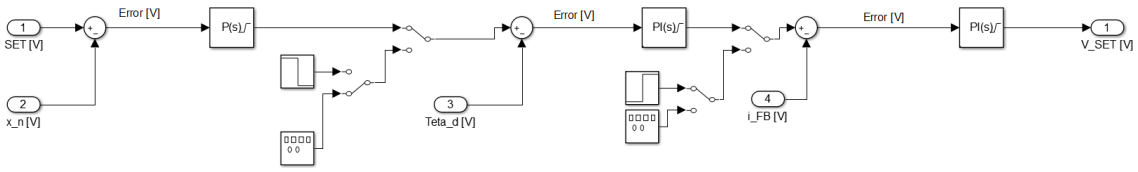

Figure 5.2: Controller subsystem

As the Figure 5.2 shows, the controller subsystem is composed by three controllers. The first one is the position controller, which is only proportional. It receives in input the error between the SET and feedback position expressed in Volt. The output is saturated between the maximum and minimum values of the motor shaft's angular velocity.
Therefore, this signal is forwarded to the second controller, which is proportional and integral. This last receives in input the error between the angular velocity command (expressed in Volt) and the feedback sent from the angular velocity sensor. Therefore, the output of the PI controller is saturated between the maximum and minimum value of the motor current. In this case it is necessary to insert the clamping method in order to avoid the so-called *wind-up* of the integral part of the controller. Indeed, if the output of the controller reaches the saturation value, it cannot increase even if the error is raising. In this case the integral term tends to increase even if the output of the controller does not change. However, this situation causes a malfunction in the PI controller, because the regulator system can work only if the servosystem returns in the linearity zone. In order to avoid the *wind-up* phenomenon, it is necessary to introduce an anti *wind-up* method such as the clamping method, as adopted in this analysis in both PIs controllers.
The output of the velocity PI controller is compared with the feedback current. The difference between these two values constitutes the input of the analogic PI current controller, whose output is limited between the maximum and minimum supply voltage of the motor.
Furthermore, it is possible to observe two manual switches which can be utilized to impose known command to the servosystem in order to check the response of each controller.

5.2.1 Sensors

As depicted in the Figure 5.2, the feedback of position and angular velocity are provided by the LVDT and the encoder whereas the current sensor can be observed in Figure 5.10. In order to have an accurate representation of the sensors behavior, it is supposed to simulate the LVDT and encoder with a second order transfer function [2]:

$$H(s) = \frac{K \cdot \sigma^2}{s^2 + 2 \cdot \zeta \cdot \sigma \cdot s + \sigma^2} \tag{5.1}$$

Where K is the proportional gain, ζ is the damping coefficient whereas σ is the eigenfrequency.
On the contrary, the current sensor is simulated as a first order transfer function [2]:

$$H(s) = \frac{K}{\tau \cdot s + 1} \tag{5.2}$$

Where τ is the time constant. In the Table 5.1 the sensors' parameters as well as the SET proportional gain are reported.

Table 5.1: Sensors Parameters

Symbol	Value	Measure Unit	Definition
K_{SET}	$285,7$	V/m	SET proportional gain
K_p	$285,7$	V/m	Proportional LVDT gain
ζ_{pos}	$0,8$		Damping coefficient of LVDT
σ_{pos}	1256	rad/s	LVDT eigenfrequency
ζ_v	$0,8$		Damping coefficient of encoder
σ_v	3768	rad/s	Encoder eigenfrequency
τ_c	$7,96 \cdot 10^{-5}$	s	Time constant of the current filter

In particular, the LVDT's gain and bandwidth characteristics are obtained from [2] whereas the damping coefficient is settled in order to not have overshoot. Furthermore, the encoder's and current sensor's transfer function simulate only the response delay with a second and first order transfer function with a unitary proportional gain. In particular, the eigenfrequency and damping coefficient of encoder are settled in order to have a sensor bandwidth 10 times higher than the velocity loop's bandwidth and an overdamped system. Finally, the current time constant is settled according to the parameter reported in [2], which is three times higher than the current loop bandwidth.

5.2.2 Controllers design

The controller design represents a fundamental step to evaluate the performances of the servosystem in terms of bandwidth, phase margin or gain margin. As before explained, there are three controllers in the Matlab/Simulink model. The first one is the current loop, the second one is the velocity loop whereas the last one is the position loop controller. In order to design each controller, a proper methodology has to be chosen. Obviously, the analysis starts from the design of the current controller, because it represents the inner loop. The design is conducted in order to obtain a stable servosystem as well as assuring a specific bandwidth for each controller loop. In particular, it is supposed to have a bandwidth of the whole servosystem at least equal to $6\,Hz$. By starting from this value, the other two controller loops are designed in order to have a bandwidth at least 10 times higher than the previous loop: $60\,Hz$ for the velocity controller and $600\,Hz$ for the current controller.

Current Loop

The first analyzed loop is the current loop, as before mentioned. In order to evaluate the correct gains, it is necessary to regulate the open-loop transfer function (to check the stability of the servosystem) and the closed-loop transfer function (to check the bandwidth and performances of the considered loop). It is known that a servosystem is not stable if the out-of-phase of the open-loop transfer function is equal to $-180°$ in correspondence of the point where the amplitude crosses the horizontal axis. In order to avoid instabilities in the servosystem, it is not only necessary that the out-of-phase in the afore-mentioned point is not $-180°$, but at the same time it is important to assure a specific phase margin at least equal to $\phi_H = 60°$ [24]. Moreover, it is important to have an amplitude margin in corrispondence of the point where the out-of-phase is $-180°$ at least equal to $7\,dB - 9\,dB$. This last is called gain margin G_M [24].
Furthermore, the bandwidth represents an important parameter because it is necessary to reduce the cutting in amplitude when the command frequency increases. The design of each controller is carried out by creating a new plant of the servosystem. Indeed, it is made an algorithm by which it is possible to evaluate the non-compensated open loop transfer function. This last is performed by indicating in the model the open loop input and output. Therefore, the created plant is implemented in the tuning tool available in Simulink environment. Here, it is then possible to regulate the controller design in an optimized way. The tuning methodology follows the procedure expressed in [25].
In order to design the current loop, it is supposed to have a stable servosystem as well as a bandwidth at least of $600Hz$. First of all, the Figure 5.3 depicts the open loop transfer function of the current loop.

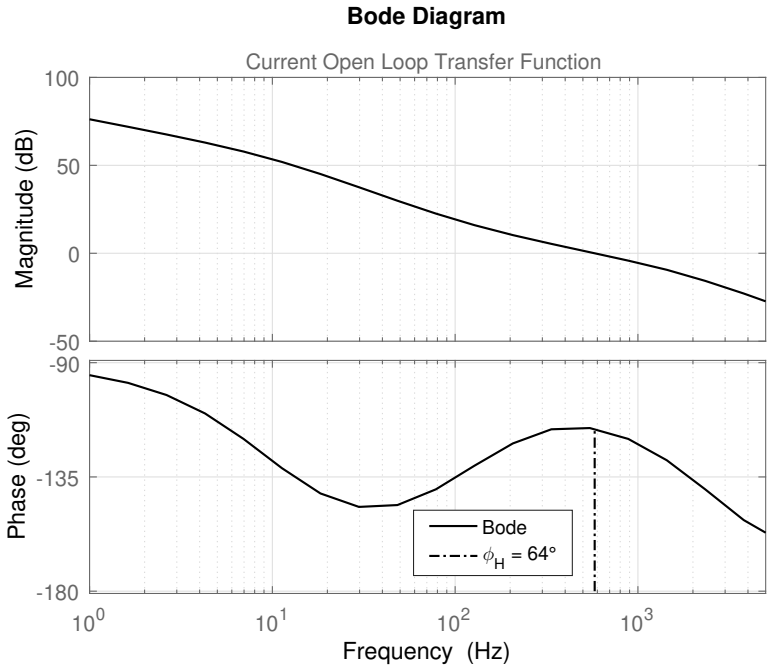

Figure 5.3: Current open loop transfer function

It may be possible to observe that the tuning leads to acceptable results because the phase margin of the current loop is equal to 64° (in this case the gain margin is not depicted because it occurs for very high frequencies. However, it is considerably higher than $7\,dB - 9\,dB$). Furthermore, the phase is equal to $-90°$ for low frequencies because the integral part of the controller introduces a pole in the origin. Moreover, by observing the phase trend, a second pole introduces another out-of-phase of $-90°$. However, the out-of-phase of the integrative part tends to decrease when the frequency is equal to $\frac{K_I}{K_P}$ [24]. For this reason, the out-of-phase tends to decrease in the middle part of the diagram. However, for high frequencies the out-of-phase tends to be equal to $-180°$. Indeed, the first order transfer function of the current transducers introduces another pole in correspondence of $\frac{1}{\tau_c} = 2\,kHz$ [24].
In order to check now the bandwidth of the current loop, the closed-loop transfer function is depicted in the Figure 5.4. This last is computed thanks to the algorithm developed in [26]. As the figure shows, there is a low amplification of the signal in correspondence of the eigenfrequency of the current loop system ($f = 300\,Hz$). Moreover, the bandwidth is settled by $800\,Hz$ because in correspondence of this frequency the cutting in amplitude is equal $-3\,dB$. This value is acceptable because it is higher than the minimum imposed bandwidth. However, in order to avoid malfunctions in the motor, the natural frequency must not be reached, which is far from the operating frequencies anyway. Furthermore, this figure plots the closed loop transfer functions for different command amplitudes. It may be possible to observe that the three trends are superimposed because the current

loop is not affected to the inertia effects. For this reason, the amplitude of the command does not modify the frequency response of the servosystem.

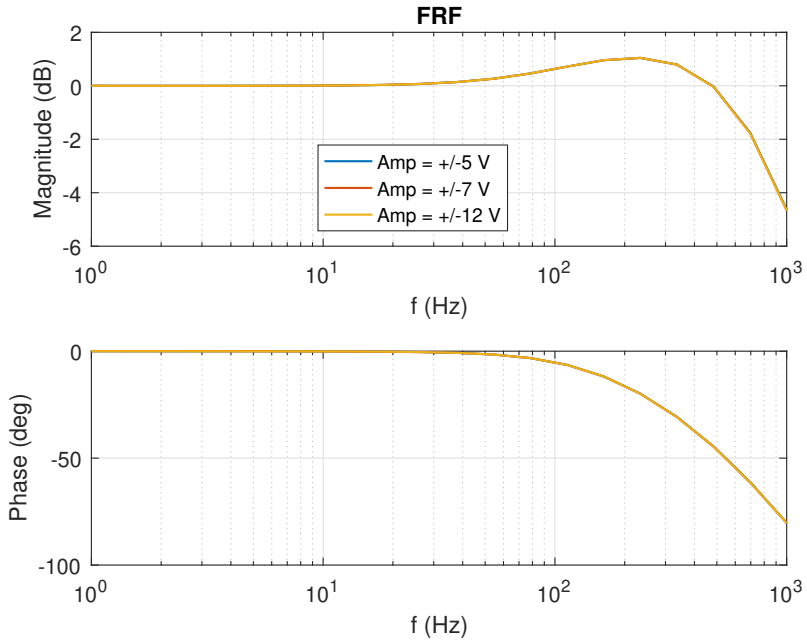

Figure 5.4: Current closed loop transfer function

Velocity loop

The velocity controller design is carried out in the same way of the current loop. In this analysis a stable servosystem with a bandwidth at least equal to $60\,Hz$ is imposed as design constraint. As before mentioned, the open-loop transfer function allows to identify the phase margin of the servosystem whereas the closed-loop shows the performance of the velocity loop.

By observing the Figure 5.5, it may be possible to conclude that the phase margin of the velocity loop is equal to 67° whereas the gain margin is $14\,dB$. Moreover, the closed-loop transfer function allows to evaluate graphically the exactness of the performed design. It is expected that for low frequencies the magnitude is $0\,dB$ in order to have an output equal to the input. This condition can be obtained only if the open-loop transfer function tends to have an infinite gain for low frequencies [24]. Indeed, as the Figure 5.5 shows, the open-loop transfer function has high magnitude when the input frequency decreases. Moreover, for high frequencies it is known that the closed and open loop transfer function have the same behavior [24]. For this reason, it is expected that the cutting in amplitude is very high as the frequencies increase. As a proof of this, the closed loop transfer function is depicted in the Figure 5.6 thanks to the algorithm developed in [26].

Indeed, by observing this figure, it is possible to conclude that the previous considerations

are verified. Furthermore, in this case the performances of the servosystem are affected by the command amplitude. Indeed, the figure shows a lower bandwidth with the increase of the command amplitude. This phenomenon is due to the inertia effects, that lead to lower performances of the servosystem with the increase of the command amplitude. Moreover, in correspondence of $f = 20\,Hz$, there is a low amplification of the signal; indeed, this last represents the eigenfrequency of the velocity loop.

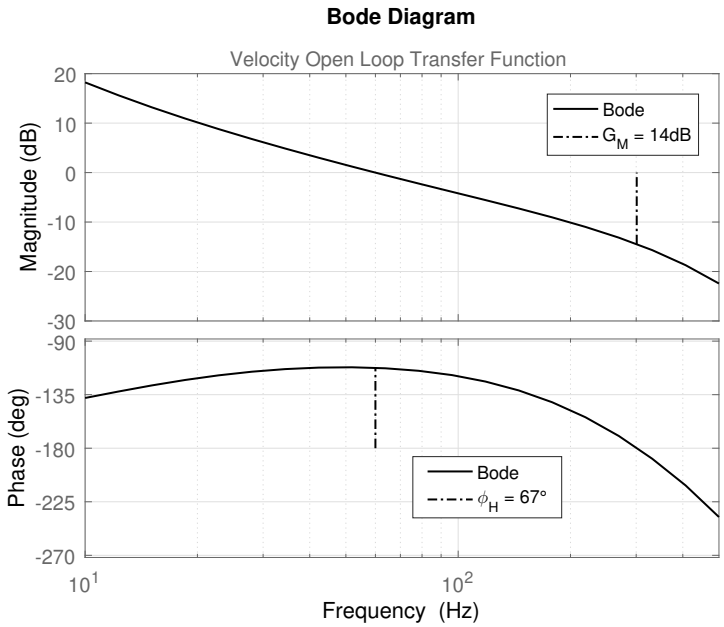

Figure 5.5: Velocity open loop transfer function

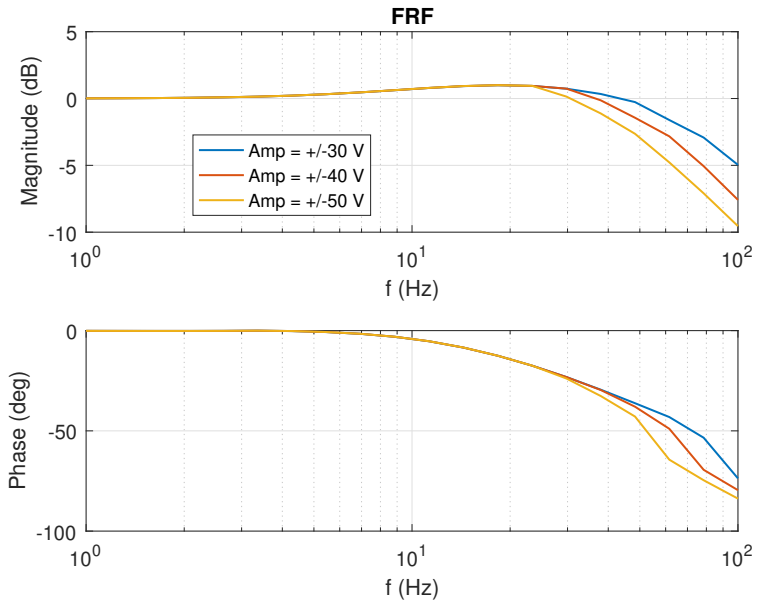

Figure 5.6: Velocity closed loop transfer function

Position Loop

The position loop design is carried out as previously done. As before mentioned, it is necessary to have a stable servosystem with at least $\phi_H = 60°$ and a bandwidth at least equal to $6\,Hz$. However, this last parameter depends on the command amplitude, as it will be possible to observe in the closed-loop transfer function.
By observing the Figure 5.7 it may be possible to conclude that the phase margin of the whole servosystem is equal to 86° whereas the gain margin is equal to $22\,dB$.

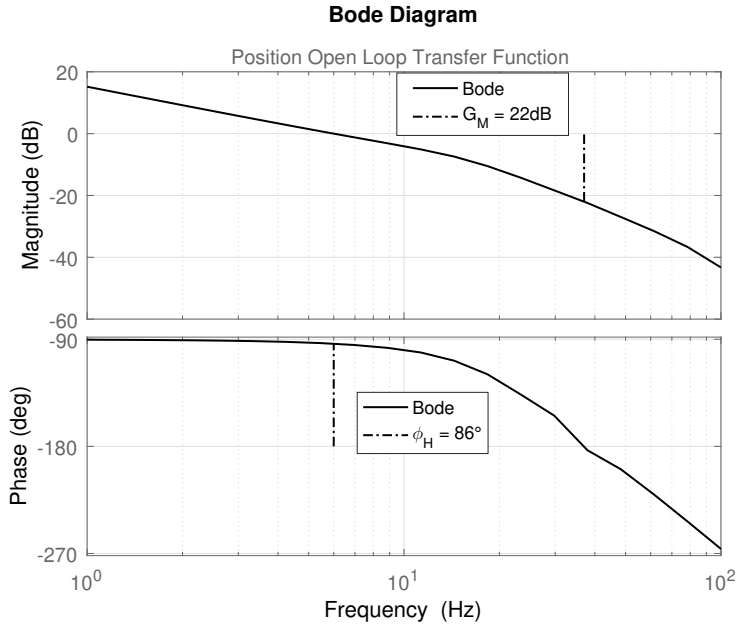

Figure 5.7: Position open loop transfer function

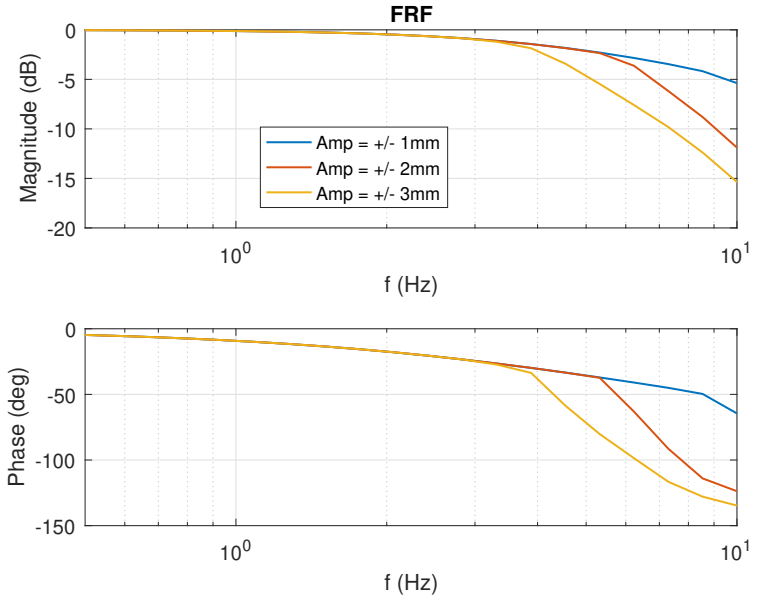

Figure 5.8: Position closed loop transfer function

Moreover, the Figure 5.8 depicts the closed-loop transfer function only in the frequencies of interest [26]. It is known that a servosystem in position control has a bandwidth in the region of few Hertz [24]. Moreover, the bandwidth of the servosystem varies according to the amplitude of the command because also the position loop is affected to the inertia effects. In fact, it is possible to observe that for low frequencies the servosystem has a good behavior with a low cutting in amplitude and out-of-phase. However, the greater the command frequency, the higher the cutting in amplitude. For this reason, it is necessary to specify that only if the command has an amplitude of $1\,mm$ or $2\,mm$ the bandwidth is higher than $6\,Hz$ as imposed during the design. Indeed, when the command has an amplitude of $3\,mm$, the bandwidth of the servosystem is equal to $4\,Hz$.

5.3 PWM and Inverter Model

The controller output is the SET voltage which can vary within a range between $-400\,V$ and $400\,V$. However, the motor supply voltage is fixed to $400\,V$. For this reason, it is necessary to operate a modulation of the SET voltage by means of PWM modulation.

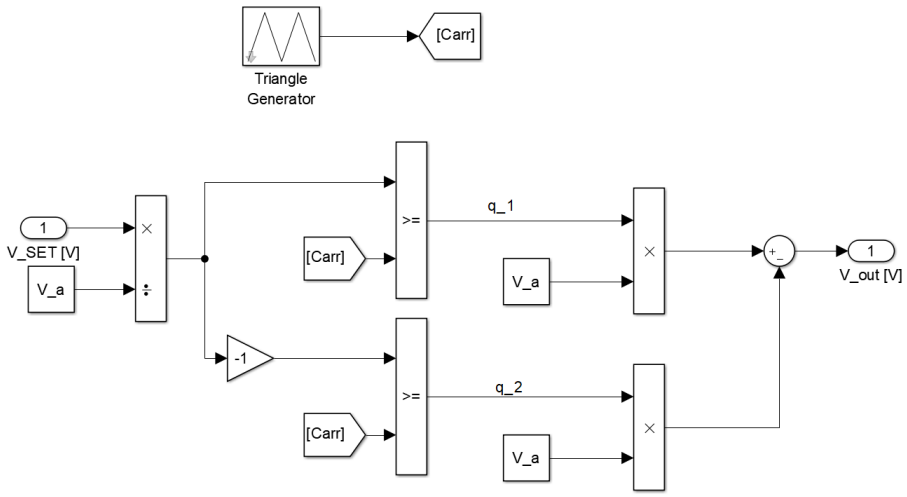

Figure 5.9: PWM Modulation and Inverter model

This last is based on a carrier function that can be a square or a triangular wave with a frequency that can vary from $8\,kHz$ to $14\,kHz$ [2]. In this analysis, the carrier function has a triangular trend with a frequency of $10\,kHz$ and unitary amplitude. Obviously, the higher the carrier frequency, the better the output voltage will reproduce the SET voltage.

As the Figure 5.9 shows, firstly the SET voltage is divided by the supply voltage. Obviously, the output of this division is included between -1 and 1. This number is then compared to the carrier function: the output of this comparison represents the duty cycle,

which is forwarded to the inverter. The duty cycles q_1 and q_2 (the second one works only when the supply voltage is negative whereas the first one only when the supply voltage is positive), multiplied by the supply voltage in the inverter model, allow to obtain the output voltage which is modulated in amplitude.

5.4 Brushless DC Motor Model

The Brushless DC motor is common used in aircraft applications thanks to its high efficiency and few maintenance works that this motor requires. The BLDC motor provides an output torque in the face of an input supply voltage. As it is known, the Brushless DC motor has three phases and the input voltage is subject to PWM modulation. In this thesis the motor is modelled as a single-phase equivalent model, as depicted in Figure 5.10.

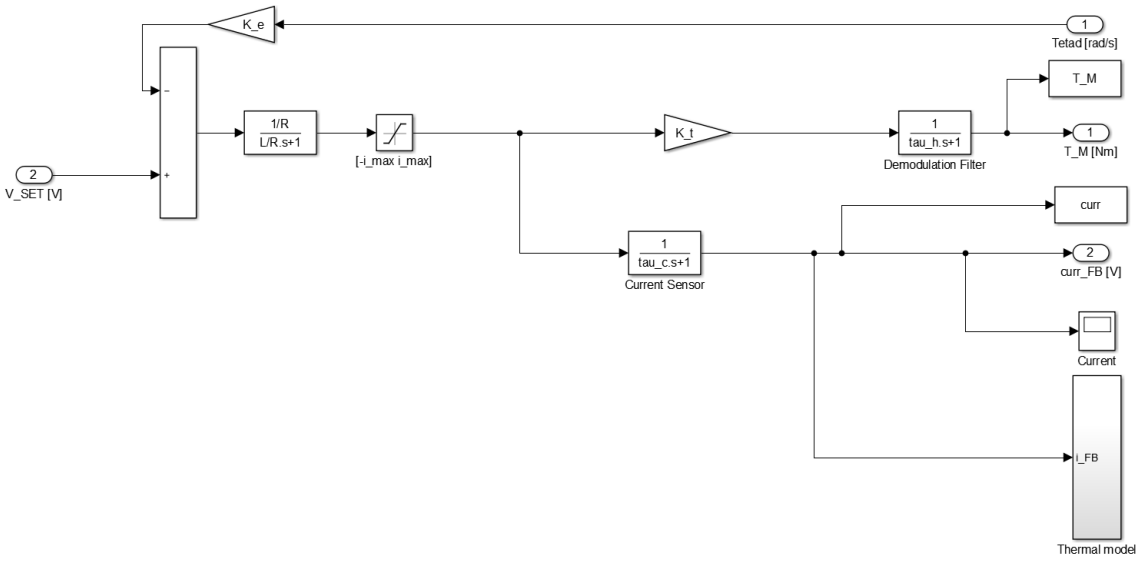

Figure 5.10: BLDC model

The equations of an equivalent single-phase Brushless DC Motor are reported in equations 5.3 and 5.4 [2].

$$V_a = R \cdot i + L \cdot \frac{di}{dt} + k_e \cdot \dot{\theta} \tag{5.3}$$

$$T_M = k_t \cdot i \tag{5.4}$$

Where V_a is the supply voltage [V], R is the resistance of the motor [Ω], L is the motor inductance [H], k_e is the motor electric constant [V/(rad/s)], k_t is torque constant [Nm/A], $\dot{\theta}$ is the velocity of the motor shaft [rad/s] and T_M is the motor torque [Nm].
It may be possible to observe that by using the motor equations, the torque can be computed. Obviously, the output current is saturated between the maximum and minimum

current values. Moreover, the feedback current allows to close the current loop. However, it is possible to observe that the feedback current is processed by the current sensor, which is simulated with a first order transfer function. At the same time, the output torque is also filtered in order to cut off the carrier function thanks to the demodulation filter. As for the current sensor, the demodulation filter is simulated with a first order transfer function [2].

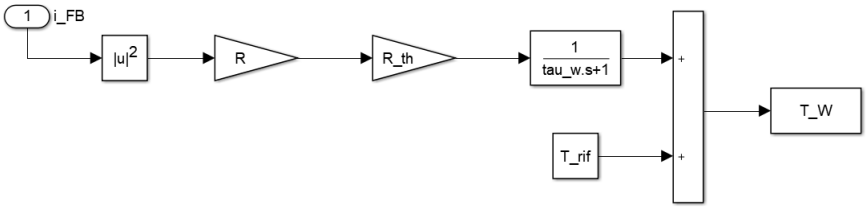

Figure 5.11: Thermal model

Furthermore, the Figure 5.11 shows the simplified thermal model by which is possible to evaluate the windings temperature. The thermal model consists in a first order transfer function [2]:

$$T = T_{rif} + \frac{P_J \cdot R_{th}}{\tau_w \cdot s + 1} \tag{5.5}$$

$$P_J = R \cdot i^2 \tag{5.6}$$

Where T_{rif} is the reference temperature [K], τ_w is the thermal time constant of the motor [s], P_J is the dissipate energy due to Joule effect [W] and R_{th} is the thermal resistance [Ω]. In the Table 5.2 the motor parameters used in the simulations are reported.

Table 5.2: Motor Parameters

Symbol	Value	Measure Unit	Definition
R	0.4	Ω	Motor Resistance
L	6	mH	Motor Inductance
I_m	$4 \cdot 10^{-3}$	$kg \cdot m^2$	Motor inertia moment
k_e	1.15	$V/(rad/s)$	Electric constant
k_t	1.5	$N \cdot m/A$	Torque constant
i_{max}	25	A	Maximum current
V_a	400	V	Supply voltage
R_{th}	2.3	W/K	Thermal resistance
T_{rif}	233	K	Reference temperature
τ_w	13	s	Thermal time constant
τ_h	$1.99 \cdot 10^{-4}$	s	Time constant of demodulation filter

5.5 Reducer Model

The reducer model is ideal because it introduces only a transmission ratio which reduces the output velocity and increases the output torque. By taking into account the reducer efficiency, the equation between the two input ports (screw shaft velocity and motor torque) and two output ports can be expressed as [2]:

$$C_M = \eta \cdot \frac{T_M}{\tau} \tag{5.7}$$

$$\dot{\theta} = \frac{\omega}{\tau} \tag{5.8}$$

Where η is the reducer efficiency, τ is the transmission ratio, C_M is the motor torque and ω is the angular velocity of the motor shaft.

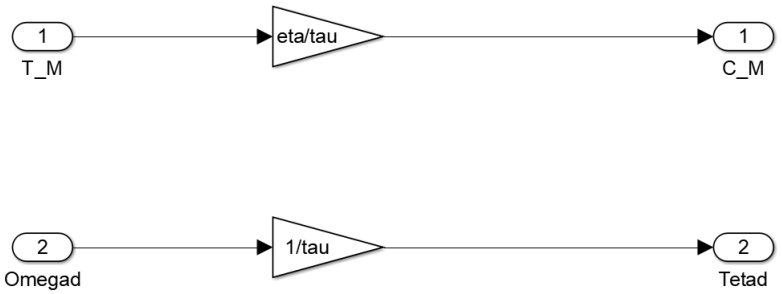

Figure 5.12: Reducer Model

In the Table 5.3 the reducer parameters are reported.

Table 5.3: Reducer Parameters

Symbol	Value	Measure Unit	Definition
η	0.95		Reducer efficiency
τ	0.25		Transmission ratio
I_r	$3 \cdot 10^{-5}$	$kg \cdot m^2$	Reducer inertia moment

5.6 Ball screw model

The model developed in the Simulink environment is a physical based model. Indeed, as it is possible to observe in Figure 5.13, the included subsystems are the principal components of the ball screw: the screw shaft, sphere and double nut. As before mentioned, this model analyzes a ball screw with double nut in order to take into account the preload

force. For this reason, in the following equations the subscript j is reported in order to specify which nut is considered in the analysis.

The screw shaft receives the torque from the reducer. Thanks to the equilibrium equation of the shaft (equation 5.9), it is possible to evaluate the angular velocity and position of the screw shaft. The evaluation of the angular velocity allows to close the velocity loop. Moreover, both angular velocity and position are sent to the sphere subsystem. These last are utilized to evaluate the position and velocity of the screw shaft along the normal direction of the contact point, that is indicated as z_i (where $i = A, B$) in the following equations. In this case, a two degrees of freedom model is adopted, in order to take into account the stiffness and damping forces in the two contact points. The outputs of this subsystem are the contact force between sphere and screw (P'_j) and sphere and nut (P_j). The first one is used to evaluate the reaction torque due to the contact between sphere and screw. Indeed, it is possible to observe that the force $F_{V,j}$ is evaluated in this subsystem and forwarded to the screw shaft subsystem, where the reaction torque C_V will be computed. The force P_j allows to compute the driving force $F_{Z,j}$ that generates the motion of the nut. Indeed, the latter is sent to the nut subsystem. Here, thanks to the equilibrium equation of each nut, it is possible to evaluate its velocity and position. In particular, these two parameters are utilized to evaluate the nuts' displacement and velocity along the z_i axis. However, the real output of the nut subsystem is the position of the whole double nut. This last can be evaluated by considering the equilibrium equation of the whole double nut, as it will be explained in detail in the following paragraphs. Finally, it should be observed that the disturbance of the whole position control servosystem is the external force, that leads to imprecisions in the position trend. In the developed model, several hypotheses were adopted: the screw has a rotary motion whereas the nut realizes a linear motion, in the balls the load is decomposed in a tangential and normal component. The first one generates the spin motion of the spheres while the second one transmits the load from the screw to the nut, the contact angles are constant and equal to $\beta = 45°$, the contact points between the sphere and the screw or the nut are respectively A and B, all the balls have the same load conditions, this makes it possible to analyze only one sphere, the spheres don't have any interaction, each sphere spins only along x_i axis and the stiffness and damping value of the contact point A and B are the same.

In the following paragraphs each subsystem is explicated by following the Matlab/Simulink model developed in [1, 2].

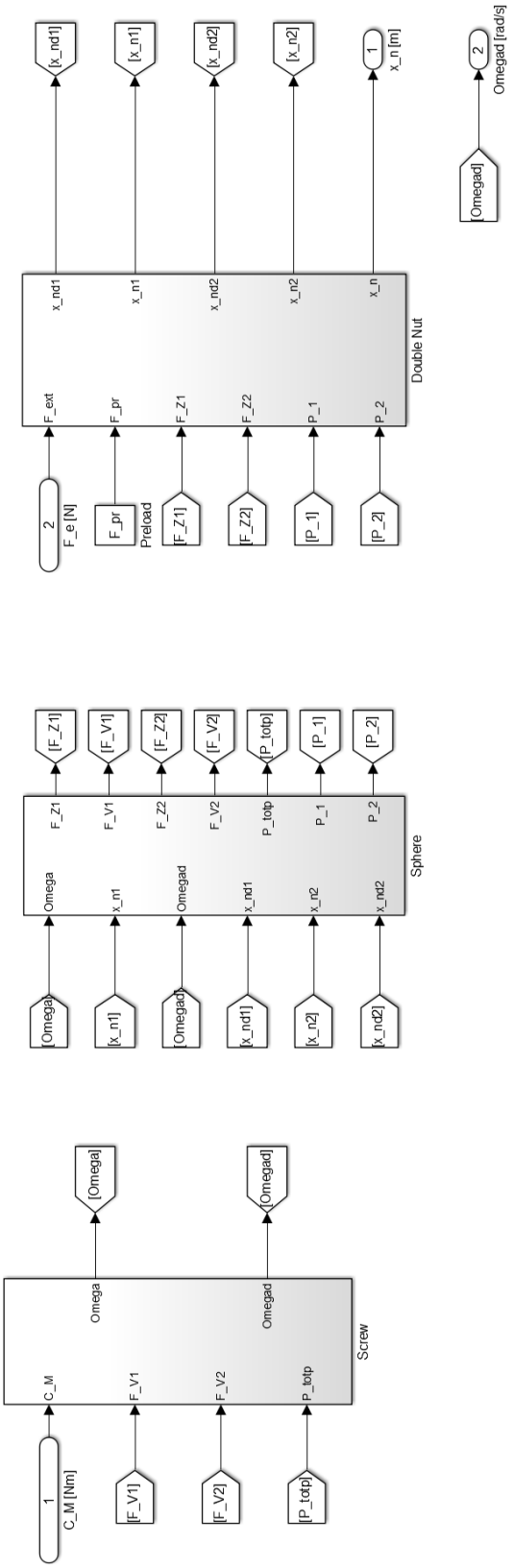

Figure 5.13: Ball screw model

5.6.1 Screw subsystem

In the Figure 5.14 the equilibrium of the screw shaft is depicted. In particular, it is possible to write the following equilibrium equation:

$$C_m - C_V - C_f = I_{eq} \cdot \ddot{\Omega} \tag{5.9}$$

Where $\ddot{\Omega}$ is the screw shaft acceleration, C_m represents the driving torque, C_f is the friction torque, C_V is the resultant moment of all reaction force exchanged between the screw groove and the ball whereas I_{eq} is the overall inertia moment which takes into account the screw, reducer and motor.

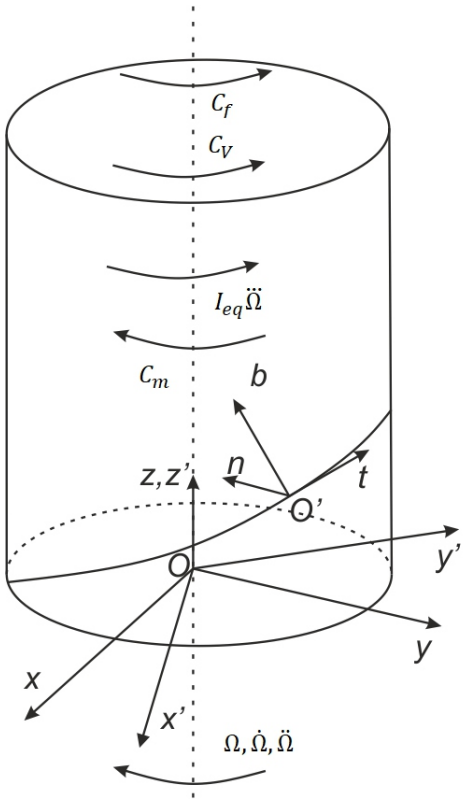

Figure 5.14: Screw shaft equilibrium

The reaction torque C_V can be expressed as [2]:

$$C_V = \sum_j Z \cdot F_{V,j} \cdot [r_m - r_b \cos(\beta)] \tag{5.10}$$

Where $F_{V,j}$ represents the projection along the tangential direction of the normal force between the screw and the ball and it will be calculated in the spheres model. Moreover,

Z is the number of active balls, which can be computed as [1]:

$$Z = 0,6 \cdot Z_{tot} = \left[0,6 \cdot \left(\frac{2\pi \cdot r_m \cdot n_t}{2 \cdot r_b \cdot \cos\alpha}\right)\right] \tag{5.11}$$

Where α represents the helix angle whereas n_t is the number of screw threads that contain the spheres capable to support the load. Furthermore, I_{eq} is the overall screw moment which takes into account the screw (I_s), reducer (I_r) and motor (I_m) reported on the screw shaft, that can be computed as reported in equation 5.12.

$$I_{eq} = \frac{I_m + I_r}{\tau^2} + I_s \tag{5.12}$$

Finally, C_f is the friction torque, which can be modelled by following the Stribeck model [1, 2]:

$$C_f = C_s \cdot \left(1 + 0.1e^{-|\omega_m|}\right) + (c_m + c_{sr}) \cdot \left(\frac{|\omega_m|}{\tau}\right) + Z \cdot \sum_j f_v \cdot \left|P'_j\right| \cdot \cos\alpha \cdot [r_m - r_b \cos(\beta)] \tag{5.13}$$

Where:

- C_s is the static friction torque of supports, reducer and motor. It can be computed as reported in equation 5.14 [2].

$$C_s = \frac{C_{fm} + C_{fr}}{\tau} + C_{fs} \tag{5.14}$$

  In equation 5.14, C_{fs} represents the static friction torque of the supports whereas C_{fm} and C_{fr} are the static torque of the motor and reducer, respectively

- ω_m is the screw shaft speed
- τ is the reducer transmission ratio
- c_m and c_{sr} are the viscous coefficients of the motor and reducer
- f_v is the rolling friction coefficient
- P'_j is the exchanged normal force between ball and screw
- r_m and r_b are the nominal screw and ball radius respectively
- β is the contact angle

Naturally, it is necessary to evaluate the force $F_{V,j}$, which represents the projection of the normal force P'_j (which is along the z_B axis) along the tangential direction of the screw

shaft. In order to do that, the transformation matrixe $\mathbf{T_{3B}^T}$ can be used to calculate the $F_{V,j}$ load (this matrix is reported in section 2.2). Therefore, it is possible ot obtain that [1]:

$$F_{V,j} = P'_j \cdot \sin\alpha \cdot \sin\beta \tag{5.15}$$

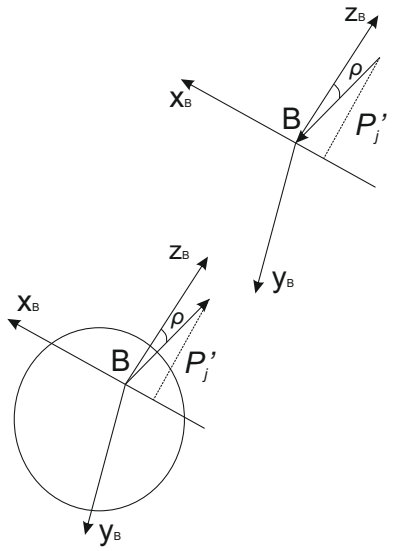

Figure 5.15: Magnification of the ball-screw contact [2]

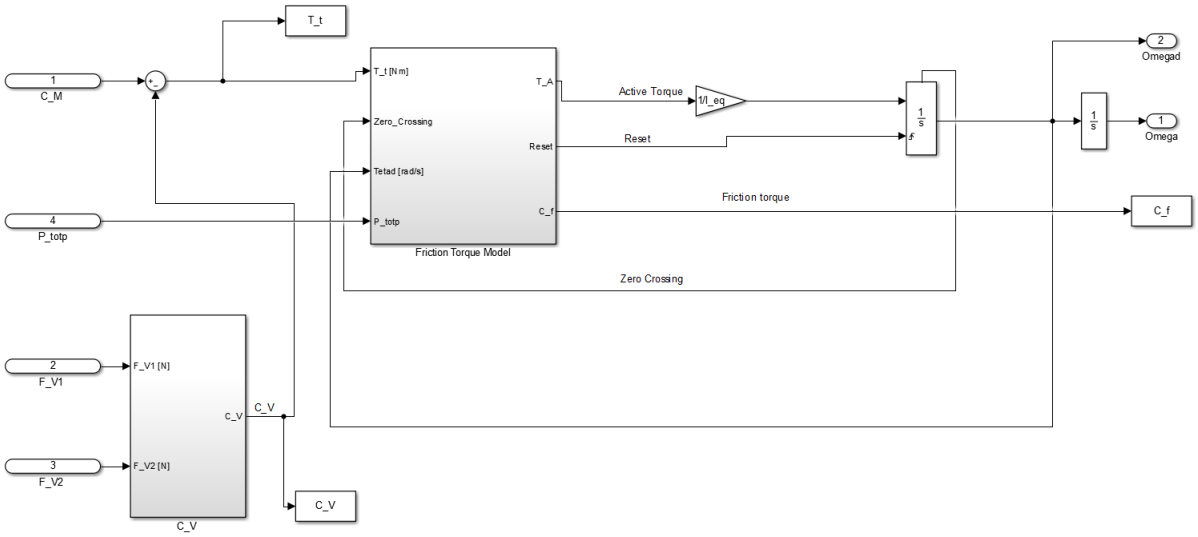

Figure 5.16: Screw subsystem

As it is possible to observe in the Figure 5.15, the normal force P'_j is the load along the z_B axis of the total force exchanged between the screw and the ball. It may be possible to observe that the P'_j force is negative when it is considered on the screw shaft; however, the direction of this force creates a reaction torque with the same sign of the Figure 5.14.

Furthermore, by dividing the force P'_j for $\cos(\rho)$ (where ρ represents the friction angle), the total force exchanged between the screw and the ball can be evaluated. In the Figure 5.16 the whole screw subsystem is depicted.

Regard to the friction model, it has been modelled in order to include the static friction in the case of the active torque is lower than static friction torque [2]. This last can be observed in Figure 5.17. This figure shows four inputs ports: the total torque subtracted by the reaction torque (T_t), the zero crossing signal derived from the state port of the acceleration integrator, the angular velocity of the screw shaft and the sum of the contact forces between the balls and screw. In particular, the zero crossing provides an unitary signal when the velocity becomes $0\,rad/s$, a null output in other cases. Furthermore, as the Figure 5.17 shows, the friction torque is evaluated on the basis of the outputs of two switches.

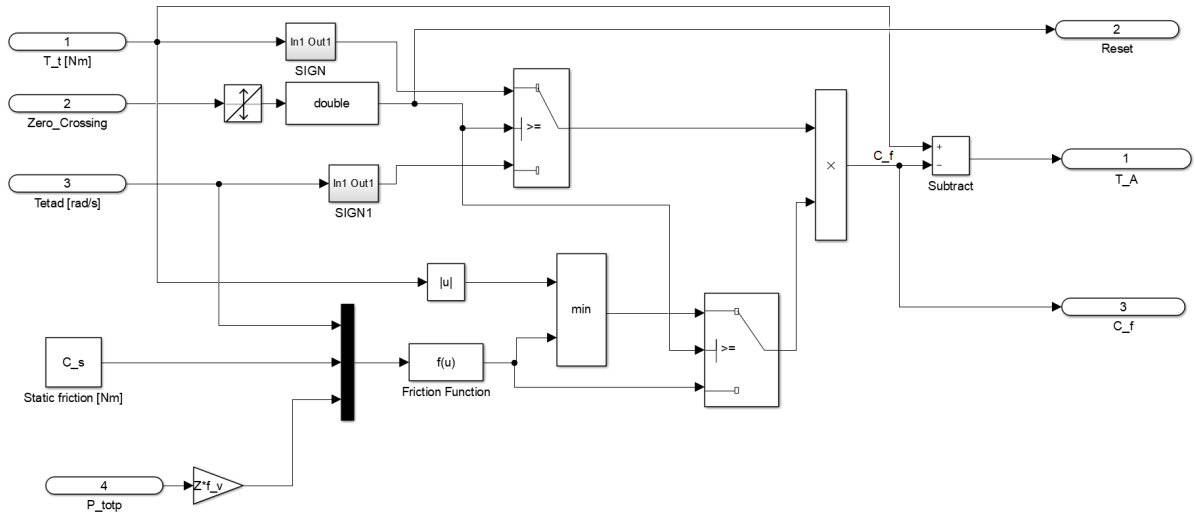

Figure 5.17: Friction Model

In order to understand how the friction model works, it can imagine to apply a torque that increases from $0\,Nm$ to a final value higher than the static friction. At the beginning, the external torque is lower than the static friction torque. In this condition the zero crossing signal derived from the first integrator provides an unitary value. Therefore, all the switches activate the upper outputs. In particular, it is possible to observe that the second switch (placed in the bottom part of Figure 5.17) provides as output the minimum between the friction torque (derived from the friction function $f(u)$) and the driving torque: in this case the output will be the driving torque itself. Therefore, the output of the switch 2 is multiplied by the output of the switch 1, which is the sign of the driving torque in this case. Then, the friction torque is equal to the driving torque if this last does not overcome the static friction: there is not screw motion.

On the contrary, when the driving torque exceeds the friction torque, the latter will be

equal to the static friction value. However, when the nut motion starts, the zero crossing signal changes its value, by passing from 1 to 0: the switches will activate the other outputs. It is possible to observe that in this situation the output of the second switch is the friction torque derived from the function $f(u)$; this last is multiplied by the sign of the angular velocity. Moreover, whenever the velocity becomes null the transition from dynamic to static condition occurs, because the zero crossing changes its value.

5.6.2 Sphere subsystem

It is possible to observe in Figure 5.18 that the sphere's motion is along z_i axis (where i can be A or B), in other words along the direction which passes through both O' and the contact points. Obviously, since the contact angle is considered equal to 45°, then the z_B direction is coincident with z_A (in fact, the contact point is not reported in the displacement of screw, ball and nut in Figure 5.18). In this analysis, the backlash, the damping and stiffness forces of the two contact points A and B are considered [1].

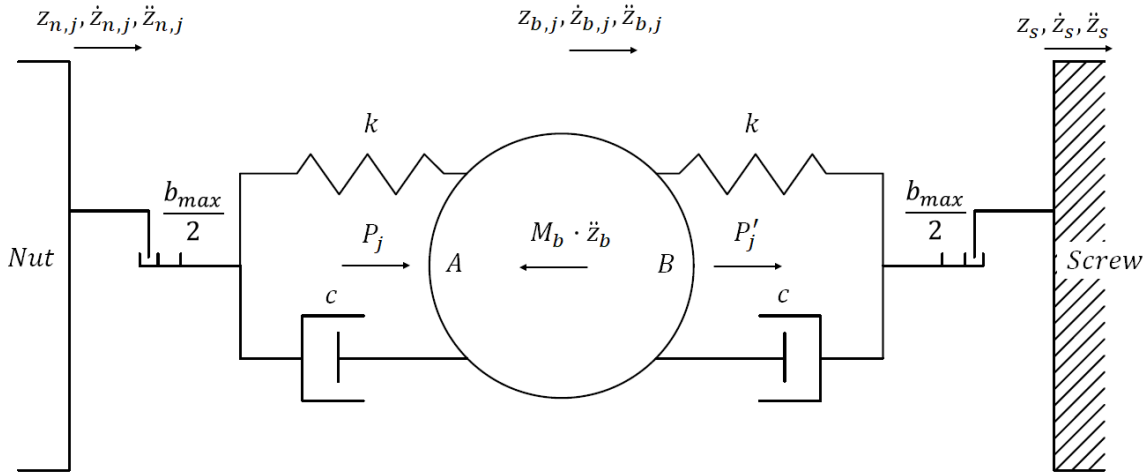

Figure 5.18: Sphere subsystem

By identifying as P_j and P'_j the normal force in the two contact points between ball and nut and ball and screw respectively, it is possible to obtain the following equilibrium equation [1]:

$$M_b \cdot \ddot{z}_b - P'_j - P_j = 0 \tag{5.16}$$

The outputs of the sphere's subsystem are the P'_j and P_j forces, by which will be possible to evaluate the C_V torque in the screw subsystem and the driving force $F_{Z,j}$, which is forwarded to the nut subsystem. The normal forces of contact points can be computed as [1]:

$$P'_j = -\left\{k \cdot \Delta z_{bs,j} + f\left[c \cdot \left(\dot{z_{b,j}} - \dot{z_s}\right), k \cdot \Delta z_{bs,j}\right]\right\} \tag{5.17}$$

$$P_j = \{k \cdot \Delta z_{nb,j} + f\left[c \cdot (\dot{z_{n,j}} - \dot{z_{b,j}}), k \cdot \Delta z_{nb,j}\right]\} \tag{5.18}$$

Where:

$$\Delta z_{bs,j} = z_{b,j} - z_s - \frac{b_{max}}{4} \cdot sign\left(z_{b,j} - z_s\right) \tag{5.19}$$

$$\Delta z_{nb,j} = z_{n,j} - z_{b,j} - \frac{b_{max}}{4} \cdot sign\left(z_{n,j} - z_{b,j}\right) \tag{5.20}$$

In the equations 5.17, 5.18, 5.19 and 5.20, z_s, $z_{b,j}$, $z_{n,j}$ are the screw, ball and nut position along the z axis, respectively. Moreover, c represents the damping coefficient, b_{max} is the backlash value whereras k is the stiffness of the spring. This last is modelled in order to guarantee the axial stiffness obtained in the catalogues. Moreover, it is known that the ball screw stiffness increases according to the applied preload. In order to take into account this phenomenon, it is supposed to have a linear correlation between the spring stiffness and the preload force, as reported in equation 5.21.

$$k = k^* + m \cdot F_{pr} \tag{5.21}$$

Where k^* is the ball screw stiffness without the preload, F_{pr} represents the preload force whereas m is the slope of the linear correlation. In order to evaluate the slope of the linear trend, it is necessary to impose a value of k^* and a second point where the linear trend will cross. In particular, the first value is settled in order to obtain an acceptable stiffness of the ball screw, that in this analysis it is supposed to be $100\,N/\mu m$. Once this value is regulated, the slope of the linear trend has to be determined. In order to do that, the correlation between the axial deformation and the external load for a no preloaded and a preloaded ball screw is used [27]. In particular, the slope is regulated in order to have a deformation of the preloaded ball screw equal to half of the no preloaded ball screw, if the external load is three times the preload. The analysis is conducted by comparing the displacement of a preloaded ball screw with $F_{pr} = 3\,kN$ and a no preloaded ball screw when an external load of $F_{ext} = 9\,kN$ is applied with a ramp trend. After this methodology the slope resulted equal to $820.5\,m^{-1}$.
Finally, f is a function that guarantees the continuity of the exchanged force. In fact, it is the minimum function when $c \cdot \Delta\dot{z} + k \cdot \Delta z > 0$, the maximum function in the other cases. This backlash model follows the model explained in [28]. This mathematical solution permits to avoid discontinuities in the exchanged force but at the cost of a limitation of the damping force:

$$|c \cdot \Delta\dot{z}| \leq |k \cdot \Delta z| \tag{5.22}$$

Moreover, the contact force will be null if there is no contact due to the backlash. This consideration can be mathematically expressed as:

$$|\Delta z_{bs,j}| \leq \frac{b_{max}}{4} \Longrightarrow P'_j = 0\,N \tag{5.23}$$

$$|\Delta z_{nb,j}| \leq \frac{b_{max}}{4} \Longrightarrow P_j = 0\,N \tag{5.24}$$

As it is possible to observe in the equations 5.23 and 5.24, the backlash model permits to obtain a symmetric dead zone whose amplitude is $b_{max}/2$ per each contact point. Moreover, when the springs are compressed, half dead band is subtracted to the relative position between ball and screw or ball and nut. On the contrary, when the springs are in traction, half dead band is summed to the relative position (that in this case is negative).

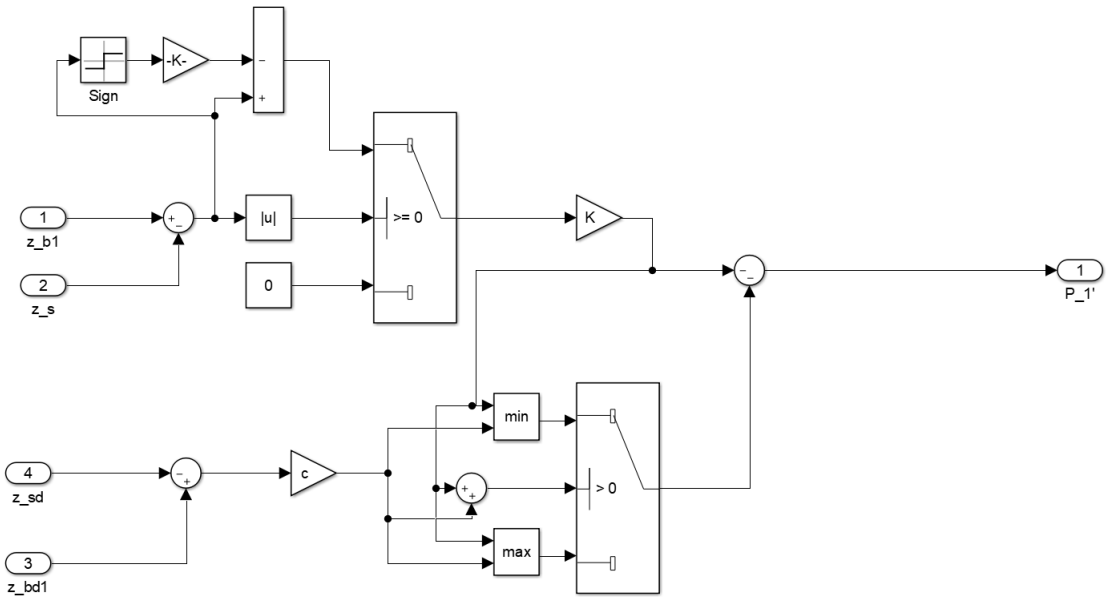

Figure 5.19: Calculation of the contact force

The Figure 5.19 depicts the utilized blocks that allow to evaluate the contact force in the first nut in the B point. The switch in the upper part of the figure checks if the relative displacement is higher than the backlash value. If this situation does not happen, the output of this switch is null. Moreover, the second switch provides as output the minimum or the maximum between the stiffness and damping force if their sum is major or minor than zero respectively. If the relative position is lower than backlash, it is possible to observe that the output of the second switch is zero too. For this reason, the final sum of Figure 5.19 provides a null output when the relative position is lower than the backlash value. In the other situations, the contact force model evaluates the contact

forces according to equations equations 5.17 and 5.18.

Now, it is necessary to evaluate the screw and nut displacement along the z axis. In order to do that, it is possible to refer to Figure 5.14, that represents the utilized references systems. Indeed, it is possible to evaluate the axial displacement of the screw shaft expressed in the $Oxyz$ reference system by imagining to linearize its rotary motion:

$$\mathbf{x_s^{Oxyz}} = \begin{Bmatrix} 0 \\ 0 \\ \frac{p}{2\pi} \cdot \Omega \end{Bmatrix} \tag{5.25}$$

By multyplying this vector by $\mathbf{T_2^T} \cdot \mathbf{T_{3B}}$ (that are reported in the section 2.2) it is possible to obtain the displacement along the z axis [1]:

$$z_s = \frac{p}{2\pi} \cdot \Omega \cdot \cos\alpha \cdot \sin\beta \tag{5.26}$$

For the same considerations, it is possible to evaluate the nut displacement along the z axis by knowing the nut axial displacement $x_{n,j}$ [1]:

$$z_{n,j} = x_{n,j} \cdot \cos\alpha \cdot \sin\beta \tag{5.27}$$

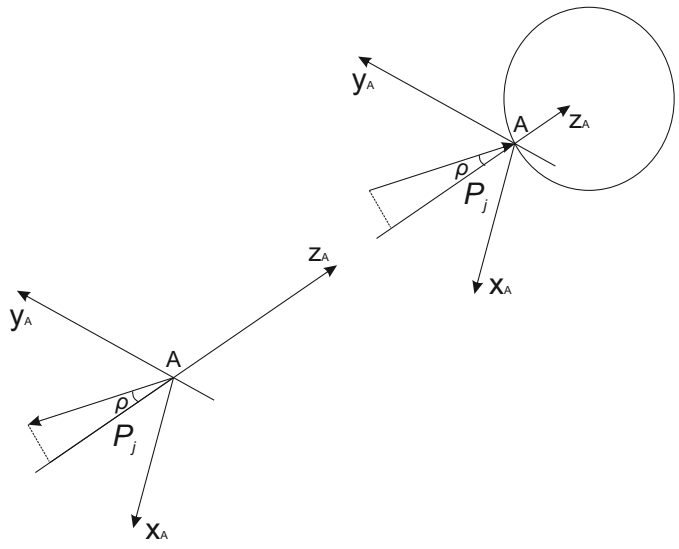

Figure 5.20: Magnification of the ball-nut contact point

Finally, it is possible to calculate the driving force $F_{Z,j}$ which creates the nut motion [2]:

$$F_{Z,j} = -P_j \cdot \cos\alpha \cdot \sin\beta \tag{5.28}$$

Obviously, the minus sign in the equation 5.28 is due to the direction of the $F_{Z,j}$ force. In particular, this last has the opposite sign compared to the P_j force. Indeed, as it is possible to observe in the magnification of the A contact point reported in Figure 5.20, the P_j force exchanged with the nut is directed along the negative direction of z_A axis. For this reason, it is necessary to introduce a minus sign in order to compute the $F_{Z,j}$ force according to the direction of equation 5.29 and 5.30.

5.6.3 Nut subsystem

The Figure 5.21 represents the equilibrium equation of the double nut. In particular, it is possible to observe several parameters: x_n is the double nut displacement, $F_{Z,j}$ is the driving force along the screw axis, M_n is the double nut mass, $F_{fr,j}$ is the friction force, F_{ext} is the external force applied to the nut and F_{pr} is the preload force due to the thickness applied between the two nuts.

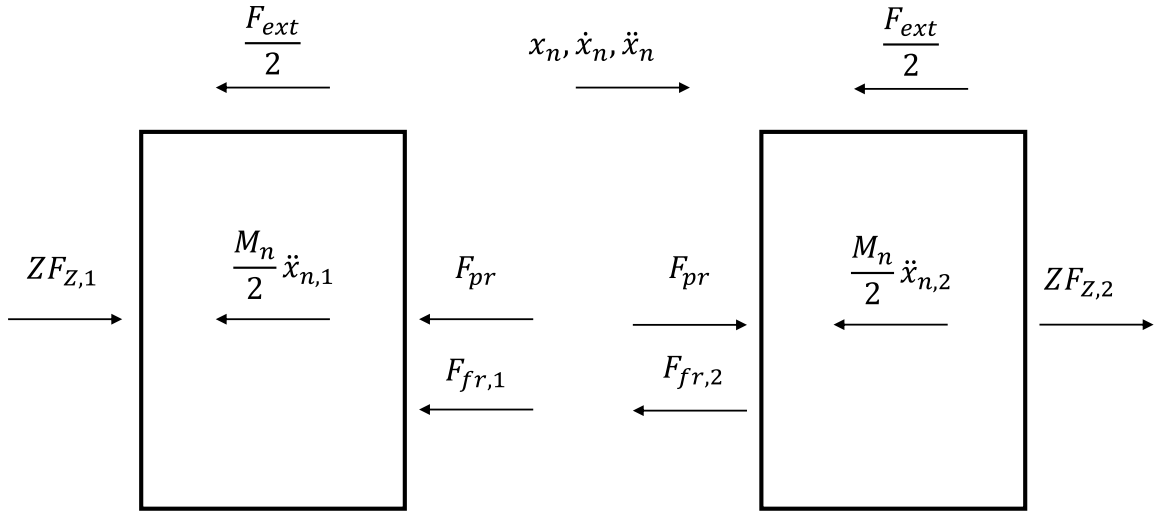

Figure 5.21: Double Nut equilibrium

For one of the two nuts the equilibrium equation can be expressed as equation 5.29 [1].

$$\frac{M_n}{2} \cdot \ddot{x}_{n,j} \pm F_{pr} - Z \cdot F_{Z,j} + \frac{F_{ext}}{2} + F_{fr,j} = 0 \tag{5.29}$$

Where the preload force sign is positive when $j = 1$, it is negative in the other case. Then, by considering the entire system including the two nuts, it is possible to obtain the nut

position by integrating two times the double nut acceleration:

$$M_n \cdot \ddot{x}_n = Z \cdot (F_{Z,1} + F_{Z,2}) - F_{ext} - F_{fr,1} - F_{fr,2} \tag{5.30}$$

The friction force between the ball and the nut is evaluated as follow [1, 2]:

$$F_{fr,j} = \frac{F_s}{2} + c_N \cdot \frac{2\pi}{p} \cdot |\dot{x}_{n,j}| + f_v \cdot Z \cdot |P_j| \tag{5.31}$$

Where c_N is the viscous friction coefficient of the nut reported on the screw axis (for this reason it is multiplied by $\frac{2\pi}{p}$), that can be evaluated as:

$$c_N = \frac{c_{sm} + c_{sr}}{\tau} \tag{5.32}$$

Moreover, p is the screw pitch, f_v is the rolling friction coefficient and Z is the number of active balls. The sliding friction model was developed in the same way of the friction torque model explained in the screw subsystem. The Figure 5.22 represents the Simulink model of the double nut.

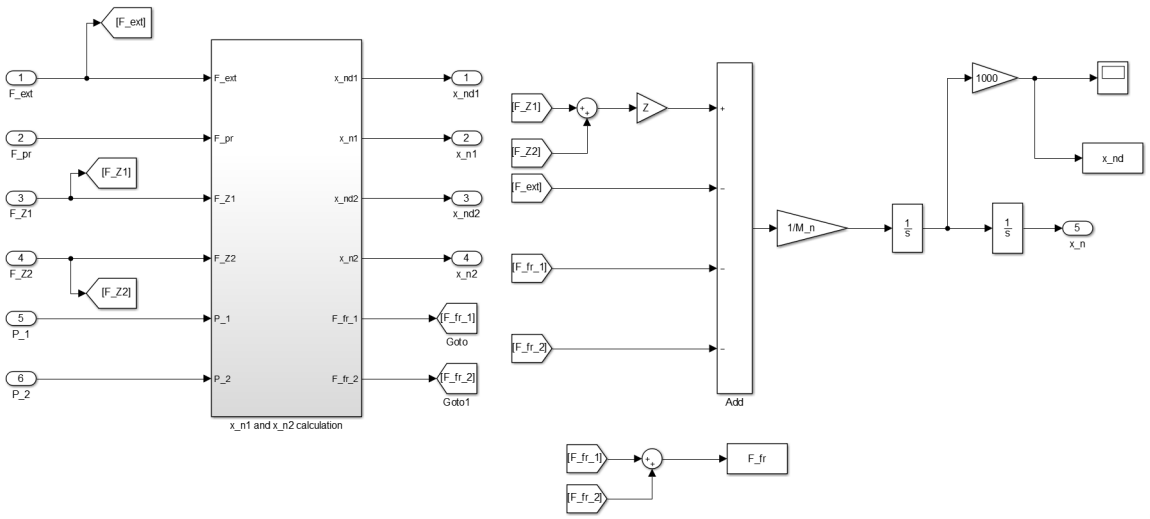

Figure 5.22: Double Nut Model

Therefore, the evaluation of the double nut position allows to close the position loop. Finally, in the Table 5.4 the ball screw parameters are depicted. In particular, the rolling friction is settled according to the value reported in literature [9] whereas the other friction parameters derived from [2].

Table 5.4: Ball screw Parameters

Symbol	Value	Measure Unit	Definition
i	6		Circuits number
Z	21		Balls number per each circuit
I_s	$8 \cdot 10^{-5}$	$kg \cdot m^2$	Screw inertia moment
p	5	mm	Screw pitch
r_b	2	mm	Ball radius
r_m	15	mm	Screw nominal radius
α	3.04	deg	Helix angle
M_n	0.54	kg	Nut mass
M_b	$2.7 \cdot 10^{-4}$	kg	Ball mass
f_v	0.001		Rolling friction coefficient
C_{fm}	0.013	$N \cdot m$	Static friction torque of the motor
C_{fr}	0.0173	$N \cdot m$	Static friction torque of the reducer
C_{fs}	0.055	$N \cdot m$	Static friction torque of the supports
c_{sm}	$5.8 \cdot 10^{-8}$	$N \cdot m$	Viscous friction coefficient of the motor
c_{sr}	$2.2 \cdot 10^{-8}$	$N \cdot m$	Viscous friction coefficient of the reducer

5.7 Model behavior

In this section, the model behavior will be analyzed by varying the principal parameters as the position command, external force, preload, friction and backlash. In particular, the first subsection analyzes the time interval that the ball screw employs to cover its total stroke by sending a step command to the servosystem. The second subsection deals with the model response when an external load is applied whereas the third section shows the effect of the preload force. Finally, the last subsection explains the effect of the degradation in the EMA's accuracy and current. In particular, this last will represent the basis of the Health and Usage Monitoring System method explained in the next chapter.

5.7.1 Step response - No external load

In this subsection the time interval that the nut employs to cover its total stroke is analyzed. For this reason, it is supposed to not apply an external load, preload as well as backlash.

In the Figure 5.23 the position trend is depicted, by forwarding a step command to the servosystem at $0.01\,s$. As the figure shows, the nut manages to reach the SET position with a delay due to inertias of the mechanical components and saturation values of current and motor angular velocity; in fact, the nut reaches the end of its stroke after $0.9\,s$. It is possible to observe the first acceleration phase, followed by a steady phase in which the

nut velocity is constant. Indeed, in this phase the saturation value of the angular velocity is reached and therefore also the nut velocity is constant. Finally, in the last phase there is a deceleration by which the final nut position is reached.

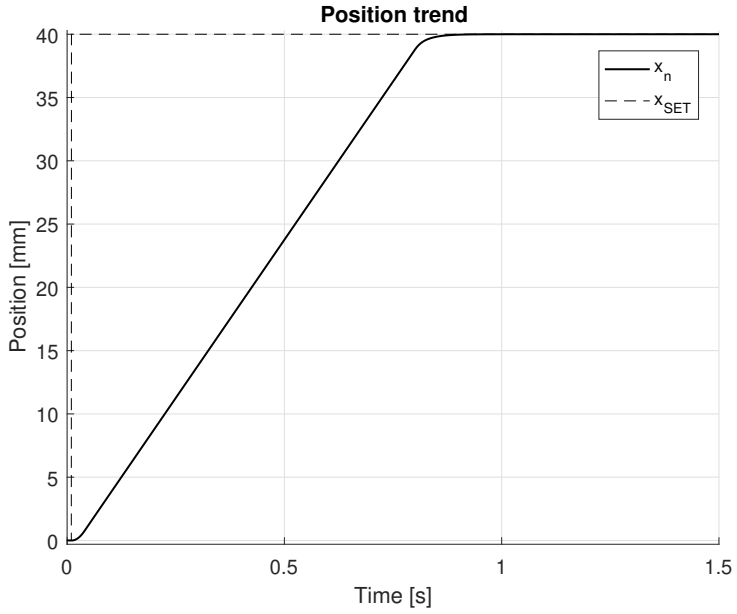

Figure 5.23: Position trend - No external load

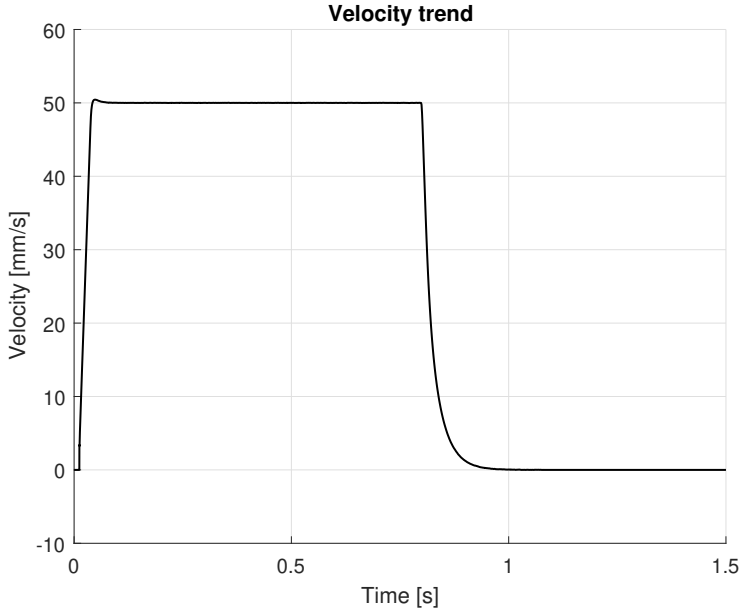

Figure 5.24: Linear velocity trend - No external load

Therefore, it is expected that the nut velocity trend should be trapezoidal, because the position has a first phase with high acceleration, a second phase with constant velocity, and a final deceleration phase. All these considerations are confirmed to the Figure 5.24. Furthermore, by observing Figure 5.25, the saturation velocity of the motor shaft is settled to $251\,rad/s$, at which corresponds an angular speed of the screw shaft equal to $63\,rad/s$.

Obviously, on the basis of these values, the linear velocity of the nut can be evaluated as reported in equation 5.33.

$$\dot{x_{n,\,max}} = \dot{\theta}_{max} \cdot \frac{p}{2\pi} \cdot \tau = 50\,mm/s \tag{5.33}$$

As it is expected, the angular and linear velocity have a trend that respects the derivative of the nut position. Moreover, both in the nut and angular velocity trends it is possible to observe a low overshoot which is caused by the controller design. However, the motor shaft manages to reach the maximum velocity with a high slope, thanks to the high torque provided by the motor during the acceleration phase. Therefore, it is possible to conclude that the servosystem has a good behavior when no external load is applied to the double nut.

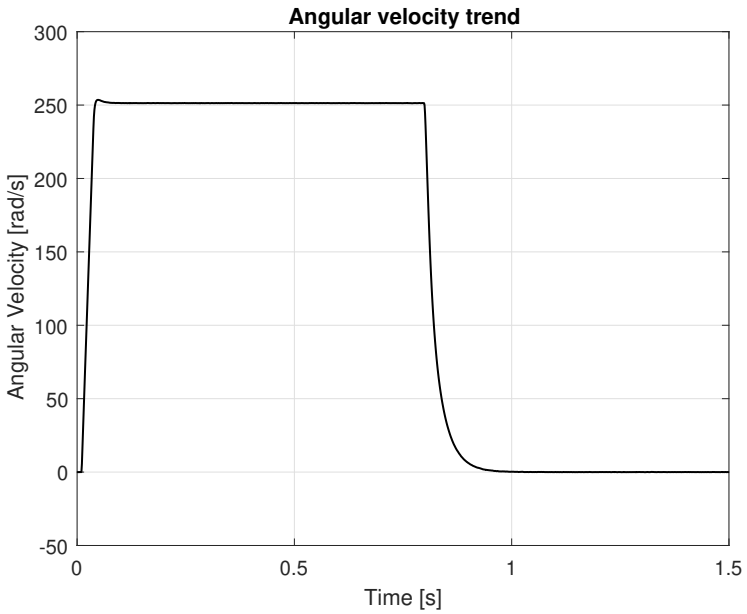

Figure 5.25: Angular velocity trend - No external load

In the Figure 5.26 the current trend is displayed. After a first acceleration phase, in which the current reaches its saturation value (equal to $25\,A$), a decrease occurs caused by the increase of current loop disturbance, which is the angular velocity of the motor shaft.
After the acceleration phase, an abrupt decrease occurs because the velocity amount to the saturation value. During this phase the current is very low because the motor has to provide a constant torque in order to equilibrate the friction force and torque applied on the servosystem. Obviously, when the deceleration phase is reached the current becomes negative in order to reduce the nut velocity until $0\,mm/s$. Furthermore, the current displayed in Figure 5.26 is filtered by the current sensor in order to cut-off the carrier frequency of the PWM modulation. Finally, it is possible to observe the effect of the

sensors noise, that affects the mean value of the current during the whole simulation.
In Figure 5.27 the torque provided by the motor shaft is depicted. In this case the torque trend is similar to the current trend. It is possible to observe that the maximum torque supplied by the motor is equal to:

$$T_{M,max} = k_t \cdot i_{max} = 37.5\,Nm \tag{5.34}$$

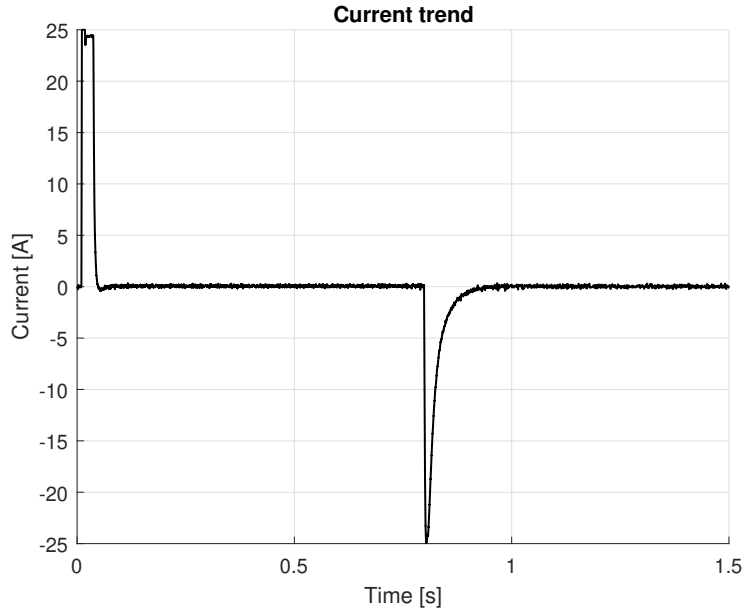

Figure 5.26: Current trend - No external load

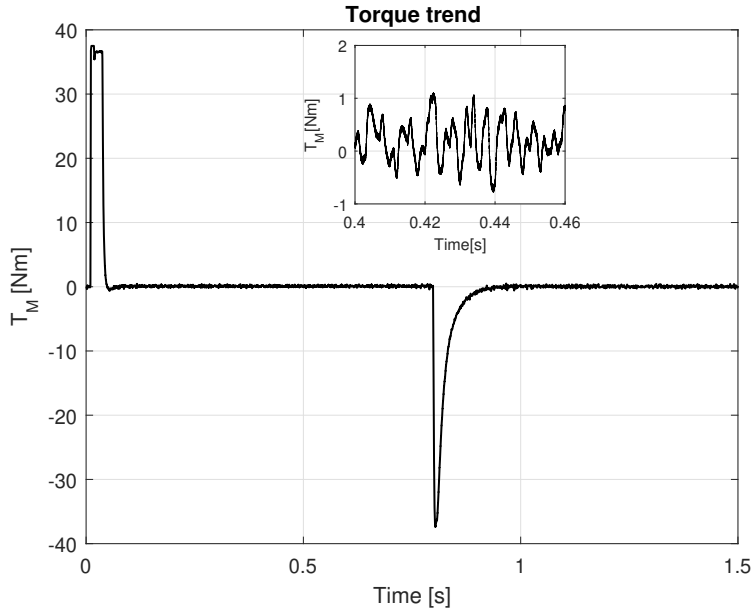

Figure 5.27: Torque trend - No external load

As depicted in the magnification of Figure 5.27, the torque during no-acceleration phase is not null but it is very low. Indeed, the motor has to provide an external torque that can equilibrate the friction force and torque, as explained before.
Then, this first analysis permits to understand the system response when the nut has to cover its total stroke. As depicted in the figures above, due to inertias phenomena the nut shows a delay compared to the command. Moreover, both velocity and current reach their saturation value, in order to arrive at the final position in the shortest time interval as possible.

5.7.2 External load applied

This subsection analyzes the servosystem behavior when an external load is applied. In particular, it is expected that the external load leads to higher friction and therefore decreased efficiency. Moreover, it will be possible to observe that to reach the same position a higher torque has to be provided by the motor in order to equilibrate the external force applied. This subsection analyzes the behavior of the servosystem by forwarding two different commands: step SET with $10\,mm$ of amplitude and a sine wave command with $\pm 1\,mm$ of amplitude and a $f = 2\,Hz$.

Step command

This simulation analyzes the behavior of the model by imposing a step command at $0.01\,s$.

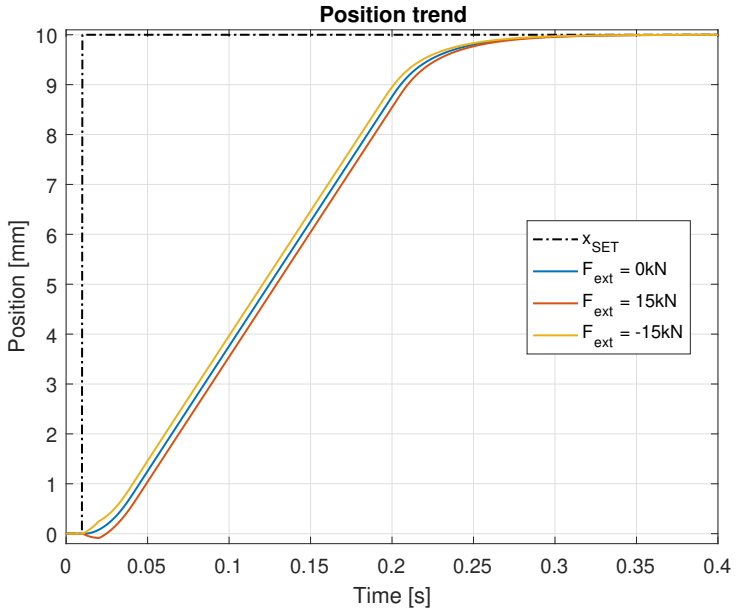

Figure 5.28: Position trend when an external load is applied

Furthermore, in correspondence of this time instant, an external load is applied. Three different cases are analyzed: no external load applied, an external load equal to $15\,kN$ and $-15\,kN$ with a ramp trend and a slope of $\pm 1500\,kN/s$.

The first load tends to obstruct the motion whereas the second load tends to promote the double nut motion. As a proof of this, the position trend is displayed in Figure 5.28. As this figure shows, a negative external load facilitates the motion. Indeed, a negative force creates a disturbance with a positive sign. This behavior is due to the sign of the external load in the equation 5.30. Indeed, it is possible to observe that if the external load is negative there is a positive displacement of the double nut and vice versa.

In the Figure 5.29 the angular velocity trend for the three analyzed cases is depicted. In particular, it is quite clear that the negative external load leads to a faster response but at the same time it causes a higher overshoot in the velocity. Indeed, this last tends to promote the motion and therefore leads to an increasing of the maximum velocity. In this case, the actuator acts like a brake after the acceleration phase, because the torque during the steady state is negative, as depicted in the torque trend. This last is represented in Figure 5.30.

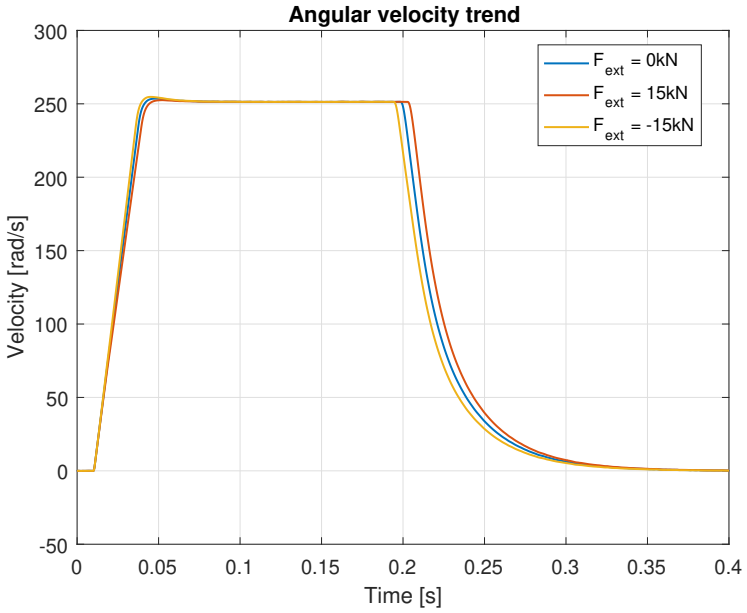

Figure 5.29: Angular velocity when an external load is applied

By observing this figure, several considerations can be carried out. First of all, it is quite understable why the case with a negative force applied has a greater time period in which the maximum torque is reached. Indeed, the controller notices the higher error caused by the external load and tends to reduce it by imposing the maximum current (and therefore a higher torque) for a larger time period. Moreover, it is possible to notice that the steady state torque is higher when an external load is applied. The value of the provided torque

is positive when a resistant force is applied to the double nut, negative in the other case. In order to verify the calculations, it is possible to evaluate the torque generated by the external force reported to the motor shaft:

$$C_M = F_{ext} \cdot \frac{p}{2\pi} \cdot \frac{\tau}{\eta} = \pm 3.14\, Nm \tag{5.35}$$

Indeed, as the magnification of Figure 5.30 depicts, this value is simular to the torque value evaluated by equation 5.35.

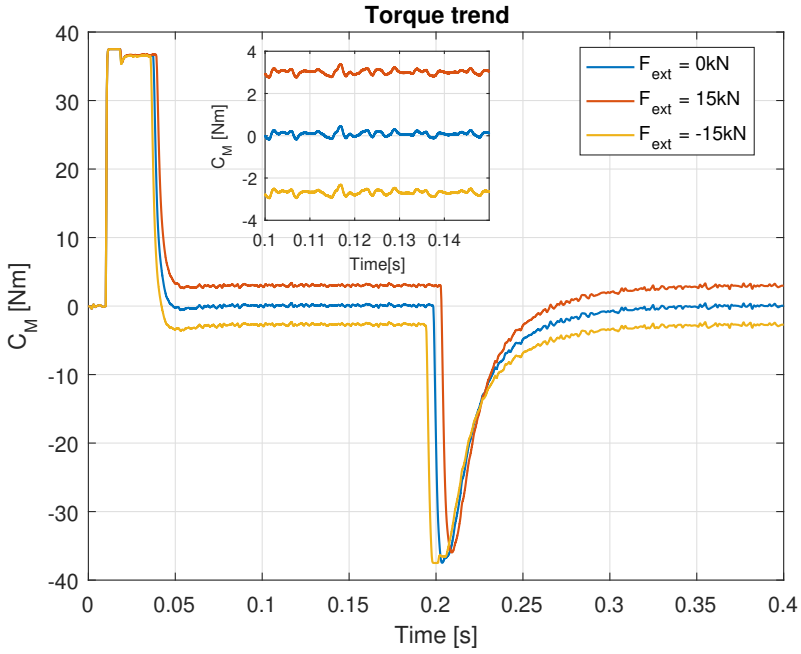

Figure 5.30: Motor torque trend when an external load is applied

Obviously, there is not a perfect correspondence between these two values because it is necessary to consider also the friction effects and the reaction torque. However, this preliminary verification allows to understand the exactness of the obtained result. Moreover, it is possible to conclude that the external load leads to a decreasing of the overall efficiency of the servosystem. Indeed, in order to obtain the same output position, it is necessary to provide a higher torque to equilibrate the applied force. This consideration can be observed in the midde and last part of Figure 5.30.

Furthermore, in the Figures 5.31 and 5.32 the friction torque and force trend are depicted in the three cases. In order to display results in the best way, the noise of the sensors is set to 0 in this case. As it is possible to observe in Figure 5.31, when no external load is applied, the friction torque has the typical Stribeck trend. However, in the other two cases it is possible to observe an increasing of the friction torque until the force reaches its maximum value. For this reason, the friction torque is higher if an external load is

applied to the double nut. This is caused by the rolling friction part of the equation 5.13 and 5.31.

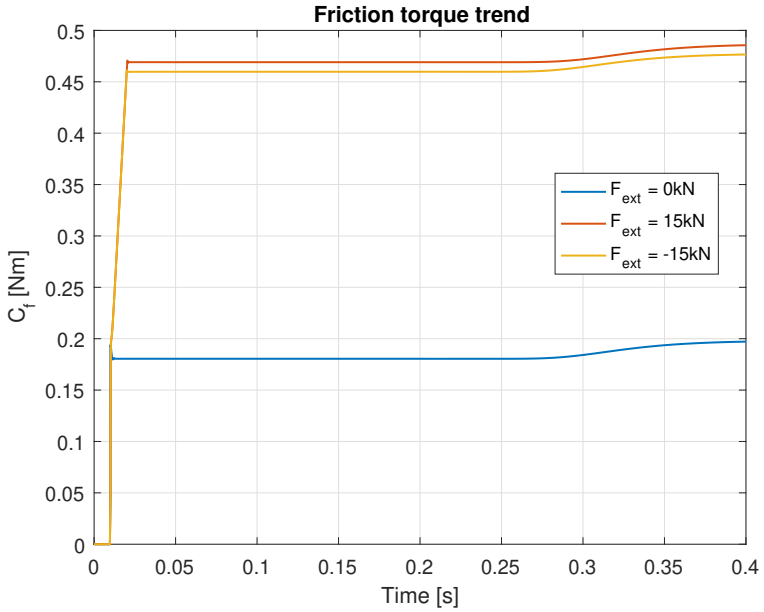

Figure 5.31: Friction torque trend

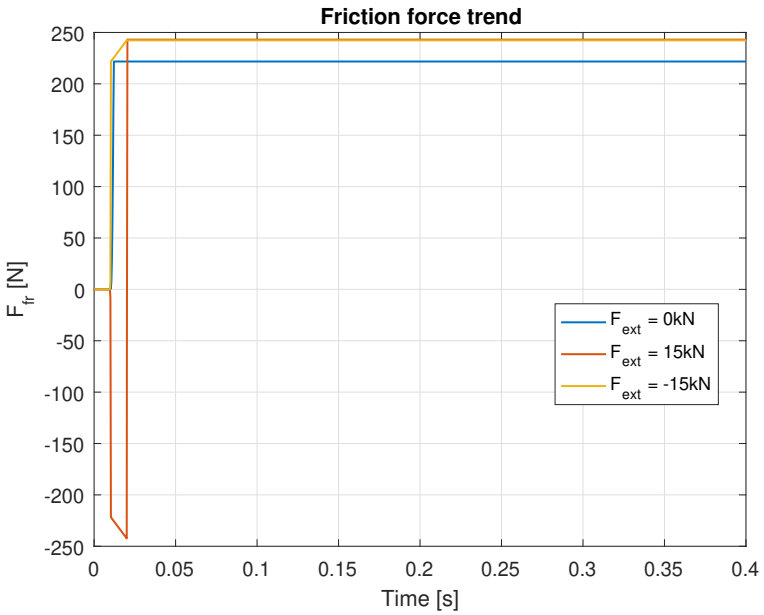

Figure 5.32: Friction force trend

Indeed, the external load leads to higher contact forces by causing increased friction forces and torques. Furthermore, when the force is positive the friction torque is higher than the last case. Indeed, when the $F_{ext} = 15\,kN$ the external and friction force have the same sign. For this reason, the contact forces in the balls have to be higher in order to reach the same final position. In the last part of the motion the friction torque increases gradually until reach the static value. In this respect, it is necessary to observe that the

friction torque is not null when the system arrestes its motion. Indeed, since the friction model is modelled in order to not have motion when the external torque is lower than the static friction value, then the final equilibrium is reached when the driving torque is a little bit lower than the static friction value. For this reason, the friction torque is not zero in the final part of the nut motion.
The same consideration can be carried out by observing the Figure 5.32. However, in this case the friction force does not have the Stribeck trend observed in 5.31, because it is neglected in equation 5.31. Furthermore, the differences between the second and last analyzed cases are less marked than the friction torque trend because the rolling friction part of the frictions models affects mostly the friction torque.

Sine Wave command

This simulation analyzes the behavior of the servosystem when a sine wave command is imposed with a frequency of $2\,Hz$ and an amplitude of $\pm 1\,mm$. In this subsection three cases will be treated: no external force applied, an external force of $\pm 10\,kN$ of amplitude with a sine wave trend and an external force of $\mp 10\,kN$ of amplitude with a sine wave trend, as depicted in Figure 5.33.
This type of simulation is performed because in-flight the external forces are not constant and can vary during time. Moreover, by observing Figure 5.33 the external force has the same phase and frequency of the command.

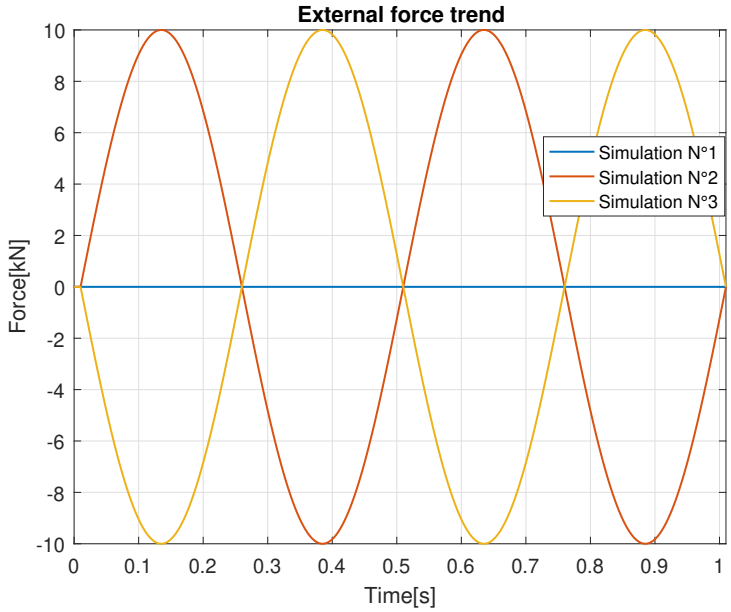

Figure 5.33: External force trend

By observing the Figure 5.34, it is possible to conclude that the external load applied in the second simulation obstructs the motion of the double nut. Indeed, this trend of

the external force creates a disturbance that has the opposite sign of the imposed command. For this reason, when an external load of $\pm 10\,kN$ is applied, the servosystem results slower. Obviously, this behavior is due to the finite stiffness of the servosystem. Indeed, if the latter has an infinite stiffness, the external disturbance should not affect the position or angular velocity. However, the finite value of the ball screw stiffness leads to the behavior depicted in Figure 5.34.

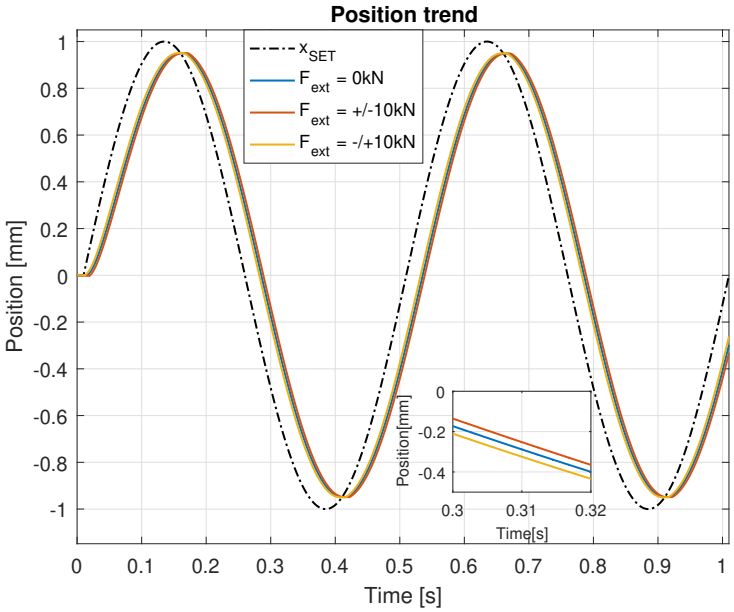

Figure 5.34: Position trend - Variable force applied

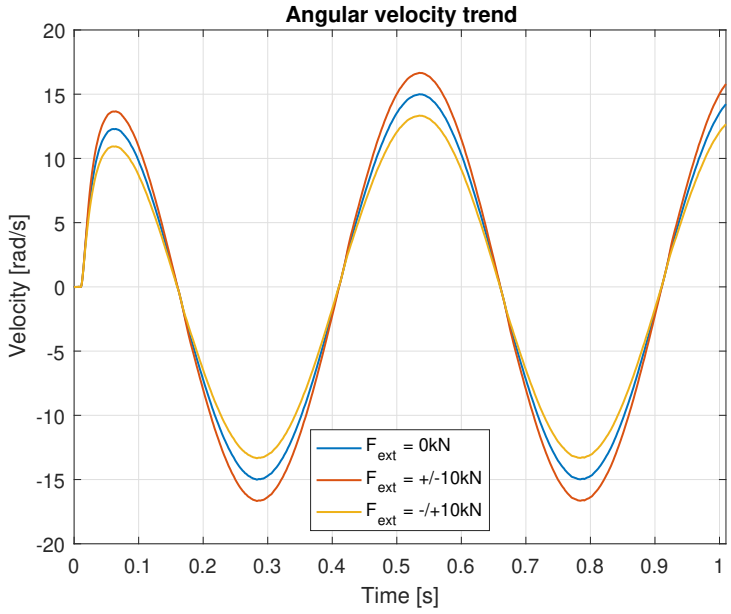

Figure 5.35: Angular velocity trend - Variable force applied

Moreover, in Figure 5.35 the angular velocity trend of the screw shaft is depicted. As the figure shows, the second simulation in this case has a higher value of the angular velocity

than the third one. Indeed, the controller notices the higher error caused by the external force and tends to impose a higher angular velocity to reduce it.
However, despite of the higher angular velocity of the screw shaft, the driving torque in the second case is lower than the third simulation, as the Figure 5.36 shows.

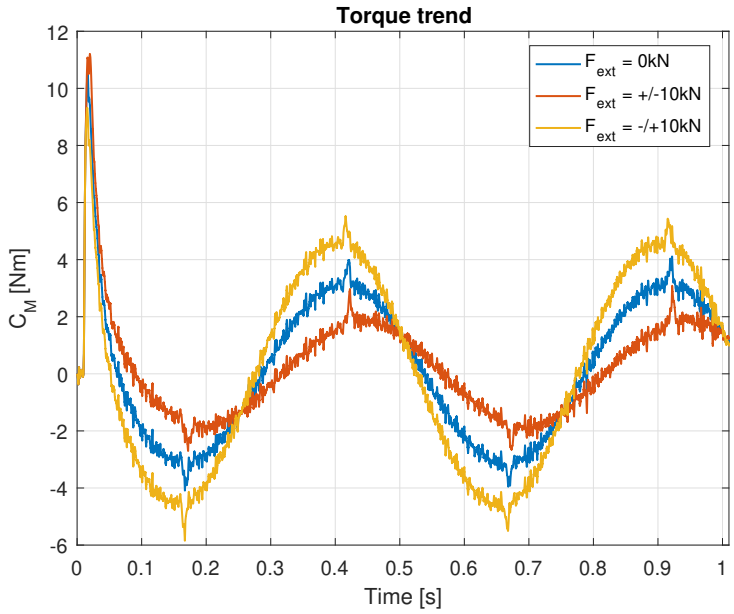

Figure 5.36: Driving torque trend - Variable force applied

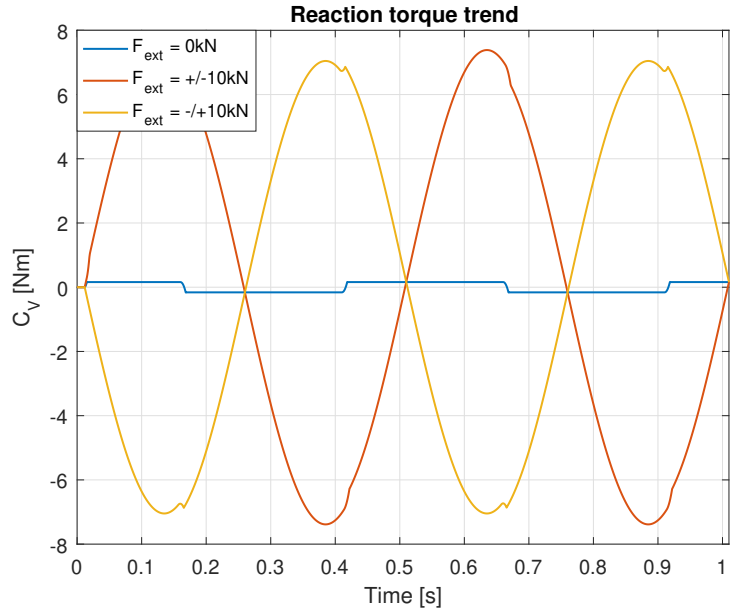

Figure 5.37: Reaction torque trend - Variable force applied

Indeed, it is necessary to take into account the effect of the reaction torque in the screw shaft equilibrium, which is depicted in Figure 5.37. In particular, a positive external load creates a positive reaction torque and vice versa. Furthermore, by comparing the Figure 5.37 and 5.36, it should be noted that the reaction torque has for a larger time interval

the opposite sign of the driving torque when a positive load is applied. Since the C_V is subtracted by the driving torque, then to have a higher acceleration of the screw shaft, the motor has to provide a lower driving torque. Despite of these considerations, the finite stiffness of the servosystem leads to a slower response, because in the second case the force obstructs the double nut's motion. The opposite situation occurs in the third simulation.
In particular, this simulation allows to understand the principal causes of the finite stiffness of the servosystem. Indeed, it is clear that in this case is not satisfied the correlation between the angular velocity of the screw shaft and the nut linear velocity:

$$\frac{x_n}{\Omega} \neq \frac{p}{2\pi} \tag{5.36}$$

$$\frac{\dot{x}_n}{\dot{\Omega}} \neq \frac{p}{2\pi} \tag{5.37}$$

5.7.3 Effect of the preload force

In this subsection the effect of the preload force in the servosystem behavior is analyzed. As explained in the previous sections, the preload force causes an increasing of the ball screw stiffness at the cost of higher frictions. This subsection treats the servosystem behavior by imposing a sine wave SET command with a $f = 3\,Hz$ and an amplitude of $\pm 0.5\,mm$ for different types of ball screws: no preloaded ball screw, a preloaded ball screw with $F_{pr} = 1\,kN$ and a preloaded ball screw with $F_{pr} = F_{pr,\,ISO}$.
In particular, the last preload value is the suggested value by (ISO 3408-4:2006) and can be computed as reported in equation 5.38 [1].

$$F_{pr,\,ISO} = \frac{F_{ext}}{2.83} = \frac{0.5 \cdot F_{ext,\,max}}{2.83} \tag{5.38}$$

Where F_{ext} is the applied external force. In this respect, it is supposed to apply an external load of $10\,kN$ in correspondence of $t = 1\,s$ with a ramp trend. In particular, the force employs $0.01\,s$ to reach its final value. For this value of external load the preload suggested by ISO is equal to $F_{pr,\,ISO} = 3.5\,kN$.
The Figure 5.38(a) depicts the position trend for the imposed command whereas the Figure 5.38(b) represents a magnification of the disturbance in the three cases. As it is possible to observe, when the preload increases the stiffness of the ball screw becomes higher, by leading to a lower disturbance when the external load is applyed. For this reason, the preload force improves the precisioning of position of the ball screw.
However, as it can be observed in the friction torque and force trends depicted in the Figure 5.39 and 5.40, the preload force causes an increasing of the friction in the first part

of the motion. In particular, the differences are more marked in the friction torque plot. Indeed, as afore explained, the rolling friction part affects mostly the friction torque.

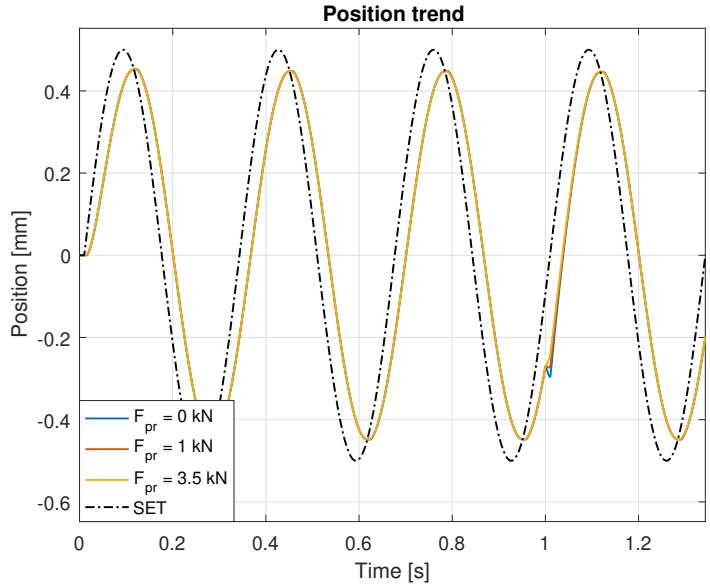

(a)

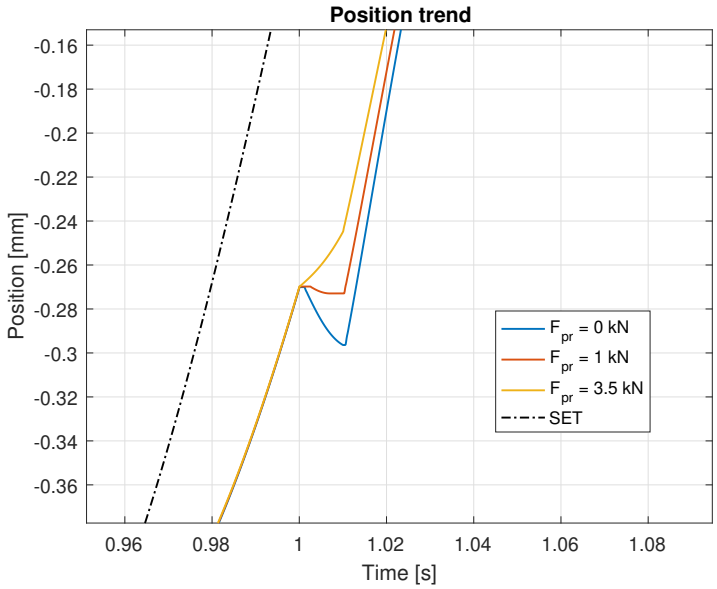

(b)

Figure 5.38: Position trend (a) and magnification of the disturbance (b)

As it is possible to observe, until the load is not applied, the preload force leads to higher friction forces and torques. Indeed, the preload force causes an increasing of contact forces during the first motion phase. For this reason, the value of the preload has to be evaluated accurately, because it can lead to decrease efficiency of the actuator.

Finally, by observing the two figures it is clear that the friction phenomena become super-

imposed after the load application. In fact, the preload does not affect the nut position but it appears only in the equilibrium equation of each nut with opposite signs. For this reason, when the external load is higher than the preload, higher contact forces occur in one nut compared to the no preloaded ball screw. However, in the other nut the contact forces will be lower than the no preloaded ball screw. For this reason, the total sum of the contact forces do not change for symmetry, then the friction forces and torques will be equal.

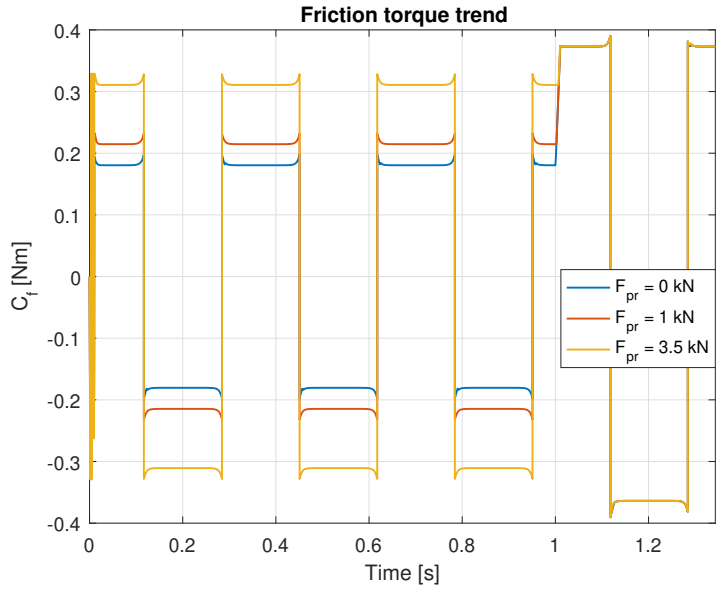

Figure 5.39: Friction torque trend by varying the preload

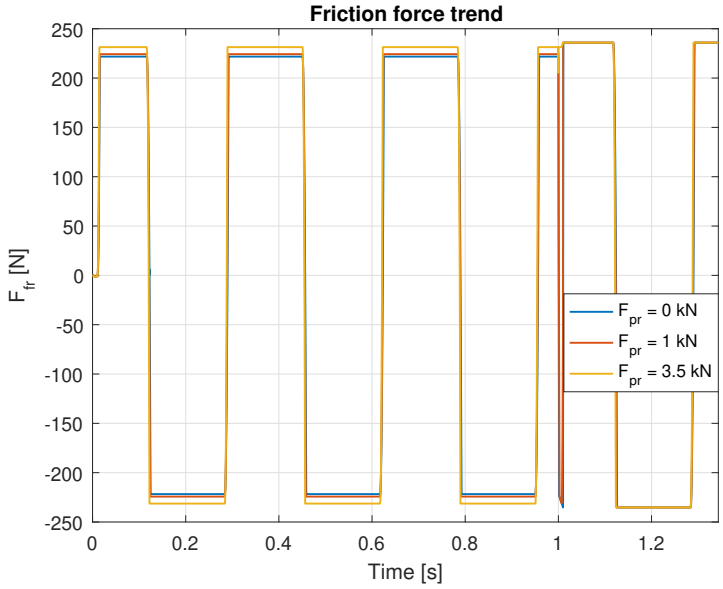

Figure 5.40: Friction force trend by varying the preload

5.7.4 Effect of the degradation

In this subsection the effects of the degradation in the servosystem behavior are analyzed. It is important to carry out this type of simulation because the axial play, the friction force and torque represent the principal parameters that increase due to degradation effects. Indeed, the degradation effects are simulated by increasing the friction torque, force and backlash up to four times the nominal value and $100\,\mu m$ respectively. In particular, these last parameters correspond to the value of 100% of degradation, as the following pictures will display.
By running the model in open-loop it is possible to highlight the effects of degradation in the actuator's accuracy. Indeed, if the position controller does not operate, it is expected that the precisioning of position decreases. In this respect, a velocity step command of $30\,rad/s$ and a cosine wave command of $\pm 30\,rad/s$ of amplitude and $f = 2\,Hz$ are analyzed in the first two paragraphs.
On the contrary, by running the model in closed-loop it is possible to underline the effects of degradation in the motor current. Indeed, the position proportional controller imposes higher current in order to reach the same double nut final position. In this section, a sine wave command with $A = \pm 0.5\,mm$ and $f = 2\,Hz$ is analyzed. All the simulations are conducted without external force applied, in order to underline the effect of the backlash in the servosystem.

Step command - Open loop

As afore explained, in this subsection the effect of the degradation in the actuator's accuracy will be analyzed. In particular, it is expected that this last leads to a lower precisioning of position as well as higher delay.
The Figure 5.41 represents the angular velocity of the motor shaft in the three analyzed cases. It is possible to observe that the three trends are superimposed because the parameter which most affect the behavior of the servosystem is the backlash. Since this last is included in the model after the screw shaft equilibrium, then the angular velocity of the motor shaft is slightly affected by degradation effects. Therefore, it is now interesting to investigate how the degradation affects the precisioning of position and the double nut linear velocity. Indeed, the double nut velocity depicted in Figure 5.42 shows clearly the delay introduced by the increased friction and backlash. By increasing the degradation there is higher delay as well as higher instabilities when the motion starts; these last are due to the axial play. Indeed, the contact forces are null until the contact between ball and either nut or screw occurs. For this reason, there is an abrut impact when the motion starts which leads to high noises during operation. At the same time, the amplitude of the peak becomes higher by increasing the backlash value. Furthermore, when the velocity

becomes null at $0.2\,s$, only the ball screw without backlash manages to reverse its motion. Indeed, the blue trend of Figure 5.42 shows a peak due to the transition from static to dynamic friction at $0.22\,s$. On the contrary, in the other two cases this transition does not occur because the axial play causes loss of motion. Therefore, it is expected that the double nut position trend shows a higher delay and a lower precisioning of position when the degradation raises.

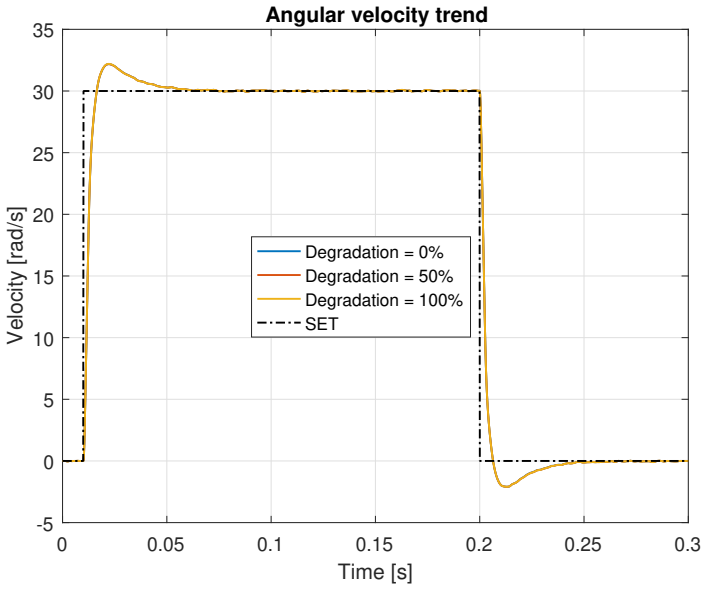

Figure 5.41: Angular velocity imposed to the servosystem

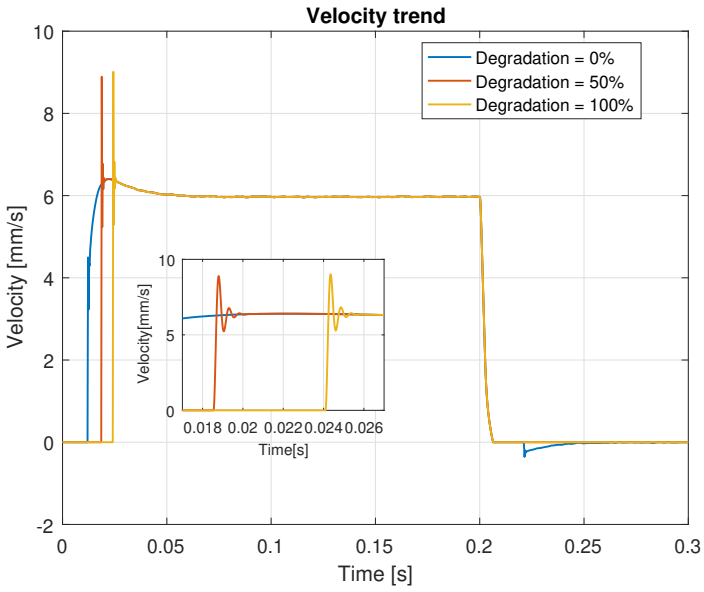

Figure 5.42: Linear velocity trend of the double nut by varying degradation effects

Indeed, as it is possible to observe in Figure 5.43, if the backlash and friction increase a dead band occurs. At the same time, the final position results lower by increasing the degradation, because in this analysis the servosystem is running in open-loop as before

mentioned.

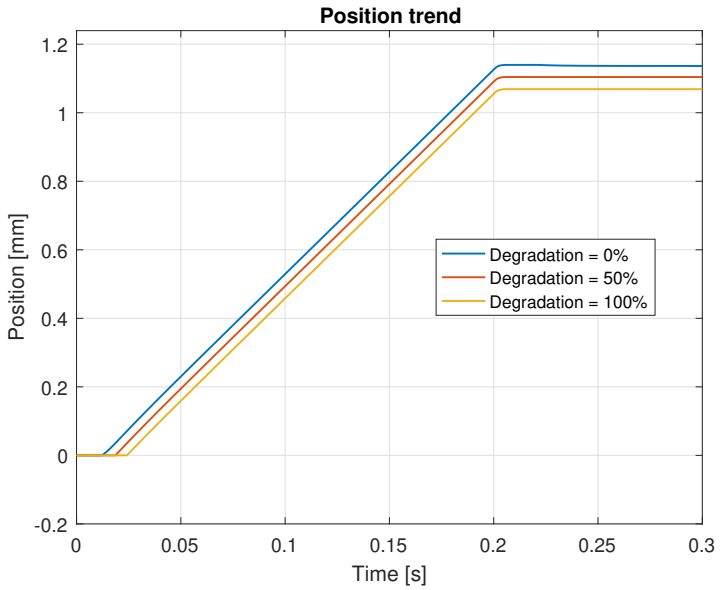

Figure 5.43: Position trend of the double nut by simulating degradation effects

This first simulation allows to comprehend that the position can represent a useful index to monitor the health state of the actuator. Indeed, when a persistent decreasing of ball screw's accuracy is detected, it is possible to conclude that the ball screw has to be replaced because deeply affects to degradation effects.

Cosine wave command - Open loop

In this second subsection, the behavior of the servosystem by imposing a cosine wave velocity command in open-loop is briefly analyzed. The command frequency is $f = 2\,Hz$ whereas the amplitude is $\pm 30\,rad/s$. Obviously, it is expected to obtain a decreasing of accuracy due to the dead zone introduced by the axial play and increased friction.
As before carried out, firstly the command is displayed in the Figure 5.44. In particular, it is possible to observe that the three trends are superimposed because the motor shaft angular velocity is slightly affected by degradation effects as before explained.
Furthermore, the backlash influences only the double nut velocity and position. Therefore, these two parameters are displayed in the Figures 5.45 and 5.46 during the simulation time. As the Figure 5.45 shows, several instabilities can be observed when the inversion of motion occurs. This behavior is obviously similar to the linear velocity trend explained in the previous subsection. However, in this case the instabilities occur at each inversion of motion, by resulting in larger peaks than the previous case.
Furthermore, it is interesting to observe Figure 5.46, that shows the position trend for the three analyzed cases. This figure allows to comprehend that the degradation strongly

influences the precisioning of position because in the third simulation the amplitude of the command is lower than the first one. Furthermore, it is possible to observe that the backlash and increased friction cause loss of motion, as it was predicted in the previous rows. Finally, the dead bands cause a delay both in the position and linear velocity, by leading to decreasing servosystem performances.

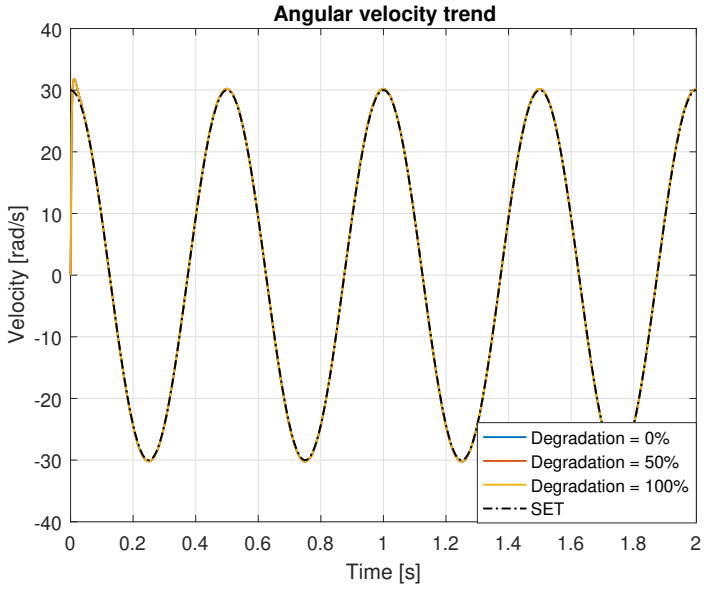

Figure 5.44: Cosine wave command applied to the servosystem

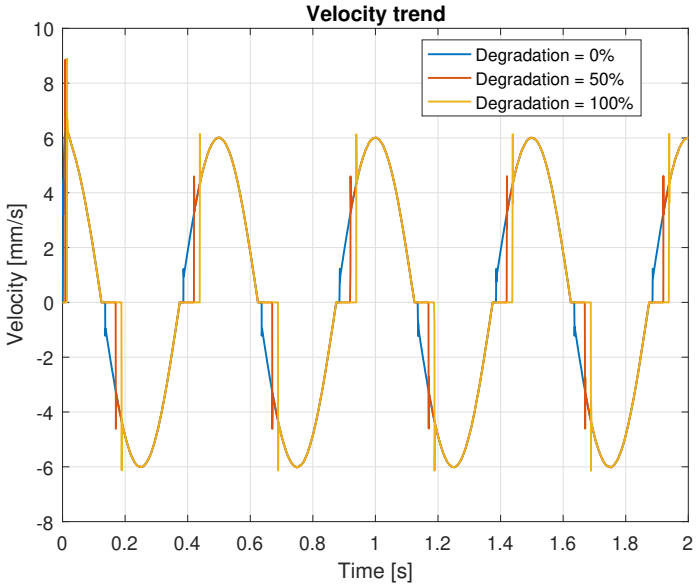

Figure 5.45: Linear velocity of the double nut by varying degradation effects

How it will be explained in the next chapter, the deviations between the nominal and current conditions of the ball screw will be analyzed both for a step and a cosine wave command. Indeed, by combining the two analyses, it is possible to increase the reliability of the results, that in the real ground tests are not deterministics.

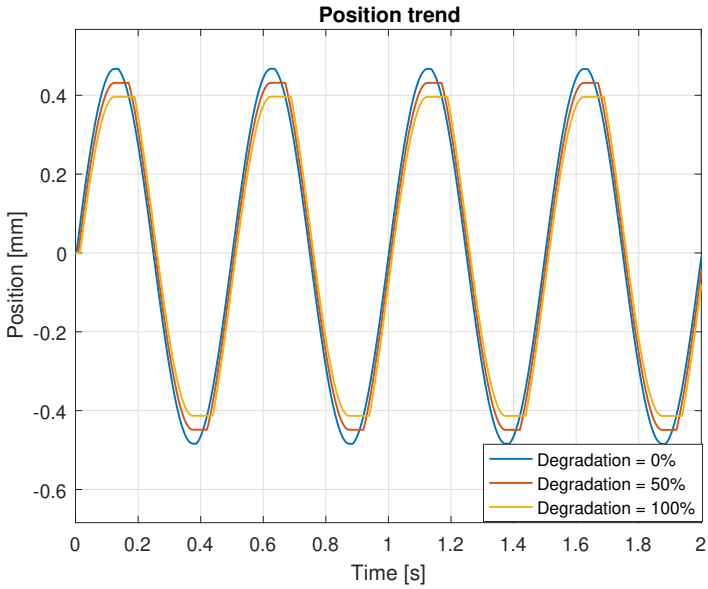

Figure 5.46: Position of the double nut by varying degradation effects

Sine wave command - Closed loop

In this third analysis, a sine wave command is forwarded to the servosystem in closed-loop.

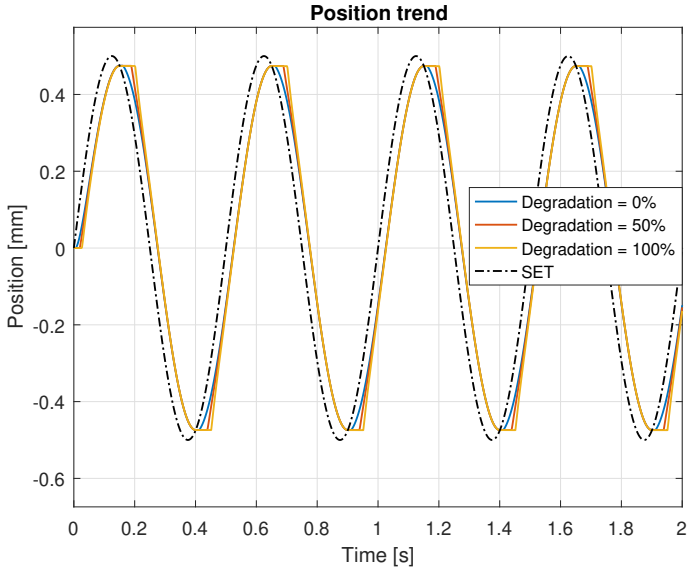

Figure 5.47: Position trend by running the model in closed loop

In this case it is expected that the servosystem will reach the same final position at the cost of higher current. Indeed, the proportional controller detects the dead band introuduced by the backlash and increased frictions and it imposes higher current to reduce as soon as possible the error between the SET and feedback position.

By observing the Figure 5.47, it is possible to conclude that the before mentioned hypotheses are veryfied. Indeed, thanks to the proportional controller of the position loop, in all cases the ball screw manages to reach the same final position. However, as the magnification depicted in Figure 5.48 shows, when the inversion of motion occurs there is a dead band caused by degradation effects. After this short delay the trends become superimposed because the controller imposes higher currents in order to reduce the error caused by the increased degradation. Therefore, the degradation effects in closed-loop affect in particular the current, which can represet a useful index to detect these phenomena in ball screws.

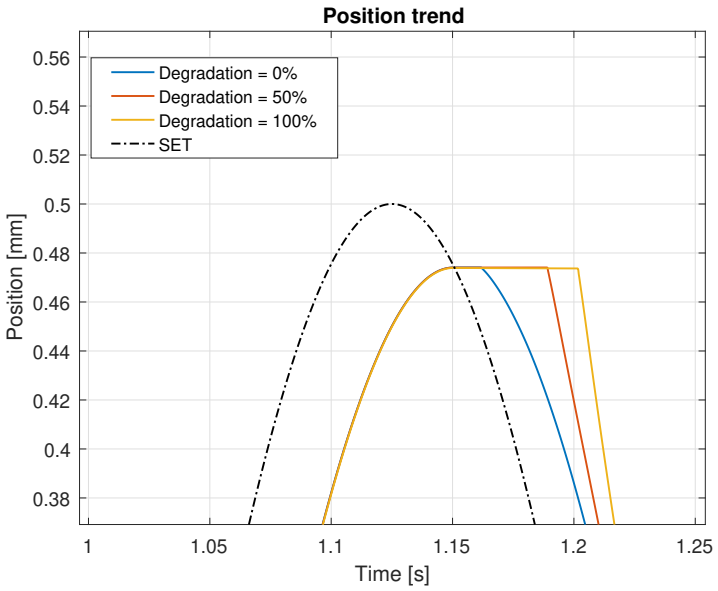

Figure 5.48: Magnification of the inversion of motion

As a proof of this, the current and torque provided by the motor are represented in the Figures 5.49 and 5.50. In particular, it is possible to observe several peaks whose amplitude increases with the increasing of the degradation. The parameter that mostly affected the current is the backlash, because it causes a short time interval in which the contact forces are null.

Furthermore, due to the dead band introduced by degradation effects the position controller notices the raising of the error and it tries to impose a higher current. However, when the contact starts, an abrupt impact occurs and the acceleration results too high. For this reason, after the peak the Figures 5.49 and 5.50 show a sudden decreasing of current and torque, in order to restart the motion the normal way.

In this respect, it is possible to observe that the maximum current becomes up to two times higher than in the nominal case. These differences between nominal and current status are certainly higher than the deviations in the precisioning of position before analyzed. For this reason, the current represents an another useful index to monitor the

actuator health state as well as predicting its remaining useful life. In particular, in the following chapter the HUMS embedded in the Matlab/Simulink model will be explained on the basis of the results obtained in this chapter.

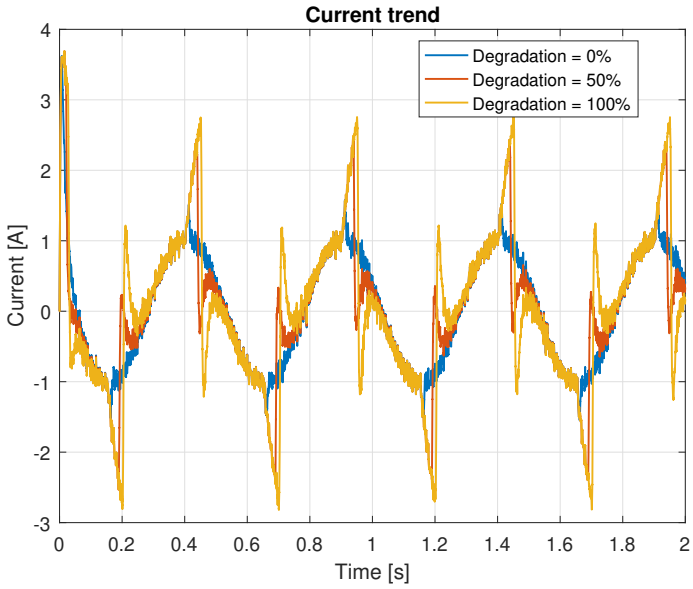

Figure 5.49: Current trend

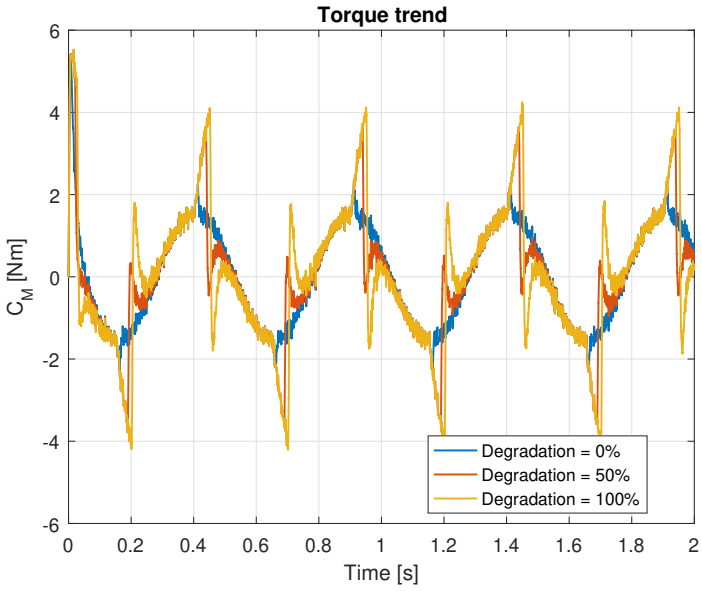

Figure 5.50: Torque trend

Chapter 6

HUMS in the Simulink model

In this chapter, the Health-and-Usage-Monitoring-System applied in the EMA model is analyzed. In order to do that, it is necessary to develop another symple model which reflects the nominal conditions of the high fidelity model. Indeed, the first section of this chapter shows the afore mentioned symplified model and it provides a comparison between this last and the high fidelity model.
After that, the methodologies by which the Health-and-Usage-Monitoring-System can be carried out are explained. As it was shown in the fourth chapter of this thesis, the possible faults in the ball screw can be detected when a persistent deviation between the nominal model and the real model can be detected. In this thesis it is supposed to simulate the degradation effects by increasing the friction torques and forces as well as the backlash. In particular, two methodologies are carried out; the first one uses the deviations between the nominal and faulted current's frequency spectrum to detect degradation in ball screws. The second proposed methodology utilizes several indexes capable to detect the deviations of sensitive parameters such as position and current. Successively, the health monitoring part based on these methodologies is explained in the fourth section. Finally, the last section explains how the Usage part can be performed by utilizing the current index.

6.1 Monitoring Model

As it was treated in the fourth chapter, the degradation and wear mechanisms in the ball screw can be detected only if persistent deviations from the nominal conditions can be observed. In order to have a comparison between the current health of the ball screw and the nominal conditions, a symplified EMA model is developed, as depicted in Figure 6.1. This last does not have to be too complex in order to reduce the computational burdern but at the same time it has to be capable to reproduce the behavior of the high fidelity model explained in the previous chapter.

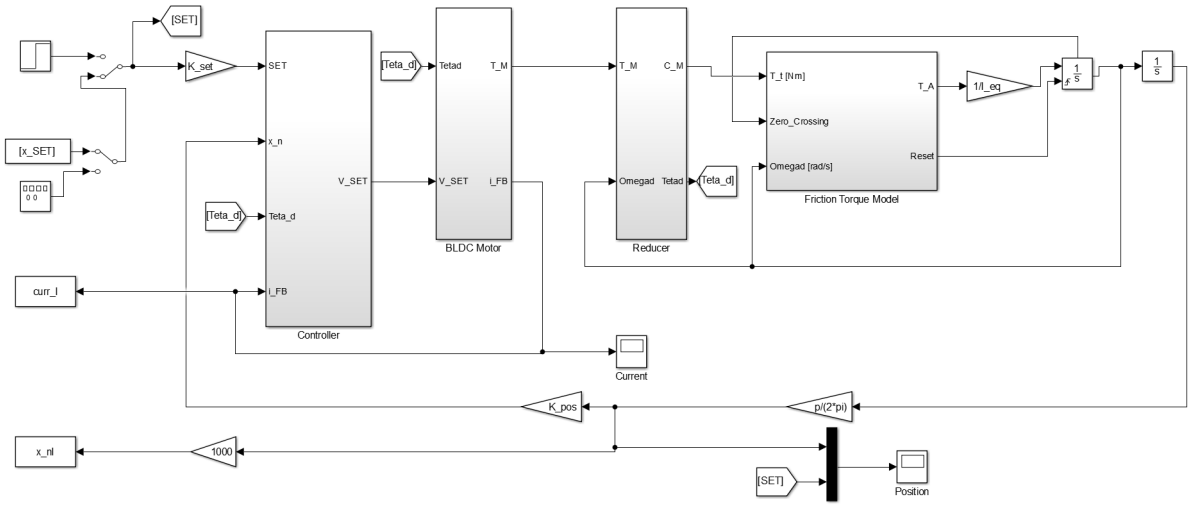

Figure 6.1: Monitoring model

As it is possible to observe in Figure 6.1, the monitoring model is composed by the same subsystems contained in the ball screw model of the previous chapter. However, in this case the PWM modulation is neglected because it would have implied to reduce the maximum time step of the solver. Since the monitoring model has to be capable to carry out an on-line monitoring, then it is supposed to neglect the PWM modulation by hypotisizing a carrier with an infinite frequency.
Finally, it is possible to observe that the whole ball screw is simulated as a simple second order transfer function:

$$C_m - 2 \cdot C_{f,nom} = I_{eq} \cdot \ddot{\Omega} \tag{6.1}$$

Where:

- C_m is the driving torque
- $C_{f,nom}$ is the friction torque in the nominal conditions. In particular, it is possible to observe in Figure 6.1 that the friction model is equal to the subsystem implemented in the high fidelity model. Indeed, it is necessary for obtaining good results that the friction values are coincident in nominal conditions. Moreover, the friction torque is considered two times in order to take into account both the friction model in the screw shaft and in the double nut. Finally, in this analysis the rolling friction part of the friction model is neglected because it influences only slightly the friction trend if no external load is applied to the servosystem
- I_{eq} is the equivalent inertia model of the whole EMA
- Ω is the angular position of the screw shaft

Once evaluated the angular position of the screw shaft, it is possible to compute the position of the double nut by considering the ball screw as a screw-nut coupling:

$$x_n = \frac{p}{2\pi} \cdot \Omega \tag{6.2}$$

The controller parameters are tuned in order to have a similar behavior between the two models. In particular, the proportional and integral gains of the two PIs controller are equal to the high fidelity model. Indeed, the motor and the first equilibrium equation are similar to the complex model and there only small differences in the transfer functions of these two loops. However, the proportional gain of the position controller is evaluated by utilizing the function *fminsearch*, which allows to compute the value of k_p that minimize the differences between the real displacement of the nut and the displacement obtained from the monitoring model. In particular, the developed algorithm is based on [29]. It is capable to find the value of k_p that minimize the error between the high fidelity model in the nominal conditions and the monitoring model.
By imposing as first attempt a value of $k_p = 20$, it is possible to observe that the *fminsearch* function allows to obtain an optimize result, because after the optimization process, the position trends derived from high fidelity and monitoring model are superimposed.

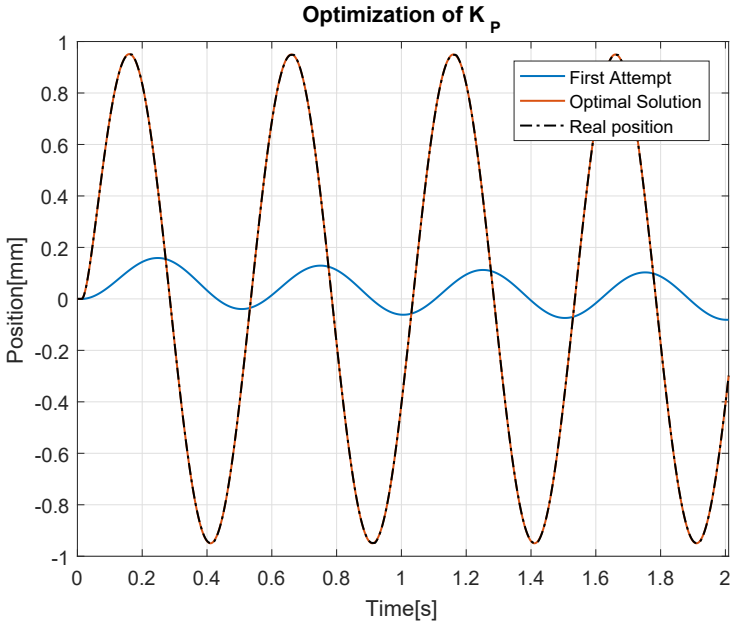

Figure 6.2: Optimization with fminsearch by imposing a sine wave command

Indeed, it is possible to observe in the Figure 6.2 that the first attempt does not reproduce the position trend derived from the high fidelity model. However, after the optimization the two trends are essentially superimposed ($k_{p,\,opt} = 663$).
As a proof of this, in the Figure 6.3 the position trends of the two models are depicted,

by forwarding a step command when the high fidelity model is in the nominal conditions. As it is possible to observe in the Figure 6.3, the monitoring model reproducts very well the behavior of the complex model also when a step command is imposed. Indeed, there are only low differences between the two models that are conservatives anyway.

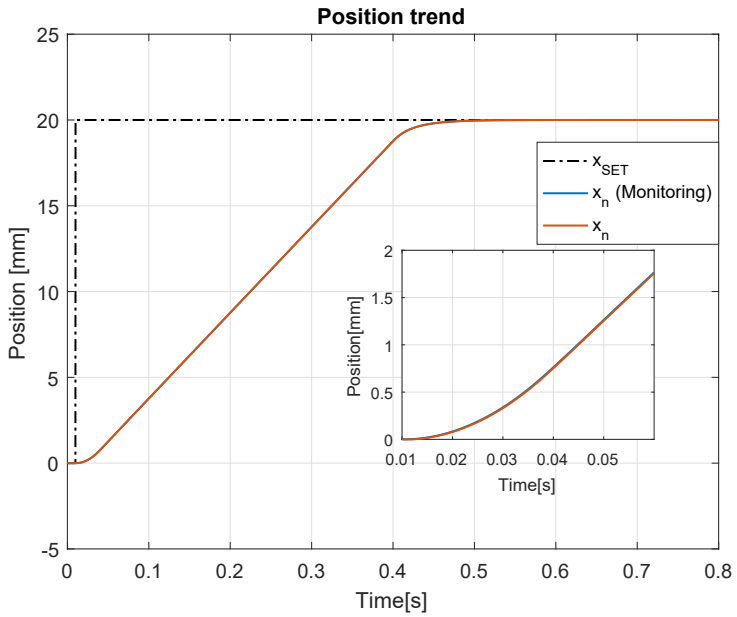

Figure 6.3: Position trend for a step for both monitoring and high fidelity model

Obviously, these differences are due to the simplyfied analysis conducted in the monitoring model. Indeed, the reaction torque due to the contact point is not considered. Furthermore, the mechanical stiffness of the monitoring model is infinite because the contact points are considered as perfectly rigid. Indeed, the Figure 6.3 shows that the monitoring model has a faster response than the high fidelity model. Since the ball screw's stiffness is infinite in this case, then the servosystem is less affected by friction phenomenon.
Moreover, since the current represents the second index by which the HUMS can be conducted, in Figures 6.4 and 6.5 the current trends for the same command analyzed before are depicted. Also in this case only negligible differences can be observed in the two figures. In particular, the Figure 6.4 allows to understand that the current mean values during the steady state are coincident in both cases. Furthermore, the Figure 6.5 shows that the highest differences in the two current trends occur when there is the transition from static to dynamic conditions and vice versa. Indeed, the different values of discontinuities are due to the lower mechanical stiffness of high fidelity model and the reaction torque, which is neglected in the monitoring model.
Finally, in the monitoring model the noise, that strongly affects the current trend in the complex model is not taken into account. For this reason, the simulations are conducted in order to forward commands that are not too much affected by the noise effects. Indeed,

for low command frequencies and amplitudes the current becomes very low. In these conditions, the results are strongly affected by the noise effects and therefore no prediction of the actuator health state can be carried out.

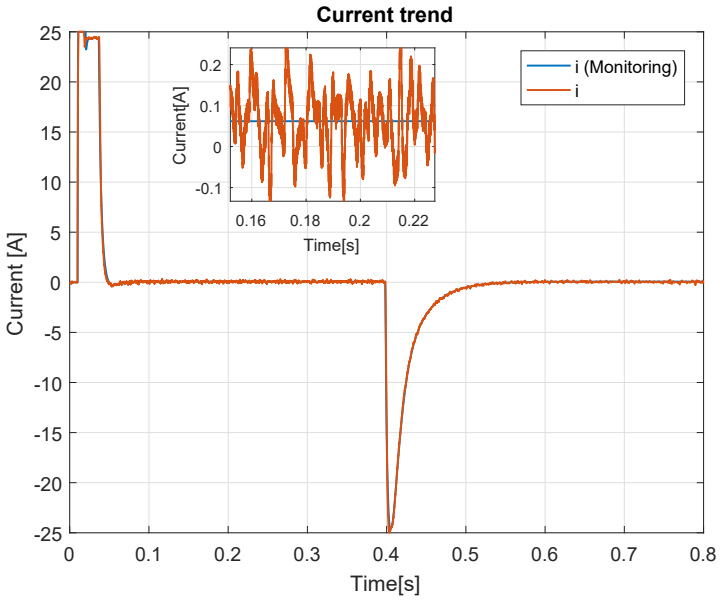

Figure 6.4: Current trend for a step for both monitoring and high fidelity model

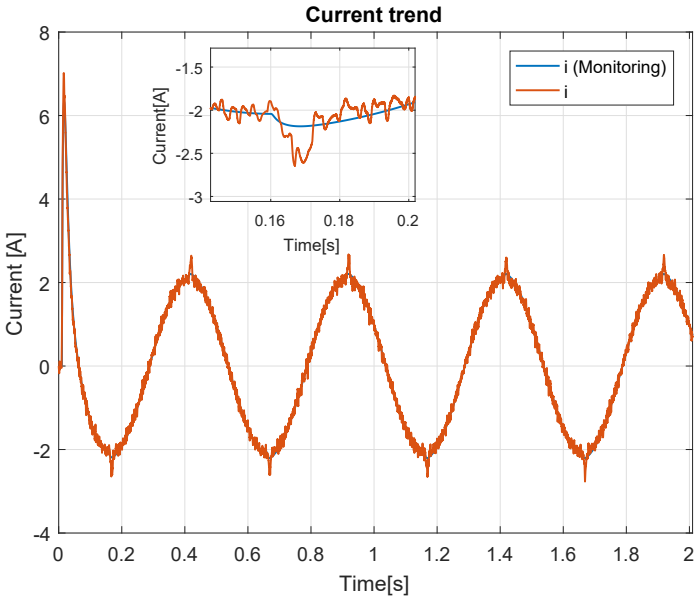

Figure 6.5: Current trend for a sine wave for both monitoring and high fidelity model

6.2 Health and Usage Monitoring

In order to evaluate the health state of the electro-mechanical actuator, it is necessary to identify useful methodologies through which an evaluation of the degradation effects can

be carried out. In particular, on the basis of the studies reported in [30] and [31], it is possible to define several methodologies to carry out a diagnostic and prognostic study of the ball screw. In this thesis the health state of the EMA is carried out by utilizing two methodologies. In the first one the frequency spectrum of the current is utilized to identify deviations between the nominal and faulted conditions. Obviously, this methodology can be useful only under a health monitoring point of view, because it is not possible to obtain a projection of the EMA's future life.
On the contrary, by utilizing the indexes defined in [30] and [31], it is possible to carry out both the Health and Usage monitoring. Obviously, all the explained indexes can be useful under a prognostic and diagnostic point of view only if a monotonic trend can be observed during the degradation effects. Since the aircraft tests are performed on the ground, all the simulations are carried out without external load applied to the ball screw and imposing deterministic command to the servosystem.

6.2.1 Fast Fourier Transform

As it was explained in the chapter 4, the frequency domain analysis can represent a useful mean to identify possible faults in ball screws. In particular, the frequency spectrum of a specified signal can be obtained by recurring to the Fourier transform. This last approximates the signals in a series (continuos Fourier transform) or a finite sum of sine and cosine wave functions. In particular, the discrete Fourier transform of a N-sampled function approximates the continuous Fourier transform and can be expressed as [32]:

$$F[n] = \sum_{k=0}^{N-1} f[k] e^{-2\pi j k n/N} \tag{6.3}$$

Therefore, thanks to equation 6.3, it is possible to turn a sampled function expressed in the time domain *f[n]* in another sampled function expressed in the frequency domain *F[n]*. In particular, in the Matlab/Simulink environment, it is possible to compute the FFT which represents a more optimized method to evaluate the Fourier transform of the analyzed signal. This last is utilized to evaluate the frequency spectrum of the current signal, in order to highlight the differences between nominal and current conditions of the actuator.

6.2.2 Mean error

The mean error computes the absolute value of the error between the nominal condition $x_{n,N}$ obtained from the monitoring model and the real position derived from the high fidelity model x_n. In particular, this error is integrated in the time interval in which the

simulation is run [31]:

$$|e| = \frac{1}{T} \cdot \int_0^T |x_{n,N} - x_n| \, dt \tag{6.4}$$

As the equation 6.4 shows, this parameter evaluates the mean error between the nominal and real position of the double nut during the simulation time. When the actuator is in the nominal conditions this parameter is similar to $0\,mm$, because the real position is comparable to the nominal one. However, due to degradation effects simulated with the increasing of backlash and friction forces and torques, the error increases up to non acceptable values. However, how the next sections will show, the maximum values of this index are too low to detect possible faults. However, it can represent a useful index to identify the exactiness of the performed simulations.

6.2.3 Fidelity coefficient

This coefficient can be used when the actuator is unloaded or subjected to low forces. In particular, in this thesis all the simulations are carried out without an external load applied to the ball screw, because the pre-flight tests are usually performed on the ground, when no external loads act on the servosystem. In this respect, two fidelity coefficients are analyzed in this thesis, both for the position and current [30, 31]:

$$C_p = \int_0^T \frac{x_{n,N} \cdot x_n}{x_n^2} \, dt \tag{6.5}$$

$$C_i = \int_0^T \frac{i_N \cdot i}{i^2} \, dt \tag{6.6}$$

Where i_N and i represent the current of the monitoring and high fidelity model respectively whereas $x_{n,N}$ and x_n are the nominal and current position. As it is possible to observe in the equations 6.5 and 6.6, these indexes allow to identify the deviations between the nominal and current conditions. Indeed, when the index is similar to 1, the actuator is in the first part of its life, because no deviations can be envisaged from the nominal conditions. However, due to degradation effects, this index changes and becomes higher or lower than 1. In this respect, it is expected that the position index tends to become higher than 1, because the degradation effects leads to lower position values. On the contrary, the current index tends to be lower than 1, because the friction and backlash cause higher current to reach the same final position.

6.2.4 Current ratio

This index is utilized by running the model in closed-loop in order to highlight how the peak current is affected by degradation effects. In particular this parameter can be

expressed as:

$$ratio = \left| \frac{i_{max}}{i_{max,\,N}} \right| \tag{6.7}$$

Obviously, the ratio is similar to 1 when the actuator is slightly affected by degradation effects. However, due to decreased performances the peak current tends to increase up to unacceptable values. However, since this index is a local value, then it is strongly affected by noise effects.

6.3 Frequency analysis - Health monitoring

As before explained, by analyzing the frequency spectrum of signals it is possible to detect faults in ball screws. In the light of this assessment, in this thesis a specific algorithm is developed in order to compute the FFT of the motor current when the actuator works in closed-loop. Indeed, as explained in the previous chapter, the current is the parameter mainly affected to degradation effects.

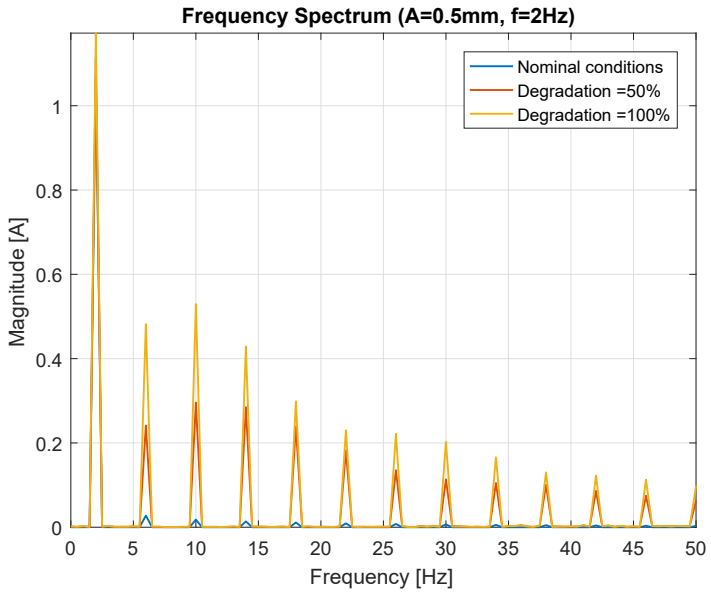

Figure 6.6: Frequency spectrum of the three analyzed cases

In order to evaluate the FFT of the current signal, it is supposed to perform a ground test by forwarding a sine wave SET with $\pm 0,5\,mm$ of amplitude and a frequency of $2\,Hz$. The signal is sampled with a frequency equal to the reciprocal of the monitoring model's maximum time step. Furthermore, the start and finish time are settled in order to consider 4 sine waves of current. At the same time, the degradation is simulated by increasing the backlash and friction. It is supposed that the maximum level of degradation (100%) corresponds to a backlash of $100\,\mu m$ and friction torque and force four times higher than the nominal condition. On the basis of these considerations, in the Figure 6.6 a

comparison between nominal conditions, 50% and 100% of degradation is depicted. As it is possible to observe in the previous figure, the frequency spectrum of the three signals is strongly affected by the degradation effects. Indeed, the nominal signal derived from the monitoring model has a frequency content that is similar to a sine wave function with $2\,Hz$ of frequency and an amplitude slightly higher than $1\,A$. Indeed, the other frequencies of the nominal signal have neglegibile amplitudes. On the contrary, by observing the signals get from the high fidelity model, the frequency spectrum is highly affected by degradation. Indeed, other than the nominal frequency content in corrispondence of $f = 2\,Hz$, the spectrum depicts other frequencies whose amplitudes are not negligible. These last are multiple of the nominal frequency of the signal, according to the Fourier transform theory. Obviously, this situation is caused by expecially the backlash, which leads to evident alterations in the shape of the current signal.
Furthermore, the magnification reported in Figure 6.7 allows to comprehend that the degradation affects the current amplitude in corrispondence of $2\,Hz$, too. Indeed, it is possible to observe that the amplitude of the current increases when the ball screw is major affected by degradation mechanisms.

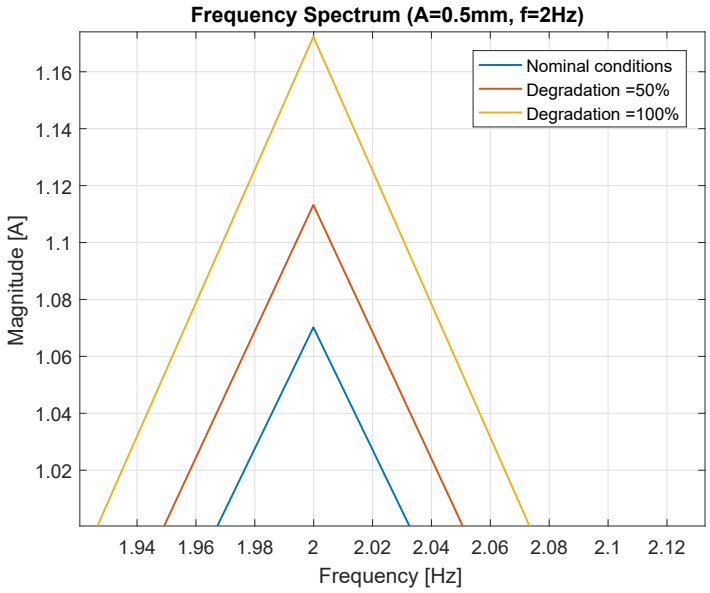

Figure 6.7: Magnification of the Figure 6.6

Therefore, this analysis allows to understand that the frequency spectrum of the current is affected by degradation. Therefore, this methodology represents a promosing concept for further analyses. However, it is necessary to specify that environmental effects such as humidity, temperature, etc. can affect the analysis. Indeed, the performances of the current sensor depends on the afore mentioned variables. However, the deviations are enough high to make this methodology a useful mean to detect faults in ball screws.

6.4 Coefficient analysis - Health Monitoring

As afore explained, the principal aim of the Health monitoring is to isolate possible faults and identify the health conditions of ball screws. In this analysis, two types of studies are conducted, according to the simulations reported in the previous chapter:

- The C_p and $|e|$ are evaluted by forwarding a step and cosine wave command to the servosystem in open-loop. Indeed, by neglecting the effect of the position controller, it is possible to highlight the effect of degradation in the position

- The C_i and the ratio between the real and nominal peak current are analyzed by sending a sine wave command to the servosystem in closed-loop. Indeed, in the previous chapter has been gauged that the current and motor torque are strongly affected to backlash and friction

In particular the degradation effects are simulated by increasing gradually the backlash from $0\,\mu m$ to $100\,\mu m$ and the friction torque and force from the nominal conditions to four times the nominal value. These two intervals are divided in 11 equispaced points and for each point the high fidelity model is run and condition indexes computed. For this reason, the pictures show along the x axis the percentage of the degradation effects. Furthermore, in this analysis the preload force in the start point is not considered because it slightly affects only the current index. Indeed, as the previous chapter shows, if no external load is applied the position trend is not affected by preload force. Moreover, the preload on one hand raises the friction but on the other hand it increases the stiffness of the servosystem. For this reason, the effect of the preload force is negligible in the current index too. However, this last is taken into account in the Usage part, in order to have a realistic representation of the ball screw's life.

6.4.1 Open Loop

This subsection explains the variation of C_p and $|e|$ by sending a step and cosine wave velocity command to the servosystem in open-loop with the following characteristics:

- The step commmand starts at $0\,s$ and it has an amplitude of $30\,rad/s$. Successively, the command returns to $0\,rad/s$ at $t_{fin} = 0.2\,s$, whereas the total simulation time is $t_{sim} = 0.3\,s$

- The cosine wave command has a frequency of $f = 2\,Hz$ and an amplitude of $\pm 30\,rad/s$. The simulation time is settled in order to have four sine waves of the SET command

In particular, these commmands have already analyzed in section 5.7.4 with the only difference that the step command starts at $0\,s$ in this case. Therefore, to observe the time plots it is possible to refer to Figures 5.43 and 5.46.

First of all, in the Figure 6.8 the C_p and error trend for the step command for both noise and no noise cases are depicted. As the Figure shows, initially the position fidelity coefficient is equal to 1, because the position from both monitoring and high fidelity model are coincident. However, due to the decreased accuracy caused by degradation, the C_p tends to raise. By monitoring the position fidelity coefficient it is possible to observe that the maximum deviation from the nominal condition is equal to 8.4%. At the same time the error, which is initially very low, tends to increase until reaching $77\,\mu m$. It is important to observe that both trends are monotonic and therefore can be useful under a diagnostic and prognostic point of view. However, the maximum amplitude of the error is too low to be detectable.

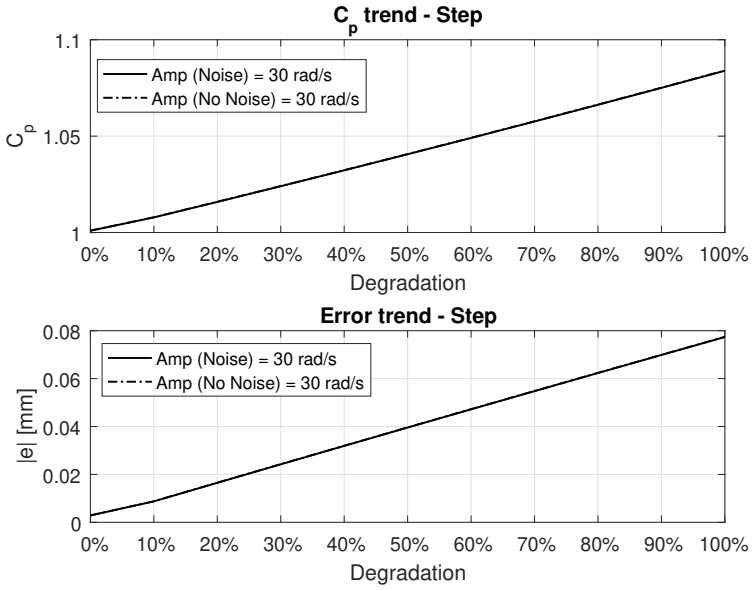

Figure 6.8: C_p and error trend for the step velocity command

For this reason, the health state can be envisaged by utilizing the position fidelity index, because the maximum deviation would be high enough to be detectable. Finally, it is necessary to note that the noise does not affect the position trend. Indeed, as the simulations of the previous chapter showed, the physical parameter that is mostly affected to noise effects is the current. Indeed, each controller reduces the noise effects by correcting the output based on the noise disturbance. Since the position is the outer loop, then it is the least affected parameter of noise effects.

Furthermore, the Figure 6.9 shows the C_p and $|e|$ trends by sending a cosine wave velocity command to the servosystem. In particular, several types of commands are analyzed in

this thesis because the results are certainly not deterministic. Since each trend is not dependent to each others, then by combining the results it is possible to reduce the dispersion of the obtained outcomes.

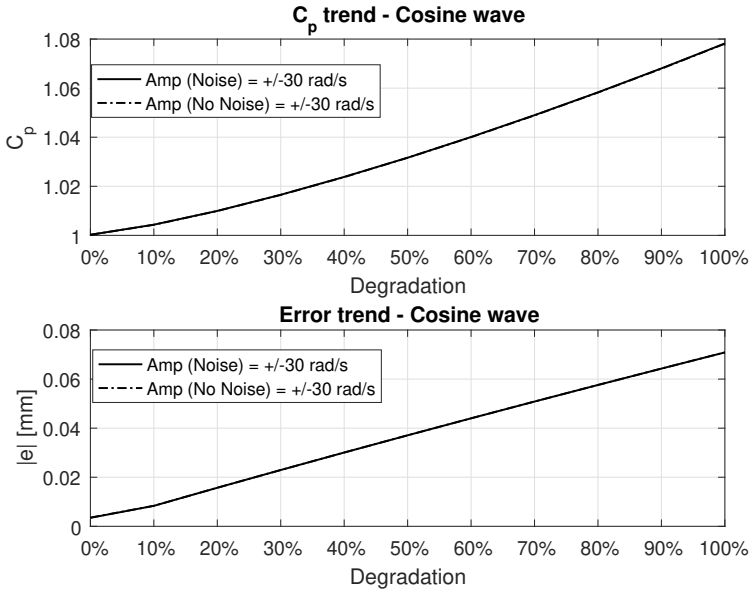

Figure 6.9: C_p and error trend for the cosine wave velocity command

As it is possible to observe in the previous figure, the trends are similar to Figure 6.8. However, in this case the deviations of the C_p and the error are a little bit lower, by amounting to 7.8% and 70 μm respectively. The maximum deviation of C_p is quite reasonable because the double nut with the backlash stationate for longer time intervals in the maximum and minimum position due to the loss of motion. For this reason, there will be a time interval in which the delay causes a real position higher than the nominal one. Therefore, this situation reduces the maximum deviation of C_p. Finally, the C_p trend of the step command has substantially a linear trend whereas the position index is similar to a quadratic function for the sine wave.

6.4.2 Closed loop

As afore explained, by running the model in closed loop it is possible to highlight the effect of degradation mechanisms in the current and torque trend. Indeed, in order to reach the same final position, the motor has to provide a higher current and torque, by leading to decreased ball screw efficiency. Moreover, it is expected that the deviations in the current trend will be higher, according to the simulations carried out in the previous chapter. This subsection does not analyze the behavior of the current when a step command is imposed to the servosystem. Indeed, in this case the current reaches the saturation value both in nominal and current conditions. For this reason, the wear mechanisms does not

affect the current trend in closed loop in this case. However, by imposing a sine wave command it is possible to observe several deviations from the nominal current. For this reason, a sine wave command with $\pm 0,5\,mm$ of amplitude and $f = 2\,Hz$ is imposed. It is possible to observe that this command was analyzed in the section 5.7.4, where the position time plot is depicted in Figure 5.47.
In the Figure 6.10 the current fidelity index as well as the absolute value of the ratio between the real peak current and the nominal one are shown.

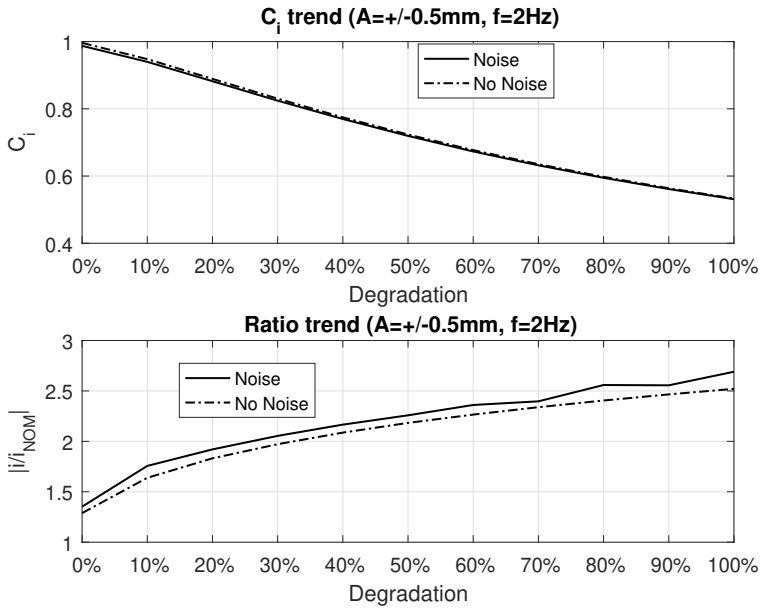

Figure 6.10: C_i and ratio trend for the sine wave position command

As the Figure 6.10 shows, the current is strongly affected by wear mechanisms and degradation effects. Indeed, the C_i shows a total deviation of 46% whereas the peak current becomes up to 2.7 times higher than the nominal conditions. For this reason, it is quite clear that the current fidelity index represents the most promising concept to identify possible faults in ball screws. Furthermore, the noise in this case has a higher influence respect to the position, especially regards to the peak current observed during the simulations. In fact, the peak current is strongly affected by noise effects because it is a local value. However, the deviations caused by the white noise are low in the current fidelity index, since it considers the entire simulation time. In particular, the highest differences can be observed especially in the first part of the C_i trend. Indeed, the deviations between nominal and current conditions are affected to the noise effects only in the first part of ball screw life, when the differences between nominal and current conditions are very low. As the degradation effects become greater, the noise effect becomes lower bacause the different behavior between the two models are principally due to the increased backlash and friction, that cause decreased performances. For this reason the current fidelity index

represents the most promising concept to identify failures in ball screws. In fact, this index is utilized to carry out the Usage monitoring part in the next section.

6.5 Usage (Prognostic)

As explained in the chapter 4, the Usage part allows to predict the RUL of the electromechanical actuator.

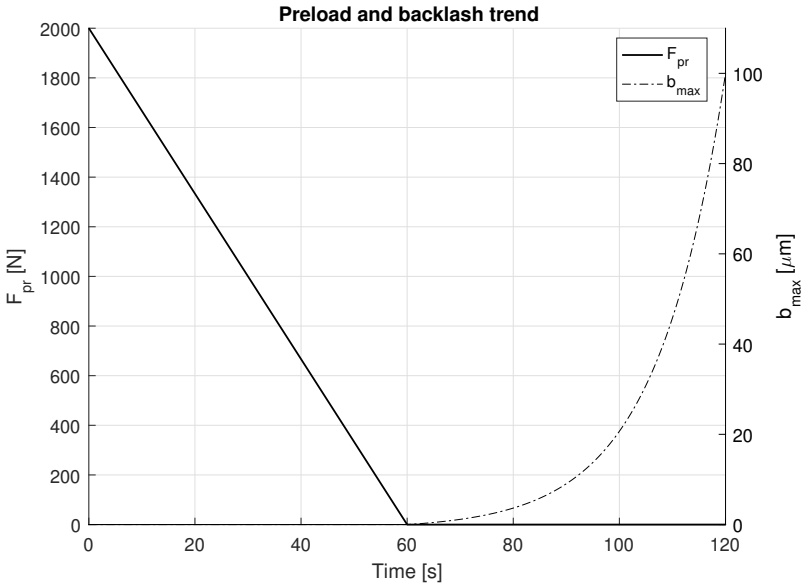

Figure 6.11: Preload and backlash trends during simulation time

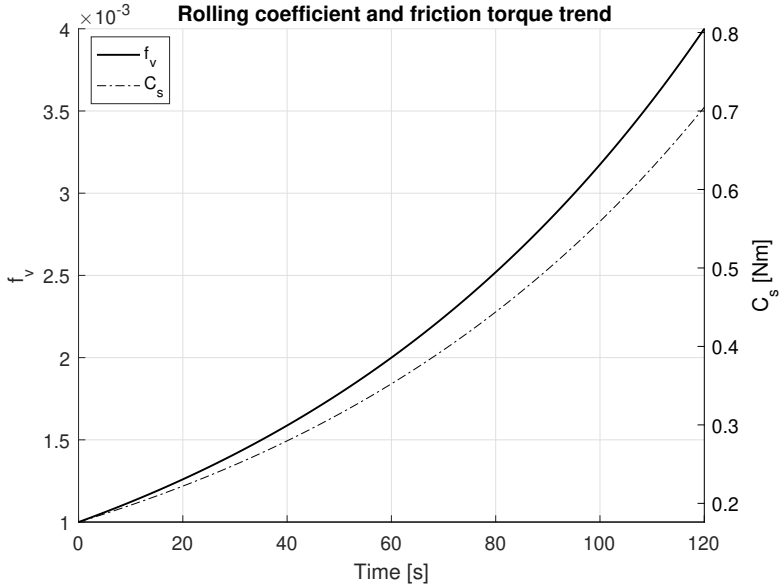

Figure 6.12: Rolling and static friction trends during simulation time

In order to do that, it is necessary to take into account the principal parameter of the

Usage methodology: the time. Indeed, the degradation and wear mechanisms are in development continuosly, during the activity time of the EMA. For this reason, in this subsection a prognostic algorithm is proposed, on the basis of the current fidelity index evaluated in the previous section, because it represents the health index most affected by degradation. In particular, the developed algorithm follows the methodology proposed in [31] but applied to this case of study.

In particular, it is supposed to have a preloaded ball screw with $F_{pr} = 2\,kN$. In the previous section the preload was not considered because it affects slightly the current fidelity index. Indeed, the preload force on one hand causes increased friction forces and torques but on the other hand it increases the stiffness, by decreasing the servosystem sensitivity to the friction phenomena when the inversion of motion occurs. In fact, it will be possible to observe that the starting point of the C_i curve is similar to Figure 6.10.

As explained in the last section of chapter 2, it is possible to suppose a linear decreasing of the preload force. For this reason, the preload force decreases in the first part of the simulation with a linear trend.

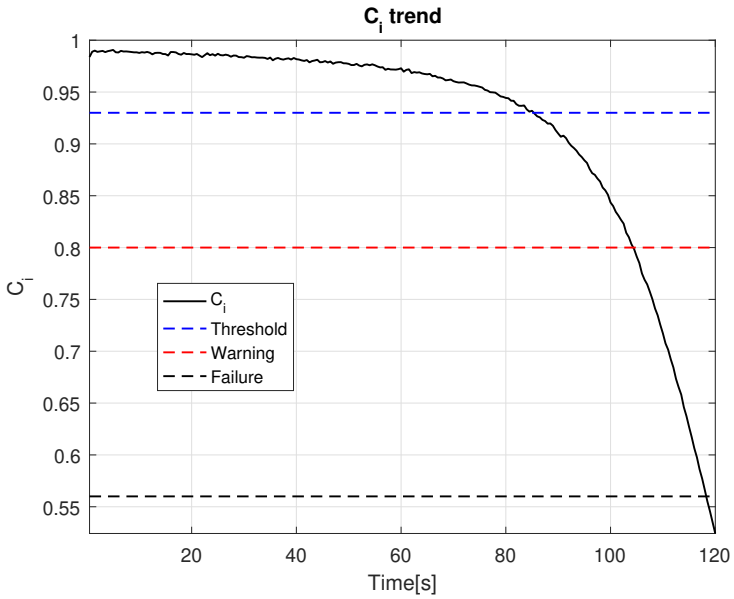

Figure 6.13: C_i trend during the simulation

Moreover, the Figures 6.11 and 6.12 show that the backlash and friction increase with an exponential trend, by reaching the final values of 100% of degradation. It is chosen these trends because usually the degradation is not linear, but it increases slowly initially and it shows high variations in the last part of the actuator's life. Therefore, the Usage methodology has to identify the EMA's RUL in correspondence of the failure point. This last can be chosen according to the final value of section 6.4.2. However, in order to have a conservative analysis, the failure point is increased to 5% than the final value of the C_i index represented in Figure 6.10. For this reason, the failure point corresponds to a

current index equal to 0.56.

In the proposed algorithm, two other levels are settled: the threshold and warning level. The first one represents the point after that the deviations from the nominal conditions are not negligible. When this level is overcome, the prognostic algorithm does not provide an alarm but it stores the points in order to identify the fitting curve capable to approximate the C_i trend beyond the threshold value. However, the algorithm is not capable to provide the EMA's RUL because larger data are necessary to have a reliable analysis. This process continues up to the warning level. Indeed, when this last is reached, the prognostic algorithm has collected enough data to provide a warning and predict the RUL.

All these levels with the C_i trend during the simulation time are depicted in Figure 6.13. As it is possible to observe, the C_i is essentially constant during the first half of the simulation time. Indeed, the decreasing of the preload force leads to decreased friction. However, the friction forces and torques are increasing according to the trend of Figure 6.12. Therefore, these two effects leads to a fidelity index which is essentially constant. However, when the preload becomes null and the backlash increases, it is possible to observe a change of the slope in the curve of Figure 6.13. In fact, the final slope of the curve is very high, according to the behavior of degradation effects in mechanical components. Indeed, the chapter 3 allows to understand that worn out components tend to have faster degradation than health parts. For this reason, the trend depicted in Figure 6.13 appears to be realistic.

Furthermore, the threshold value is settled to 0.93, which corresponds of the value where a deviation of 5% from the nominal conditions can be envisaged. The warning level is settled to 0.8, because beyond this point, the prognostic algorithm has collected enough data to predict the RUL of the actuator. The proposed prognostic algorithm evaluates the fitting curve between the points immediately beyond the threshold and warning levels. Obviously, these last have to be evaluated more accurately by performing several experimental tests.

In this case a third order polynomial function is utilized to fit the data between the threshold and warning level, as depicted in Figure 6.14. As it is possible to observe, the fitting function well approximate the real data collected during the simulation. Indeed, only negligible differences can be envisaged.

Therefore, by utlizing the fitting curve is now possible to predict the actuator's RUL. In particular this last is depicted in Figure 6.15.

As it is possible to observe, the algorithm predicts a RUL equal to 13.5 s in corrispondence of 118 s. This time instant corresponds to a real backlash of 85 μm and a friction 3.9 times higher than the nominal conditions.

Therefore, it is possible to conclude that the proposed analysis leads to conservative re-

sults because the time-to-failure is lower than the maximum values of degradation. In this respect, it is necessary to underline that the RUL can be identified only after that degradation effects lead to high deviations in the current fidelity index. Indeed, this last is not affected by the decreasing of the preload force, as afore explained. This is a limit of the proposed algorithm because the prediction of the EMA's RUL can be carried out only in the last part of the actuator's life.

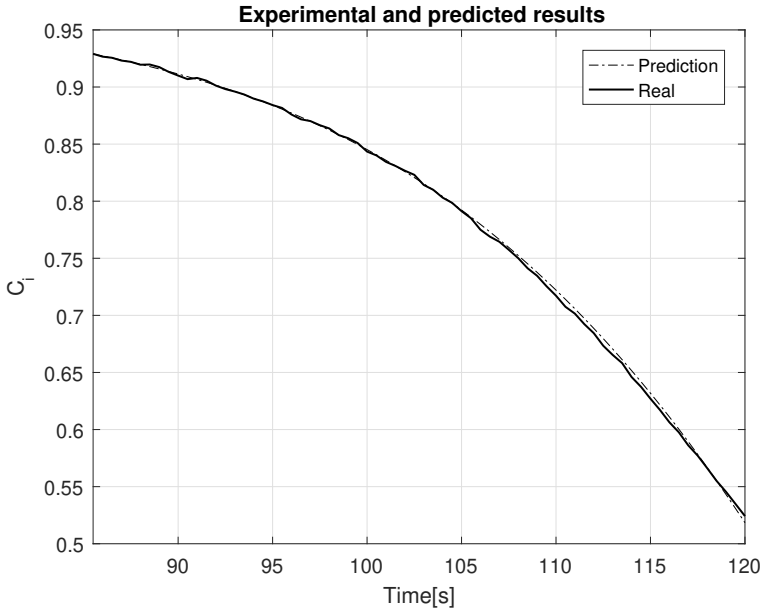

Figure 6.14: Fitting of the real data

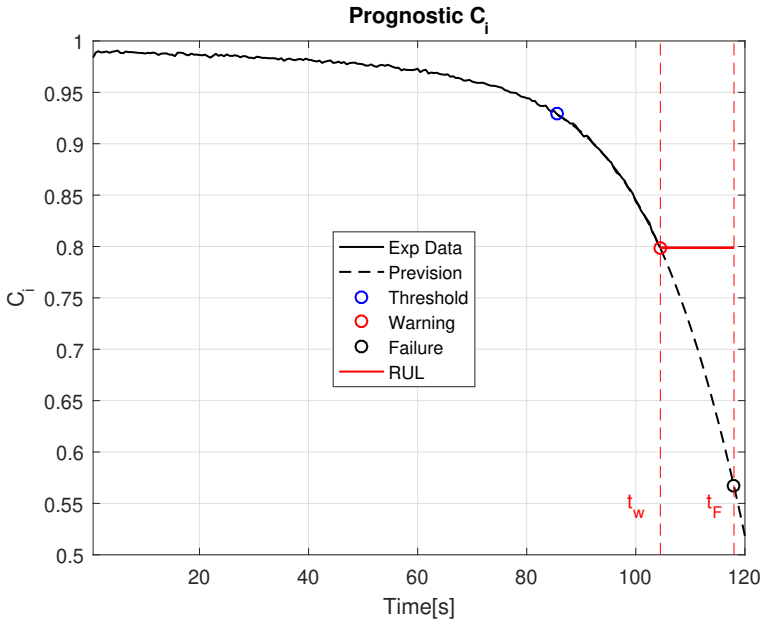

Figure 6.15: Prevision of the EMA's RUL

Indeed, it is possible to observe that the prediction can be obtained when the actuator has performed about 90% of its life. Obviously, the problem of the proposed algorithm

is due to the degradation trend which is not linear in mechanical components. For this reason, there is a high decrease of performances in a short time interval in the final part of the EMA's life. This issue represents one of the worst problems of the prognostic algorithms applied to wear mechanisms, where the decrease in performance is very quick. However, this methodology can represent a useful mean to predict the EMA's RUL before catastrophic failures can happen.

Conclusions

This thesis has the purpose to develop a HUMS applied in ball screws for EMAs in primary flight controls. In order to do that, an extensive literature research is conducted, by which a ball screw high fidelity model is developed on the basis of [1, 2]. This last is embedded in the whole EMA model in order to simulate in detail its behavior under several conditions. In order to evaluate the model's behavior, many simulations are carried out. Indeed, the fifth chapter analyzes the model behavior by varying preload, external force, type of command and simulating the degradation. In particular, this last simulation is performed by increasing the backlash and friction up to $100\,\mu m$ and four times the nominal value, respectively. Thanks to this simulation it is possible to understand that the degradation effects affect the position trend when the model is run in open-loop. In fact, in this way the effect of the degradation in the position trend can be underlined, because the first proportional controller does not operate. Furthermore, the current shows several peaks due to the dead zone caused by the friction and especially backlash by running the model in closed-loop. Indeed, in this case the position controller tends to impose higher current in order to reach the same final position.

On the basis of these results, in the last part of this thesis a monitoring model is developed, in order to simulate the nominal conditions of the high fidelity model. A minimization algorithm is utilized to reduce the differences between the monitoring and high fidelity model in nominal conditions. Therefore, on the basis of the obtained results in the fifth chapter, two methodologies are proposed in this thesis.

The first one utilizes the frequency spectrum of the current signal when the model is run in closed-loop. In particular, this methodology leads to promising results because the faulted ball screw shows a different frequency spectrum compared to the nominal one. These deviations could be as high in ground tests to detect degradation in ball screws as well as carrying out their health assessment.

Furthermore, the second methodology is based on several condition indexes previously defined in [30, 31]. In particular, an analysis based on the position and current fidelity indexes (C_p and C_i respectively) is proposed to identify the deviations of the high fidelity model from the nominal conditions. By running the model in open-loop it is possible to identify a maximum deviation of the position index up to 8.4% for a step command

and 7.8% for a cosine wave command. However, the index which is most affected by degradation is the current fidelity index. Indeed, by forwarding a sine wave command in closed-loop, it is possible to detect a maximum deviation equal to 46%.

In the light of these results, a methodology to predict the EMA's RUL is explained in the last part of the thesis. In this respect, the methodology proposed in [31] is utilized, where a prognostic algorithm for a servovalve is carried out. In order to predict the EMA's RUL, a sine wave command is forwarded to the servosystem for $120\,s$, in which the degradation is simulated by decreasing the preload force until a null value and increasing the friction and backlash with an exponential trend. The prediction of the RUL is conducted by identifying a threshold, warning and failure point. By computing the fitting curve capable to approximate the data of the high fidelity model between the threshold and warning levels, a prediction of the actuator's RUL can be obtained in a conservative way. However, the prediction of the EMA's RUL can be carried out but only in the last part of the simulation time. In fact, usually the increase of degradation is not linear, but it is slower in the first time interval and it raises faster in the last part of the actuator's life.

In this respect, it is necessary to underline that the proposed methodologies are carried out by using a complex model which has to be experimentally validated. For this reason, the next step of the proposed work is to carry out the validation of the complex model, as the outlooks of this thesis will be explained in detail.

Future Outlooks

The proposed methodologies are capable to detect the degradation in ball screws as well as predicting its Remaining Useful Life. However, in order to have more reliable analyses, it is necessary to carry out the experimental validation of the model by using a test rig. Moreover, it is expected that to improve the reliability of the analyses, several ground parameters that can affect the measurement has to be taken into account. For instance, it is known that the sensor performances depend on the operating temperature. Therefore, the theoretical deviations analyzed in this thesis could be lower in the real tests. However, the deviations are high enough to represent a useful mean to detect degradation and decreased performances in ball screws.
Furthermore, in order to obtain the motion of a primary flight control surface, usually two EMAs are employed. Therefore, the pre-flight tests can be conducted by moving either or both actuators. It is expected that the results proposed in these methodologies should be more reliable by conductiong the test moving both of actuators, in order to reduce as far as possible the loads acting on the actuator during maintenance works.
At the same time, it is necessary to underline that the explained methodologies are based on a parametric simulation of degradation effects. Therefore, in order to have a more detailed overview of ball screws' degradations, a deeper analysis of wear mechanisms could be implemented in the model in future works. Indeed, in the chapter 3 several types of wear mechanisms are treated in order to give an overview of the most common failures causes in mechanical components. Therefore, a simulation of wear mechanisms according to deeper studies can represent a promising concept for future works.
Finally, the model is capable to simulate the motor thermal behavior. This last is not used in this thesis because the detected deviations are too low in the ground tests, where the commands are imposed to the servosystem for short time periods. In order to have reliable results, a more detailed thermal model has to be carried out, which has to be capable to take into account the refrigerant fluids that influences the windings' temperature. In this way, it is possible to analyze the in-flight data, where the actuator acts many random movements for larger time periods. In fact, since the degradation causes higher current, then the windings temperature tends to increase. Therefore, this last could represent a useful parameter to detect the deviations of the actuator from its nominal conditions.

Bibliography

[1] A. C. Bertolino, G. Jacazio, M. Sorli, and S. Mauro. High Fidelity Model for Efficiency Calculation of Ball Screws for Flight Control Actuators. *Recent Advances in Aerospace Actuation Systems and Components*, 2018.

[2] Antonio Carlo Bertolino. *Modellazione di sistema vite/madrevite in attuatori elettromeccanici per comandi di volo.* Master thesis, Politecnico di Torino, 2015/2016.

[3] Learn to Fly [online]. `http://learntoflyblog.com/2017/04/27/cfi-brief-flight-controls-of-a-typical-commercial-airliner/`.

[4] MARÉ Jean-Charles and FU Jian. Review on signal-by-wire and power-by-wire actuation for more electric aircraft. *Chinese Journal of Aeronautics*, 30(3):857–870, 2017.

[5] Jean-Jacques Charrier and Amit Kulshreshtha. Electric actuation for flight & engine control system: evolution, current trends & future challenges. In *45th AIAA Aerospace Sciences Meeting and Exhibit*, volume 8, 2007.

[6] Ricardo de Arriba and Alberto Gallego. Health and Usage Monitoring System (HUMS) Strategy to enhance the Maintainability & Flight Safety in a Flight Control Electromechanical Actuator (EMA).

[7] Jean-Claude Derrien and Sagem Défense Sécurité. Electromechanical Actuator (EMA) advanced technologies for flight controls. In *International Congress of the Aeronautical Sciences*, pages 1–10, 2012.

[8] Features of ball screws [online]. `https://tech.thk.com/en/products/pdf/en_b15_006.pdf`.

[9] Fabio Gallerani. *Analisi numerico sperimentale del rendimento nelle viti a ricircolo di sfere.* Master Thesis, Politecnico di Milano, 2011/2012.

[10] MC Lin, SA Velinsky, and B Ravani. Design of the ball screw mechanism for optimal efficiency. *Journal of mechanical design*, 116(3):856–861, 1994.

[11] Chin-Chung Wei and Ruei-Syuan Lai. Kinematical analyses and transmission efficiency of a preloaded ball screw operating at high rotational speeds. *Mechanism and machine theory*, 46(7):880–898, 2011.

[12] Chin-Chung Wei, Wei-Lun Liou, and Ruei-Syuan Lai. Wear analysis of the offset type preloaded ball–screw operating at high speed. *Wear*, 292:111–123, 2012.

[13] Bikramjit Basu and Mitjan Kalin. *Tribology of ceramics and composites: a materials science perspective*. John Wiley & Sons, 2011.

[14] Boris Popović, Tino Bucak, and Nikica Hoti. Hums-Health and Usage Monitoring System. *Promet-Traffic-Traffico*, 12(4):179–184, 2004.

[15] Yong Shen, Xingwang Li, Xiumei Zhai, Huiyun Wang, and Yifei He. Design on the health and usage monitoring system. In *Prognostics and System Health Management Conference (PHM-2014 Hunan), 2014*, pages 465–468. IEEE, 2014.

[16] Michel Todeschi and Laura Baxerres. Health monitoring for the flight control EMAs. *IFAC-PapersOnLine*, 48(21):186–193, 2015.

[17] Andrea De Martin, Jacazio Giovanni, and Geroge Vachstevanos. Anomaly Detection and Prognosis for Primary Flight Control EMAs. 2016.

[18] Jay Lee, Fangji Wu, Wenyu Zhao, Masoud Ghaffari, Linxia Liao, and David Siegel. Prognostics and Health Management design for rotary machinery systems—Reviews, methodology and applications. *Mechanical systems and signal processing*, 42(1-2):314–334, 2014.

[19] Jin-Hyuk Kim, Yurim Park, Yoon-Young Kim, Pratik Shrestha, and Chun-Gon Kim. Aircraft health and usage monitoring system for in-flight strain measurement of a wing structure. *Smart Materials and Structures*, 24(10):105003, 2015.

[20] E Gilson, JD Kopp, and D Manzanares. Moog next generation control and actuation. *Proc. of Recent Advances in Aerospace Actuation Systems and Components*, 2014.

[21] Won Gi Lee, Jin Woo Lee, Min Sung Hong, Sung-Ho Nam, YongHo Jeon, and Moon G Lee. Failure diagnosis system for a ball-screw by using vibration signals. *Shock and Vibration*, 2015, 2015.

[22] Carl S Byington, Matthew Watson, Doug Edwards, and Paul Stoelting. A model-based approach to prognostics and health management for flight control actuators. In *2004 IEEE Aerospace Conference Proceedings (IEEE Cat. No. 04TH8720)*, volume 6, pages 3551–3562. IEEE, 2004.

[23] Chung Seng Ling, Dan Hewitt, Steve G Burrow, Lindsay Clare, David AW Barton, Dan M Wells, and Nick AJ Lieven. Technological challenges of developing wireless Health and Usage Monitoring Systems. In *Health Monitoring of Structural and Biological Systems 2013*, volume 8695, page 86950K. International Society for Optics and Photonics, 2013.

[24] Lorenzo Trecroci. Notes, Mechatronic course Prof. Massimo Sorli, Politecnico di Torino, 2017-2018.

[25] Design PID Controller Using Estimated Frequency Response [online]. `https://it.mathworks.com/help/slcontrol/ug/designing-pid-controller-in-simulink-with-estimated-frequency-response.html`.

[26] Nicola Pozzi. FRF function, Mechatronic course Prof. Massimo Sorli, Politecnico di Torino, 2017-2018.

[27] Linear Motion Tips [online]. `https://www.linearmotiontips.com/how-to-calculate-the-effect-of-preload-on-ball-screw-axial-deflection/`.

[28] Mattias Nordin, Johann Galic', and Per-Olof Gutman. New models for backlash and gear play. *International journal of adaptive control and signal processing*, 11(1):49–63, 1997.

[29] Prof. Massimo Sorli. Function developed in the Mechatronic course, Politecnico di Torino, 2017-2018.

[30] Paolo Maggiore, Matteo DL Dalla Vedova, Lorenzo Pace, and Alessio Desando. Definition of parametric methods for fault analysis applied to an electromechanical servomechanism affected by multiple failures. In *Proceedings of the Second European Conference of the Prognostics and Health Management Society*, pages 561–571. Citeseer, 2014.

[31] Lorenzo Borello, MDL Dalla Vedova, Giovanni Jacazio, and Massimo Sorli. A prognostic model for electrohydraulic servovalves. In *Annual Conference of the Prognostics and Health Management Society*, pages 1–12, 2009.

[32] Alan V Oppenheim and Ronald W Schafer. *Discrete-time signal processing*. Pearson Education, 2014.

Acknowledgements

Vorrei ringraziare tutti coloro i quali mi hanno permesso di svolgere al meglio questo lavoro di tesi, grazie a critiche costruttive e suggerimenti che mi sono tornati utili durante tutti questi mesi.
Volevo innanzitutto ringraziare il Prof. Massimo Sorli e il Prof. Giovanni Jacazio per avermi permesso di vivere questa bellissima esperienza.
Ringrazio il Prof. Frank Thielecke per avermi consentito di svolgere questo lavoro di tesi presso la TUHH, esperienza che mi ha arricchito come persona e mi ha permesso di mettermi alla prova in un contesto del tutto nuovo ma stimolante.
Ringrazio infine Christoph Kupfer, il quale ha supervisionato il mio lavoro con diligenza e professionalità, fornendomi preziosi consigli per completare al meglio questo lavoro di tesi.
Vorrei dedicare il mio lavoro in primis alla mia famiglia, per il supporto fornitomi durante il mio soggiorno ad Amburgo. In particolare, volevo ringraziare mio padre, per le numerose (seppur brevi) chiamate e per il sostegno fornitomi durante tutto il mio corso di studi. Volevo inoltre dedicare il mio lavoro a mia madre, che mi è stata vicino con il cuore durante tutti questi anni.
Allo stesso modo, volevo dedicare questo lavoro a tutti i miei amici di Cosenza, grazie ai quali ho passato bellissime esperienze in cui spesso ci si divertiva con battute fini e sofisticate, come la nostra etichetta impone.
Infine, volevo dedicare questa tesi a tutti gli amici che ho conosciuto a Torino (Salernitani e non), con cui ho passato due anni splendidi che ricorderò per tutta la mia vita.